AN ABSTRACT OF THE THESIS OF

Paige Elizabeth McKinley for the degree of Master of Science in Wood Science presented on August 5, 2016.

Title: Multi-scale Investigation of Adhesive Bond Durability.

Abstract approved:

Frederick A. Kamke Arijit Sinha

Moisture durability is essential for wood composites, especially those used in building construction, where products are prone to weathering. The primary focus of this research was to determine if adhesive penetration into the cell wall has a positive influence on adhesive bond durability. To fully understand the measureable effects of adhesive penetration on moisture resistance, a multi-scale investigation was conducted.

The study used bonded Douglas-fir lap-shear test specimens (6mm x 14 mm x 64 mm), varying in bonded surface cell type (earlywood vs. latewood) and adhesive type. The adhesives of interest were a low and high molecular weight phenol-formaldehyde (PF), a low molecular weight PF with added filler and extender, and a methylene diphenylene diisocyanate (MDI). Half of each group of test specimens was subjected to accelerated weathering and the rest remained dry. All samples were mechanically tested in lap-shear. During the test, Digital Image Correlation (DIC) was used to track

displacements across the surface of the sample. The failure load, effective shear modulus, energy to failure, percent wood failure, failure mode, and DIC shear strain maps were used to evaluate the mechanical performance of the dry and weathered specimens.

Smaller samples (2 mm x 2 mm x 10 mm) were cut from the previously tested lap-shear samples and scanned at the Advanced Photon Source (APS), Argonne National Laboratory, using micro-X-ray Computed Tomography (XCT). All adhesive types were previously tagged with iodine to increase contrast during the XCT scans. This technique gave high resolution (1.3 μm^3/voxel), 3D images for which adhesive penetration was analyzed. Further, additional samples were cut from the previously scanned micro-XCT samples for nano-XCT scanning at the APS. The nano-XCT data gave a resolution of 60 nm^3/voxel, allowing for detection of adhesive penetration into the cell substance and sub-micron cell features. Complementary analyses using Energy Dispersive Spectroscopy (EDS) and X-ray Fluorescence Microscopy (XFM) were used to confirm the presence of iodine in areas containing adhesive, and to further observe adhesive penetration into the cell substance.

Statistical analysis showed two of the adhesive formulations had significant differences in mechanical properties after weathering. Weathering had a negative effect on the mechanical properties. DIC shear strain maps revealed that the same two adhesive formulations had more strain around the bonded interphase at the same applied load. Adhesive penetration into the cell substance was observed, but cannot be quantitatively compared between the four adhesives, due to inadequate image quality from nano-XCT and the low number of specimen replications. Overall, there was more effective adhesive penetration in the lower molecular weight adhesive and less shear strain calculated from

the DIC macroweathered analysis. This indicated that adhesive penetration could have a positive influence on moisture durability, although the variability is too high to make a definite conclusion and there were not enough replicates to compare the amount of adhesive penetration into the cell wall.

Multi-scale Investigation of Adhesive Bond Durability

by
Paige Elizabeth McKinley

A THESIS

Submitted to

Oregon State University

in partial fulfillment of
the requirements for the
degree of

Master of Science

Presented August 5, 2016
Commencement June 2017

Master of Science thesis of Paige Elizabeth McKinley presented on August 5, 2016.

APPROVED:

_____

Co-Major Professor, representing Wood Science

_____

Co-Major Professor, representing Wood Science

_____

Head of the Department of Wood Science and Engineering

_____

Dean of the Graduate School

I understand that my thesis will become part of the permanent collection of Oregon State University libraries. My signature below authorizes release of my thesis to any reader upon request.

_____

Paige Elizabeth McKinley, Author

ACKNOWLEDGEMENTS

Countless people have directly and indirectly been an inspiration and have helped me with this achievement—thank you! I would like to express my sincerest appreciation to the following people who have made a tremendous impact on my graduate career:

Lech Muszyński	Jesse Paris
Milo Clauson	Angela Haney
Daniel Ching	Jessica King
Chad Hammerquist	Michelle Maller
Vincent DeAndrade	Matt Edelstein
Xianghui Xiao	Betsy, Suzanne, and Camille
Joseph Jakes	Blake, Byrne, and Danny
Teresa Sawyer	Fred and Ari's lab groups

Additionally, my advisors, Fred Kamke and Ari Sinha, for giving me guidance while still allowing me to have independence for my own exploration. I will be forever grateful of your mentorship and I know my graduate studies would not have been as successful without you two. The Wood Based Composites Center and Linda Caudill for industry feedback and professional development. The US National Science Foundation for funding this project (Grant No. IIP-1331043). Finally, I would not be where I am today without the love and support of my parents, brothers, and all of my family and friends—thank you for everything you do!

TABLE OF CONTENTS

Page

TABLE OF CONTENTS

Page

TABLE OF CONTENTS

Page

LIST OF FIGURES

Figure Page

LIST OF FIGURES

LIST OF FIGURES

LIST OF FIGURES

LIST OF FIGURES

Figure Page

LIST OF FIGURES

Figure Page

LIST OF FIGURES

LIST OF FIGURES

LIST OF FIGURES

Figure Page

LIST OF FIGURES

LIST OF FIGURES

LIST OF TABLES

LIST OF TABLES

LIST OF TABLES

CHAPTER 1: INTRODUCTION

The residential building industry in the United States today depends heavily on wood as the main raw material for building products. Current wood building products fall into two main categories: solid lumber and engineered wood products. Solid lumber is generally used for framing (studs). Engineered wood products are comprised of wood and an adhesive system to bind the wood together. This means that engineered wood products can be manufactured into various shapes and sizes that are not possible/feasible with solid timber. These are often used as sheathing (OSB, plywood), subflooring, and for large spanned areas such as floor joists (I-joists) or header beams (LVL). Wood composites are desirable for many reasons: they typically have better structural properties since any defects are distributed throughout the product; they have the ability to be manufactured into shapes that may not be available from solid wood; they utilize raw materials that may otherwise be considered unusable.

Wood composites as building products are favorable in structural design due to the high strength to weight ratio and ease to manufacture in different shapes. In addition, wood is a natural, renewable, and abundant resource that will be sustainable for generations to come. A biological material, such as wood, is much more susceptible to various types of deterioration when placed in an unfavorable climate (moisture, temperature, ultraviolet (UV) light, etc.). Therefore, ensuring that a structural product is durable, and continues to be durable, throughout years in service is essential.

Durability of building products has been a topic of research for many years due to the importance of structurally sound products for the health and safety of the building. Durability refers to the ability of the material to resist deterioration factors and still be

able to meet certain benchmark criteria. These benchmark criteria are often set up in standards for specific products. Measuring the durability can refer to different aspects of the product integrity and are typically determined based on the product use. Deterioration factors come in many forms including, but not limited to, fungal, UV, and moisture-induced degradation. This research focuses on the latter— moisture-induced degradation.

Wood shrinks and swells as it takes up and releases water, especially when the wood substance is fully saturated. Solid wood has different rates of shrinking and swelling in each direction (tangential, longitudinal, and radial) and different cell types (earlywood vs. latewood). Engineered wood products react differently than solid wood since the presence of the adhesive adds more complexity in the rate of shrinking and swelling of the product. The adhesive is a non-porous, sometimes brittle, material that does not uptake the water in the same manner as the wood.

Engineered wood building products are often exposed to the natural elements during the construction phase due to unexpected weather or delays in the construction process. This results in extreme conditions, such as cycles of moisture (precipitation, snow, and condensation) and temperature changes (afternoon sun exposure to cool nights) over a period of time. This puts extra stresses on the overall product, and more specifically, the wood and adhesive interphase, due to the differences in properties of the wood and the adhesive (Frihart, 2009).

Measuring the effects of moisture on the product can be difficult due to the many parameters involved, such as sample size, amount of moisture exposure, cyclic moisture exposure, type and size of fiber, and type of adhesive. Fundamental knowledge must be

gained in order to formulate better building systems for the current products on the market, and for future innovations.

1.1 Research Objectives

This research dives into a question of high interest to adhesive chemists and wood composite product manufacturers: what effect does adhesive penetration into the cell wall substance have on the moisture resistance of the bondline? It is hypothesized that if the adhesive polymer can penetrate into the cell wall and then polymerize, it will reinforce the cell substance and provide more dimensional stability (Frazier & Ni, 1998). This Interpenetrating Polymer Network (IPN) theory is directly related to the performance of the adhesive interphase region when exposed to moisture. The porous wood structure shrinks and swells at a different rate, and at a different extent, than the adhesive. This phenomenon can cause critical stress concentration at the bondline, and potentially delamination, significantly altering the product performance. If the adhesive is able to enter the cell wall substance and polymerize, it could create a more uniform rate of shrinking and swelling. Even further, it could possibly lessen the amount of shrinking and swelling in the interphase region due to the rigid structure of the adhesive bulking up the cell substance and blocking pathways for moisture intrusion. Answering this question will give insight to how adhesive formulations can better improve current wood composite products, and help develop new ones.

To fully understand the measureable effects of adhesive penetration on moisture resistance, a multi-scale investigation is necessary. The macro performance of the bonded wood product is effected by the micro details of the bondline and therefore both must be studied at multiple resolutions. The overarching goal of this project was to determine if

adhesive penetration into the wood cell has an effect on the moisture durability of the bondline.

The specific objectives of this project are:

- Develop a technique to detect penetration of an organic polymer inside the cell walls of wood using x-ray computed tomography (XCT).
- Obtain a quantitative measurement of adhesive penetration into the cell wall and resolve sub-micron details of the cell wall using XCT.
- Measure moisture-induced, three-dimensional (3D), micron-scale deformation of a wood-adhesive bond and correlate the observations with macro adhesive bond performance.
- Determine if adhesive penetration into the cell wall has a positive influence on moisture resistance.

Not only is it difficult to visualize the 3D, unique structure of the wood-adhesive interaction, it is more difficult to quantitatively measure adhesive penetration. Micro-XCT is an emerging technology that has found many applications in biology and the study of materials. Synchrotron-based micro-XCT has been adopted for this study of adhesive bonding in wood to qualitatively and quantitatively understand the wood-adhesive interactions in 3D. This method has been successfully used before to examine bonded wood (Paris, 2014), but this study will be using XCT to assess durability.

To correlate the measurements of penetration with the bond performance, a sophisticated mechanical bond evaluation must be used. The traditional, lap-shear tension test leaves out a lot of information about how the bondline performed before failure.

Digital Image Correlation (DIC) is an optical, non-contact method used to measure strains on the surface of specimens as they are loaded. In this study, DIC shear strain measurements were used to compare the bond performance of those specimens that were not exposed to weathering to matched specimens that were exposed to cyclic moisture conditions.

This research includes the study of anatomical features of Douglas-fir (*Pseudotsuga menziesii)*, a commonly used softwood species in building construction. Four adhesives, all exhibiting different penetration characteristics, were evaluated on their penetration measurements and compared to their mechanical bond performance before and after weathering. Phenol-formaldehyde (PF), one formulation with a low molecular weight, one with added fillers and extenders, and one with a high molecular weight, were assessed as the structural adhesives. Methylene diphenylene diisocyanate (MDI) was also used for comparison since it is known to easily flow and penetrate into the wood. The adhesive in this study was covalently bonded to iodine to permit differentiation by X-ray attenuation for the XCT scans, thus allowing for segmentation of the adhesive from the wood cell in the resulting tomogram. The final experiments include a comparison of the amount of penetration of the adhesive into wood (using XCT) and any moisture effects on bond performance (using DIC). Accurately assessing the role of cell wall penetration on moisture resistance is essential for the proper formulation of adhesives. Table 1 is a list of acronyms used throughout the paper and should be references as needed.

Table 1. Acronyms used throughout the paper.

EW	earlywood
LW	latewood
EL	earlywood bonded to latewood
EE	earlywood bonded to earlywood
LL	latewood bonded to latewood
CML	compound middle lamella
IPL	low molecular weight iodinated phenol-formaldehyde
IPH	high molecular weight iodinated phenol-formaldehyde
IMDI	iodinated methylene diphenylene diisocyanate
IPLFE	low molecular weight iodinated phenol-formaldehyde with added filler and extender
XCT	X-ray Computed Tomography
DIC	Digital Image Correlation
SEM	Scanning Electron Microscopy
EDS	Energy Dispersive Spectroscopy
XFM	X-ray Fluorescence Microscopy
PAA	paracetic acid
COV	coefficient of variation
FOV	field of view
AOI	area of interest
WP	weighted penetration
EP	effective penetration
Even number labels	non-weathered specimens
Odd number labels	weathered specimens

CHAPTER 2: LITERATURE REVIEW

2.1 Adhesive Penetration

The adhesive bond is a complex interphase containing an adhesive polymer that is liquid when applied to the wood surface, and polymerizes, after following the path of least resistance (Kamke & Lee, 2007). Interphase more accurately describes the bonded area than interface due to the variable anatomical features of the wood substrate. The adhesive and wood surfaces require both physical and chemical changes to provide an adequate bond (River et al., 1991). Adhesive penetration is categorized into gross penetration and cell wall penetration. Gross penetration refers to the adhesive flowing into the porous structure of the wood (cell lumens, pits, intercellular voids, and cracks). This is important for bonding because the adhesive fills any voids and creates a support to hold the two pieces of wood into one product. Cell wall penetration is infiltration of the adhesive into the wood substance before polymerization and can potentially create a mixed phase of adhesive and cell substance. Gross penetration is a common occurrence, and easily achieved by most wood adhesives. Cell wall penetration, however, is only achievable with the low molecular weight portion of the adhesive, and has been observed in previous research with MDI and low molecular weight PF adhesives (Laborie, 2002; Paris & Kamke, 2015; Stephens & Kutscha, 1987).

Having an adequate amount of adhesive penetration at the surface of the bonded wood as well as away from the bondline is essential for a strong bond between the two substrates. Over penetration into the wood, away from the bonded surface may result in a weak bond that is starved of the strength of the adhesive (River et al., 1991). A study on

penetration measurements of adhesives in beech wood showed that the saturation, rather than the penetration depth, correlated with the mechanical bond performance (Hass et al., 2012).

There is not enough clarity about the effects of adhesive penetration into the wood and the ability for the bond to resist shrinkage and swelling of the wood cell wall. The purpose of the adhesive is to bond two wood substrates together into a product, and also transfer stress across the bondline (Frihart, 2005). It is theorized that if the adhesive can penetrate into the cell wall substance and polymerize, it will create an IPN and reinforce the wood surrounding the bond (Frazier & Ni, 1998). In turn, this will aid in transferring stresses subjected to the bond and give a better overall performance of the product (Frazier & Ni, 1998; Frihart, 2006). Nanoindentation studies have proven that the elastic modulus and the hardness of the cell wall increases with penetration of the adhesive into the cell substance (Gindl & Gupta, 2002; Jakes et al., 2015).

In order to test this improvement in moisture durability with penetration theory against weathering, many aspects must be carefully considered. The macro adhesive bond performance is an important measure and gives information about the structural integrity of the bond. However, many details are ignored such as anatomical features and the performance of the area around the bonded surfaces. Therefore, this multi-scale investigation study uses the combined techniques of XCT and DIC to obtain a holistic view of the performance of the bondline when exposed to weathering.

2.2 Moisture-induced Degradation

Understanding and predicting the behaviors of wood building products after moisture exposure has been a topic of research for many years (Frihart, 2009). Studies

have been conducted on mass timber building products (Svensson et al., 2011), plywood (Li et al., 2015), and OSB (Kojima et al., 2011) after climatic exposure over short and long periods of time. Mimicking the actual conditions can be difficult and time consuming, but accelerated weathering studies have been developed to serve that purpose. Devices in place at Oregon State University, such as the Q-lab Ultraviolet (QUV) system (small scale) and Multi Chamber Modular Environmental Conditioning (MCMEC) system (large scale) can accurately control the temperature, UV light, and moisture conditions imposed on test specimens. Technology is constantly developing to monitor durability of wood products (Laleicke, 2015) because of their importance in our society. Standardized accelerated weathering procedures for engineered wood products are in place (ASTM D2559, 2012; BS EN 321, 2002; PS 1-09, 2010) but the results tend to focus on large-scale effects of specific products and are based on a pre-defined benchmark. These standards assess the resistance to shear, creep, and delamination after moisture exposure (ASTM D2559, 2012) and typically a pass/fail assessment. When multiple parameters are introduced to the study, it is difficult to understand specific implications of certain mechanisms within specimens and on the spatial scale of the adhesive bond.

Fully understanding and improving how the wood-adhesive interaction responds to moisture cycling requires more than just a strength test of a bondline that has been subjected to weathering. There are many macro, micro, and nano-scale phenomena that are overlooked with this type of study. There is a strong desire to gain a complete understanding of durable adhesive bonds (Frihart, 2005). Studies have looked at

promoting covalent bonding between the adhesive and cell wall substance by chemically modifying the cell wall, or employing a coupling agent. Attempts have been made to add coupling agents to the wood surface in order to enhance moisture durability of the bondline and prevent delamination (Vick et al., 1995). This method leaves one end of the molecule capable of reaction with a functional group in the cell wall, and the other end that is capable of reacting with a functional group on the adhesive. These modification techniques can be complex and time intensive, therefore understanding these nanometer scale cell wall and adhesive interactions are of great interest in order to eliminate the need for these modification procedures. Additional studies have concluded that having both a high and low molecular weight component of the adhesive system is preferred for decreasing moisture sorption (Jakes et al., 2015; Stephens & Kutscha, 1987). The low molecular weight component can infiltrate the cell substance to reduce moisture uptake within the cell wall, as well as migrate into each wood substrate, and the high molecular weight portion can fill any voids at the bonded interface (Jakes et al., 2015).

Comparing different categories of adhesives based on how they polymerize has indicated that durability is dependent mainly on the chemical composition of the adhesive, both based on the gross and cell wall penetration (Frihart, 2009). Polymeric diphenylmethane diisocyanate (pMDI) and phenol-formaldehyde (PF) are both common adhesives used in wood products and are considered *in situ* polymerized adhesives, since they are made of small molecules that first flow, potentially penetrate the cell wall, polymerize, and form a highly cross-linked, rigid system after curing (Frihart, 2009). pMDI is known to easily penetrate the cell substance due to its low molecular weight

(Frazier, 2002; Frazier & Ni, 1998; Sonnenschein et al., 2005). PF is considered one of the most durable adhesives when it comes to moisture resistance, despite its brittle nature and the fact that only the low molecular weight portions penetrate the cell wall (Frihart, 2009). Additional information about effects of penetration into the cell substance must be gained in order to better understand wood-adhesive-moisture behavior. Not only are adhesives typically the most expensive cost in engineered wood products, preventing degradation from moisture intrusion could save money for companies manufacturing the products, as well as claims on products in service.

2.3 Literature Review of Methods

The adhesive bond is a complex structure determined mostly by the unique morphology of the wood anatomy. Accurately visualizing and measuring the adhesive penetration and mechanical performance of the bondline requires advanced methods, especially when correlating effects of moisture resistance.

2.3.1 X-ray Computed Tomography (XCT)

Wood is an anisotropic, porous, and biological material. There is a high amount of variability within the same species of wood and even with the same piece of lumber (Kretschmann, 2010). This results in the complex adhesive interphase region, previously mentioned. A main goal of this study was to determine if there is a correlation between adhesive penetration and moisture-induced degradation, which requires a precise measurement with as few variables as possible. In order to conduct this type of moisture durability comparison, multiple steps must be examined. Light and UV microscopy studies (Gindl et al., 2004) and Scanning Electron Microscopy (SEM) (Gindl, 2001) studies have proven to easily detect adhesive penetration into the cell lumens but precise

detection of adhesive in the cell wall is difficult. SEM (Gindl, 2001), UV microscopy (Gindl et al., 2002), nanoindentation (Gindl et al., 2004; Stöckel et al., 2012), and x-ray fluorescence microscopy (XFM) (Jakes et al., 2015) experiments have successfully detected adhesive in the cell wall substance. However, these methods require damaging of the specimen to get a clean section or surface, and only give information about the 2D surface that is exposed for examination. Figure 1 shows a scanning electron micrograph (SEM) of an adhesive bondline. While the adhesive can be seen in the lumens, there is no indication of how it traveled from the applied surface, through the wood. The 3D path of the adhesive is the only true representation of the complex interaction.

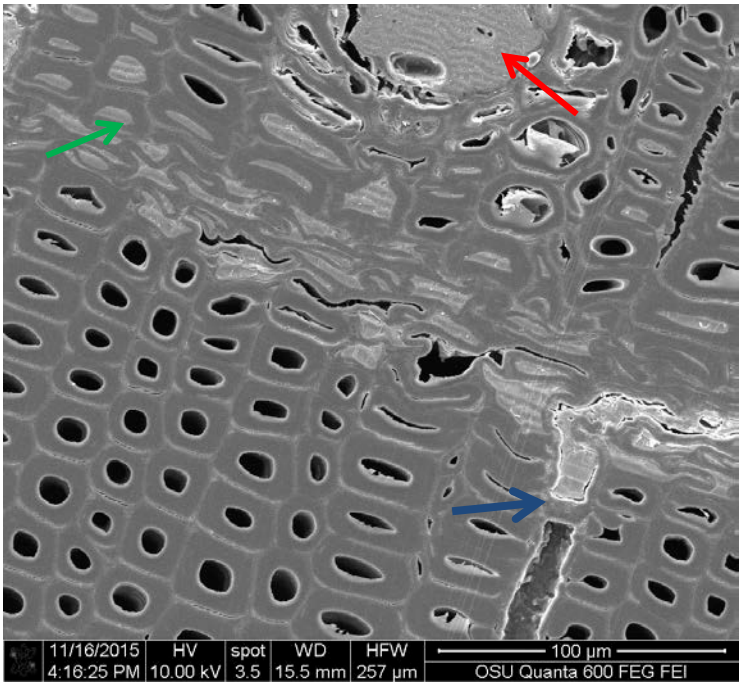

Figure 1. SEM example taken by the author of an EL-IPL sample, showing a resin canal (red arrow), cell lumens (green arrow), and a ray (blue arrow) filled with adhesive.

To accurately assess the anatomical features in biological materials at the micron scale, XCT has been successfully used to visualize the complex structure of natural

materials (Bastani et al., 2016; Evans et al., 2010; Hass et al., 2012; Mannes et al., 2010; Mayo et al., 2010; Paris, 2014; Standfest et al., 2010; Steppe et al., 2004; Trtik et al., 2007; Wildenschild et al., 2002; Zauner et al., 2012). XCT is a high resolution, 3D, non-destructive, novel method to analyze materials and potentially segment material phases within a dataset (Metscher, 2013). XCT experiments measured the amount of void spaces within MDF products to give insight on pressing parameters (Standfest et al., 2010). Dimensional changes of wood cells were monitored during moisture exposure using XCT (Derome et al., 2011; Patera et al., 2013). Zauner explored *in situ* deformations of wood using a custom mechanical test device during XCT scanning (Zauner, 2015; Zauner et al., 2012). XCT data has been used to develop models for adhesive penetration in hardwood species (Mendoza et al., 2012). XCT opens up many more opportunities for exploration, but there are a few caveats to be mindful of: time and resource limitations, specimen preparation, resolution constraints, and the large quantity of data for processing.

Being able to segment material phases becomes crucial when analyzing specimens containing multiple material properties, such as a wood composite (Evans et al., 2010; Modzel et al., 2011). Paris et al. (2014) developed a successful method for tagging adhesives with iodine in order to quantitatively segment wood cell substance from adhesive in tomograms. Jakes et al. (2015) has used a similar technique with a bromine tag for samples analyzed with x-ray fluorescence microscopy (XFM). Segmentation of the void, wood, and adhesive phases has been achieved for studying the wood-adhesive interactions (Bastani et al., 2016; Evans et al., 2010; Hass et al., 2012;

Paris & Kamke, 2015). This research follows the procedure developed by Paris et al. (2014).

There are two main types of XCT systems: cone beam and synchrotron (Kastner et al., 2010). Cone beam XCT systems use a polychromatic beam that results in lower resolution, greater noise, and reduced contrast (Kastner et al., 2010). Cone beam systems are more readily obtainable research instruments, but still trial synchrotron systems in regard to spatial resolution and beam power. Synchrotron XCT, employs a monochromatic beam that produces high spatial resolution, low noise tomograms (Hoheisel et al., 2006; Wildenschild et al., 2002). Despite the great advantages of synchrotron XCT, there are only a few government-operated facilities, with limited user programs. The synchrotron device at the Advanced Photon Source (APS), Argonne National Laboratory (ANL), Argonne, Illinois was used for this study. Beamtime at the APS is obtained via a competitive, proposal-based, General User Program.

Resolution is of great interest in studying wood since micrometer- and nanometer-scale features can impact overall properties. However, gaining resolution requires a smaller field of view (FOV), therefore a decrease in specimen size. This reduction in specimen size results in more difficultly in specimen preparation and more complexity in specimen selection. In addition, any specimen movement during scanning results in blurred tomography and low quality images. As the FOV decreases, the effects of micron movements become harder to control but equally as important to eliminate.

At the micro-XCT scale, gross and cell wall adhesive penetration was measured with a spatial resolution of 1.4 μm (Paris & Kamke, 2015). However, to gain further

information regarding penetration of adhesive into pits and cell walls, nano-XCT must be achieved. Although gaining resolution, the sample size must be reduced. Nano-XCT has been successful in visualizing samples such as mouse bone (Khoury et al., 2015; Schneider et al., 2007), electrodes in fuel cells (Shearing et al., 2011), and the pore structure of tight sandstone from reservoirs (Bin et al., 2013). To date, there have not been any studies looking at wood-adhesive interactions at the nanometer scale using XCT. This research was the first to develop these preliminary wood-adhesive, 3D adhesive penetration assessments using nano-XCT. The authors were able to obtain images at a resolution of 60 nm^3/voxel.

Both the micro- and nano-XCT systems use the same light source, but the way the beam is condensed before contacting the sample differs. Figure 2 shows a schematic of the micro-XCT beamline used in this study, and Figure 3 - Figure 4 show the nano-XCT beamline configuration. Figure 3 and Figure 4 show the complex design of the 32ID beamline, with the capillary condenser, pin hole, zone plate, and phase ring which all improve resolution and enhance the imaging of material boundaries.

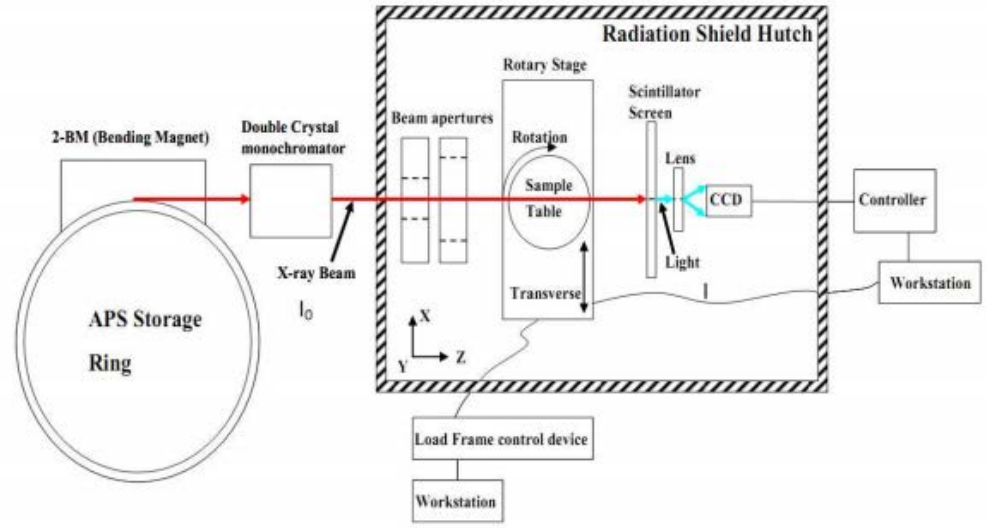

Figure 2. Schematic of the micro-XCT setup at the APS on the 2BM beamline (Subramanian et al., 2011).

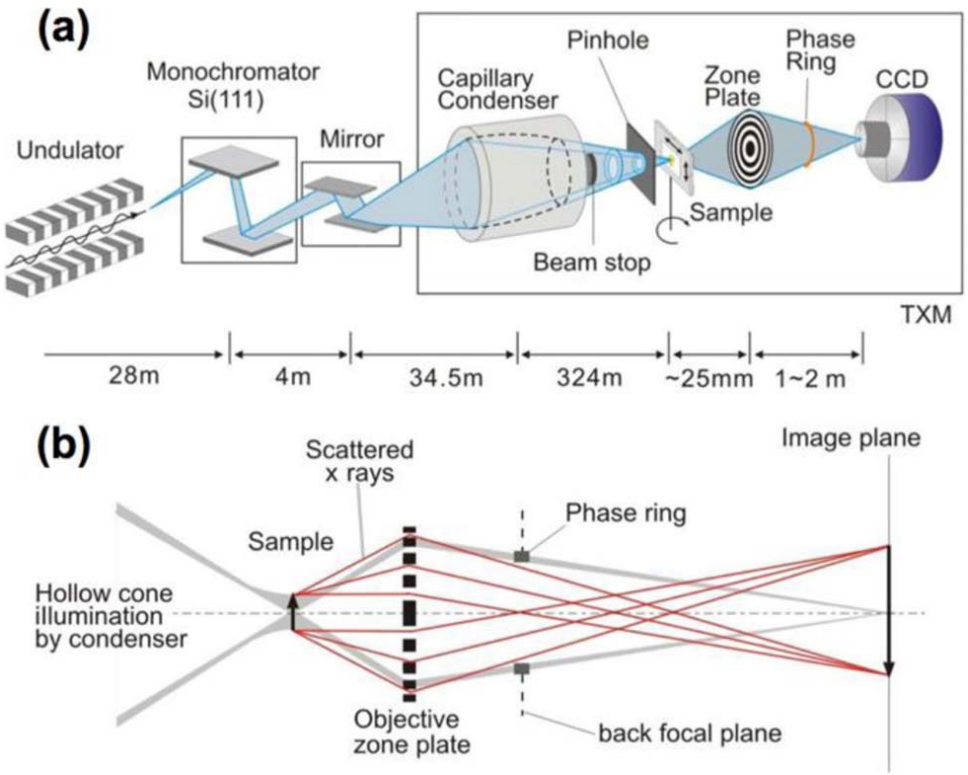

Figure 3. Schematic of the nano-XCT beamline design at the APS on the 32ID beamline (Saunders & De Andrade, 2015).

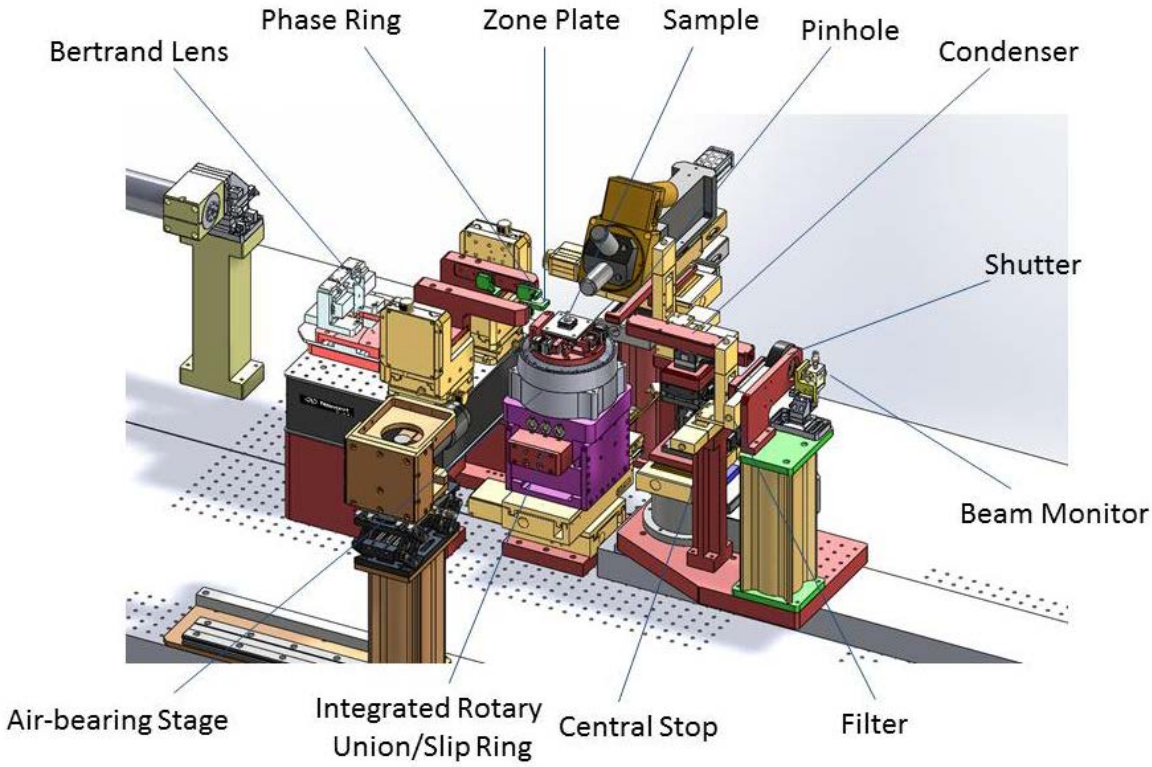

Figure 4. Schematic of nano-XCT setup at the APS on the 32ID beamline (Saunders & De Andrade, 2015).

2.3.2 Digital Image Correlation

To correlate the adhesive penetration observations with the mechanical performance and moisture resistance of a wood-adhesive bondline, lap-shear testing was conducted on each sample variation. Tension testing is extremely difficult for wood products, and often only yields a maximum load at failure, with little information about how the sample performed before failure (Serrano & Enquist, 2005). Usually these bond performance studies only tell part of the story of how the bond is performing under load. Typically, the maximum strength of the lap area is recorded, along with the percent wood vs. adhesive failure (Ammann et al., 2016; Gindl et al., 2004), giving no indicator of the

behavior up to the failure of the specimen. Extensometers can be added to the sample during the test to calculate strain within an area. Extensometers measure the total deformation of the bond along a single dimension. These devices are relatively inexpensive, easy to calibrate and use, but leave out detailed information about strain as it is being transferred across a bonded interphase. A way to visualize and calculate the strain behavior around the bonded region is needed to back up the theory of improved stress transfer across a bondline containing adhesive penetration. A study by Müller et al. (2005) investigated the effects of adhesive penetration using electronic speckle pattern interferometry, which is a technique used to track the surface deformations of a specimen during testing using a laser (Gindl & Müller, 2006; Müller et al., 2005). This is a type of non-contact measurement tool, but was not used in this study.

Digital Image Correlation (DIC) is also a technique used to measure precise surface deformations using two cameras, which track a unique pattern on the sample surface simultaneously as the sample is being loaded. The algorithm then solves for the deformations of that pattern using the collected images (Sutton et al., 2009). DIC provides more detailed information about how a sample performs throughout the duration of the test. The two-dimensional deformation data may be used to assess the transfer of strain across the bondline, which gives an indication of the stress transfer across that area. Although DIC is a more precise and detailed method of measuring strain, the equipment is expensive, requires extensive training for the use and calibration of the system, and is time consuming to both setup and analyze the data.

DIC has been successfully used to evaluate strains in solid timber materials (Zink et al., 1995), and has become a popular method for evaluating strains in wood composite panels since it is a non-contact measurement tool that can observe detailed strain fields otherwise not measurable, such as around adhesive bondline interphases (Alldritt, 2013; Way, 2015). DIC has been adapted for the study of strain distribution of adhesive bonds, in a similar manner to this study (Serrano & Enquist, 2005) and was also used to model and predict behavior of materials using finite element analysis (Schwarzkopf, 2014). The fracture mechanics of bondlines in laminated veneer lumber (LVL) after accelerated weathering were evaluated using DIC to monitor crack propagation in the bondline (Mirzaei, 2016). Stereomicroscope DIC systems allow for measurements at a higher resolution, and have been used for studies with wood plastic composite materials (Schwarzkopf, 2014). DIC is favorable for these type of studies due to the increase in information from the optical measurements. Understanding the detailed effects of adhesive penetration on the bond performance will facilitate future innovations for structural adhesive systems.

Moisture induced-degradation is complex in wood composite products due to the different properties of the wood and the adhesive. These methods are needed to assess and gain a holistic understanding of the wood and adhesive at different resolutions. XCT has proven to be successful in measuring adhesive penetration in previous work and was in this study to assess moisture durability. DIC has been used to calculate strain in wood composites and was used in this research to compare the mechanical performance of composites after weathering exposure.

CHAPTER 3: MATERIALS AND METHODS

3.1 Materials

3.1.1 Wood Species

The sapwood of Douglas-fir (*Pseudotsuga menziesii),* at approximately 12% moisture content, was used for this research. Both EW and LW regions were selected for comparison. The wood samples were solid-sawn and freshly planed immediately before adhesive application.

3.1.2 Adhesives

Four different adhesive formulations were used in this study. Each adhesive had different characteristics and should exhibit varying penetration results and potentially different moisture resistance. Three formulations of phenol-formaldehyde (PF) and one formulation of methylene diphenylene diisocyanate (MDI) were used. PF and MDI are structural adhesives that are commonly used for wood composites and are known for good water resistance. To achieve potential differences in penetration, high and low molecular weight PF formulations were prepared. The high molecular weight PF was achieved by extending the time of the resin cook procedure. The high molecular weight PF for this study had a weight average molecular weight of 28,050 g/mol and a polydispersity index of 1.135 (Arclin, Springfield, OR). This formulation will now be referred to as the high molecular weight PF (PH). The low molecular weight PF was formulated with a weight average molecular weight of 18,110 g/mol and a polydispersity index of 1.097 (Arclin, Springfield, OR). This formulation will now be referred to as the low molecular weight PF (PL). Gel permeation and ion chromatography analyses were

used to measure the molecular weight and polydispersity of each adhesive. The third PF adhesive combined the low molecular weight PF with filler and extender material, consisting of soda ash, wheat flour, and alder bark flour (Willamette Valley Company, Eugene, OR). This adhesive will now be referred to as the low molecular weight PF with added filler and extender (PLFE). In addition to modifying adhesive fluid characteristics and enhancing adhesive application, filler and extender materials provide control of penetration of the adhesive into the wood material (Frihart & Hunt, 2010).

The MDI for this study was derived from a commercial OSB resin (Rubinate M, Huntsman). MDI is known to penetrate wood easily and primarily cures by reaction with bound water in the wood. MDI resin is a mixture of oligomers that polymerize by reaction with water, polyols, and amines. The small molecular size promotes penetration throughout the bonded wood interphase.

Each adhesive required elemental tagging to create a contrast between the wood cell wall substance and the adhesive during XCT scanning. Achieving sufficient X-ray adsorption contrast between two materials depends on both the materials elemental composition and the density (Myridis, 2008). Since both the wood and adhesives are organic materials (comprised of mostly carbon, hydrogen, and oxygen) and both the cured adhesive and the cell wall have a similar density (~1.5 g/cm^3) the x-ray adsorption characteristics are similar. A tagging procedure using iodine that was previously developed for XCT experiments of bonded wood was also used for this study (Paris et al., 2014).

The PF was formulated with 100% of the phenol component replaced with meta-iodophenol. This method ensured that all PF molecules were covalently bonded with iodine, therefore no free iodine migration was possible. PF resin solids content was 44% and the PL viscosity was 125 cp and PH was 388 cp, at 25^{o}C. The MDI was also tagged with iodine, although in this case, not all MDI molecules were covalently bonded with iodine. Triodophenol was dissolved in tetrahydrofuron (THF), and then mixed with MDI under nitrogen for 24 hours at 50^{o}C (Paris et al., 2014). A calculated 10% of the NCO (isocyanate) groups were substituted with an iodine urethane group. To avoid excessive viscosity, the THF was retained in the adhesive mixture, and did not evaporate until bond formation. All adhesives will be referred to as I(x) throughout the paper, indicating they are tagged with iodine.

All of the comparisons about adhesive types from this study are meant to be fundamental findings and not intended for generalizations by adhesive type. The adhesives were modified from those formulations that are typically used in industrial practice.

3.1.3 Bonding Procedure

The sample dimensions before assembly were 64 mm x 100 mm x 6 mm (T x L x R). All IPF adhesive systems were applied at 28 mg/cm^2 based on resin solids, and the IMDI was applied at 17 mg/cm^2. The adhesive was applied to the surfaces of both lamina, at this application level, with a flat putty knife. The IPF samples were pressed for 7 minutes at 180^{o}C and 0.69 MPa. The IMDI samples were pressed for 1 hour at 100^{o}C (to remove the flammable THF) and 0.69 MPa then heated to 180^{o}C for another 10 minutes.

3.1.4 Specimen Treatments

There were two groups of weathered samples in this study. One group of samples was first reduced in size for micro-XCT scanning before weathering at the APS. These samples were scanned with micro-XCT before exposed to weathering, and then the same sample was scanned again directly after weathering. These samples will now be referred to as microweathered samples. The microweathered samples were cut from the bonded assemblies, using a small bandsaw to approximately 2 mm x 2 mm x 10 mm. The bondline was oriented to be in the center of the microweathered sample, as shown in Figure 5. The microweathered specimen replicates are listed in Table 2.

Figure 5. Micro-XCT sample with the central bondline seen as a dark line.

Table 2. Microweathered sample replicates.

Wood Species	Orientation of Lamination	Bonded Surface	Adhesive
DF	Parallel	LW:LW	IPH
DF	Parallel	EW:LW	IPH
DF	Cross (perpendicular)	EW:LW	IPH
DF	Parallel	EW:EW	IPL
DF	Parallel	EW:LW	IPL
DF	Parallel	LW:LW	IPL
DF	Cross (perpendicular)	EW:LW	IPL
DF	Parallel	EW:LW	IPLFE
DF	Parallel	EW:LW	IMDI
DF	Parallel	LW:LW	IMDI

The second group of samples was subjected to weathering at Oregon State University, using a slightly different weathering cycle technique. Half of these samples were subjected to weather cycling while the other half remained dry. These samples will now be referred to as macroweathered samples. Table 3 lists the replications for the macroweathered samples. Each group contains both weathered and non-weathered samples and all groups are bonded parallel.

Table 3. Macroweathered sample replicates.

Wood Species	Bonded Surface	Adhesive
DF	EW:EW	IPH
DF	EW:LW	IPH
DF	LW:LW	IPH
DF	EW:EW	IPL
DF	EW:LW	IPL
DF	LW:LW	IPL
DF	EW:LW	IMDI
DF	LW:LW	IMDI
DF	EW:LW	IPLFE

The dimensions of the macroweathered samples were 13 mm x 6 mm x 60 mm in a single lap-shear orientation (Figure 6). The bonded area between the notches was roughly 152 mm^2.

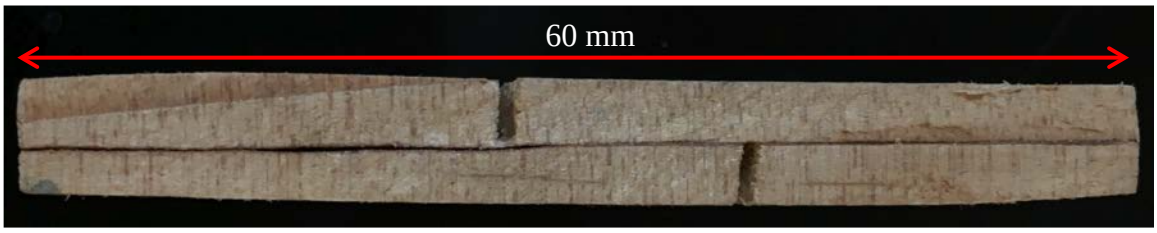

Figure 6. Macroweathered lap-shear specimen.

Table 4 is an overview of the specimen types with their respective methods. The microweathered experiment included two EL-IPL samples and two EL-IPH samples, one of each was parallel laminated and the other was cross-laminated.

Table 4. Specimens with respective methods for analysis; all samples in table are parallel laminated.

Sample	Lap-shear Analysis	EDS Analysis	XFM Analysis	Micro-XCT Analysis	Nano-XCT Analysis
EE-IPL	10	1	-	4	3
LL-IPL	10			-	-
EL-IPL	7			1	-
EE-IPH	9	1	7	2	-
LL-IPH	10			-	-
EL-IPH	9			3	-
EL-IMDI	8	2	5	-	-
LL-IMDI	4			-	-
EL-IPLFE	8	-	-	-	-

3.2 Methods

3.2.1 Weathering Cycles

To visualize internal cracking and adhesive penetration throughout the sample, all of the microweathered specimens were scanned using micro-XCT before and after accelerated weathering. These samples were subjected to weathering at a size of 2 mm x 2 mm x 10 mm. The weathering procedure was conducted at the APS and consisted of five cycles. Each cycle included water soak for 30 minutes at room temperature at approximately 20 kPa absolute pressure, followed by drying for 30 minutes in an air stream at 70°C and less than 1% relative humidity. The specimens were allowed to equilibrate to the APS laboratory conditions for approximately 12 hours after weathering and before the second round of XCT scanning.

To determine any mechanical bond performance variations in samples subjected to moisture exposure, half of the macroweathered specimens were subjected to a weathering cycle based on a modified ASTM D2559 technique and the other half remained non-weathered (ASTM D2559, 2012). Weathered specimens were placed in a vacuum desiccator and completely submerged in warm tap water (approximately 27ºC) by a porcelain plate (Figure 7). A vacuum was pulled for 3 minutes in an attempt to remove air from the lumens and voids in the sample. The vacuum was turned off for 1 minute to force the water into the sample. This procedure was repeated until there were no more visible air bubbles being removed from the samples. The pressure was held in the desiccator at approximately 20 kPa for 15 hours. The samples were then removed from the water and placed 25 mm apart in a convection oven at 75ºC for 9 hours.

Figure 7. Desiccator used for vacuum pressure water soak on macroweathered specimens.

Once removed from the oven, each specimen was checked for delamination or cracks and the cycle was repeated for a total of five times. Some specimens were removed from the cyclic weathering procedure due to major delamination such as shown in Figure 8. A total of 5 macroweathered samples were removed from the study due to delamination during weathering. These samples will be considered during the statistical analysis of the mechanical bond performance. After the weathering cycles, specimens were stored in a controlled environment chamber maintained at 20 ºC and 65% relative humidity until they reached equilibrium, prior to mechanical testing.

Figure 8. Example of delaminated macroweathered IMDI sample after three weathering cycles.

3.2.2 Mechanical Testing

The matched dry and macroweathered specimens were tested in lap-shear mode and evaluated using a stereomicroscope Digital Image Correlation (DIC) system (Correlated Solutions, Columbia, SC). The notches located near the center of the sample provide stress concentrations to induce shear failure at the bonded interphase. That area was analyzed using DIC. The area between the notches was cleaned using a sledge microtome. This cleaned surface was imaged prior to weathering, using a Nikon E400 epi-fluorescence microscope under UV light (Figure 9). These images were used as a comparison with the DIC images to identify any behavior in the DIC measurements that correlated to anatomical features. Additional light micrographs were captured on some samples (Figure 10) as an additional reference.

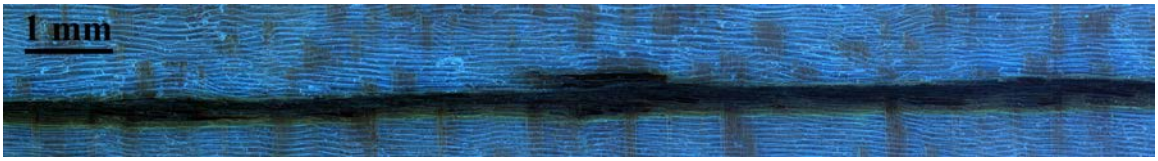

Figure 9. Fluorescence micrograph of area between notches of macroweathered IPF specimen; bondline is oriented horizontally in radial-longitudinal plane, and IPF appears dark green/brown.

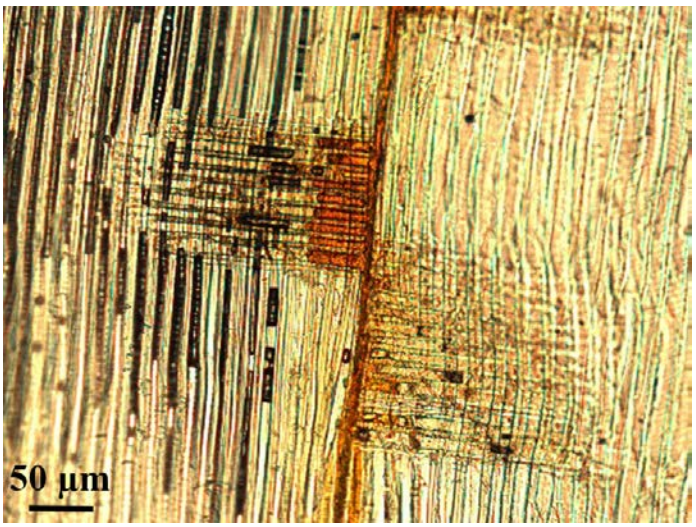

Figure 10. Micrograph of IPF bondline.

The first round of testing was conducted on an Instron E1000 universal test machine with a 1 kN load cell (Figure 11). Care was taken in the test setup to reduce eccentricity of the load. Due to the specimen dimensions and the design of the serrated grips available for the Instron E1000, there was difficulty with proper tension testing of the first group of samples. The specimen was slipping out of the test grips, and not completing the test to failure. DIC data was still collected for these twenty samples, but no maximum load could be recorded due to the slippage.

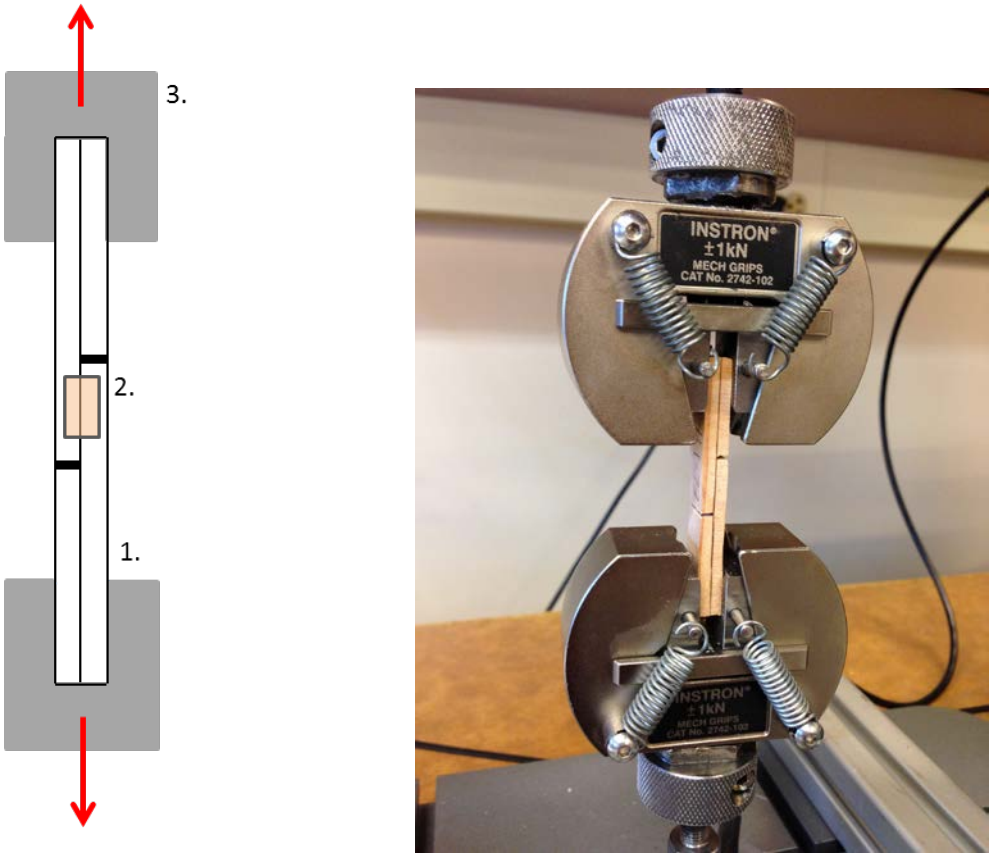

Figure 11. Illustration of the Instron E1000 test setup with 1) lap-shear test specimen; 2) area of interest (AOI) used for DIC analysis; 3) Instron serrated test grip and direction of loading on the left; lap-shear specimen in the grips on the right.

Nine of these specimens were tested on another universal test machine (Sintech) equipped with a 5 kN load cell. The Sintech had larger grips and deeper serrations, but the ends were crushed from too much pressure of the grips and the deep grooves from the serrations. An additional notch was created on five of the test specimens to see if creating a smaller lap shear area would create a lower failure load and therefore fix the gripping issue. This did not resolve the issue, and specimens still crushed in the grips, seen in Figure 12.

Figure 12. Sintech universal test machine showing the problem with a crushed specimen.

In order to eliminate this issue of the specimens crushing in the grips, two carbon fiber pieces were added to each end of the specimen as an extension tab that could then be gripped. The uniaxial carbon fiber tabs were manufactured in the lab using a small hot press. Two sheets of pre-impregnated carbon fiber were pressed together with the fibers oriented parallel to each other. They were cured using a pressure of 34 MPa for one hour, with press platen temperatures of 55^{o}C. The cured, two layer carbon fiber sheets were then cut using a shearing tool into smaller strips of 14 mm x 80 mm. The carbon fiber tabs were glued to the end of the samples using a two part steel reinforced, JB Weld

epoxy (Original Cold Weld Formula, USA). The tabs were clamped to the samples using large paper clips and left to cure overnight.

For the test, a small piece of aluminum was placed between the carbon fiber tabs, inside the serrated grips to prevent the tabs from delaminating from the surface of the sample, seen in Figure 13. The air-actuated grips were tightened using an air pressure of 0.41 MPa.

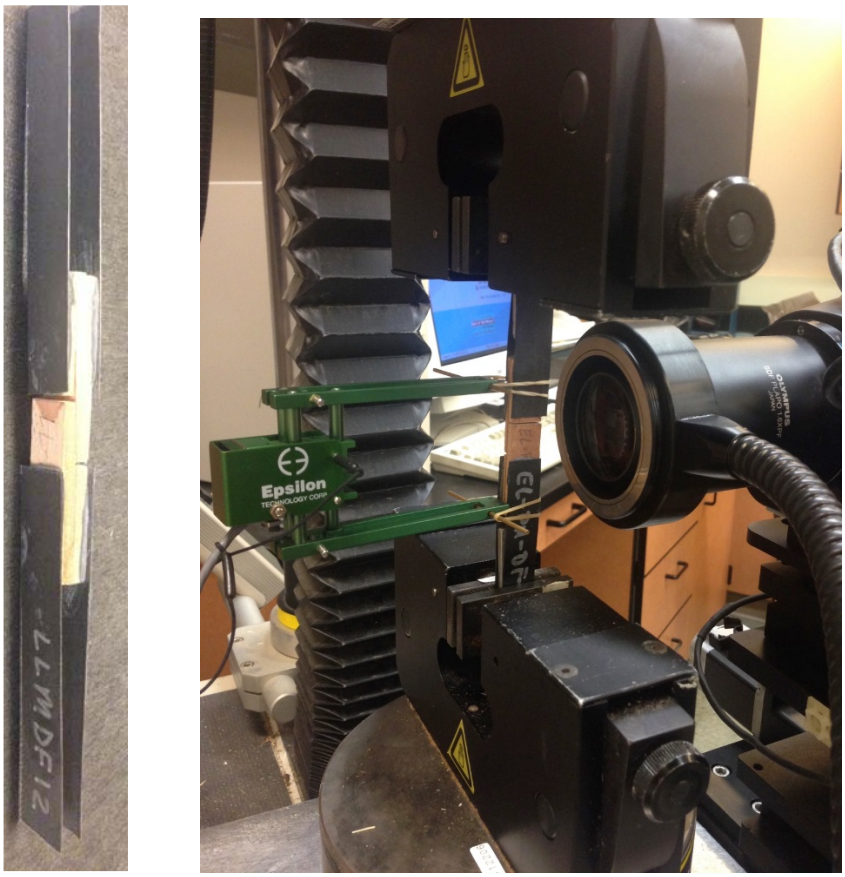

Figure 13. Specimen with carbon fiber tabs shown on the left; specimen held in grips on Sintech test machine with the clip gauge attached to the back of the specimen and the stereomicroscope DIC system with the gooseneck light shown on the right.

The lap-shear test was conducted at a displacement rate of 0.4 mm/min. The lap-shear configuration creates a shearing effect on the bondline, which is what will be

measured. The bondline creates this shear stress transfer between the wood pieces. An extensometer displacement clip gauge was calibrated and attached to the back side of the specimen, which recorded the change in specimen length throughout the test. The crosshead displacement was also recorded. The crosshead displacement is a sum of total specimen length extension, slack in the test setup, and movement of the fixtures relative to the samples. Hence, crosshead displacement can be unreliable for samples of this scale.

Careful notes were taken during the tests and any abnormal behavior was specifically noted. Location of the notches were not recorded. This would be beneficial for a future study, as a point of reference. Images were taken of the failed samples and then categorized based on the type of failure: failure between the notched area; failure only outside the notched area; failure both inside and outside the notches; failure directly at the notch, in the wood only. The failed surfaces were also analyzed to quantify the amount of wood vs. adhesive failure, using digital image processing and analysis (ImageJ, US National Institute of Health). Methods followed ASTM D5266, the standard for assessing percent wood failure (ASTM D5266, 2013). Images were taken of each failed, bonded surface, using fiber-optic gooseneck lights to provide uniform, shadow-free illumination for the three IPF formulations (Figure 14). The IMDI samples did not provide contrast between the wood and adhesive and therefore were stained using 1% safranin in 50% ethanol, and rinsed in distilled water. The imaged surfaces were then run through a macro in ImageJ that segmented the 8-bit grayscale image into percent wood failure vs. adhesive failure.

Figure 14. Failed surfaces of lap-shear area after failure of IPH sample.

3.2.3 Digital Image Correlation

In addition to recording the load and displacement of the sample, a stereomicroscope DIC system by Correlated Solutions (Columbia, SC) was used to capture one image per second throughout the duration of the test. DIC allows for a non-contact, optical measurement of two-dimensional deformation at a high resolution, in a selected field of view. In order to track movements on the surface of the sample, a random speckle pattern was applied to the previously smoothed, microtomed surface. The speckle pattern must be random, unique, and distinct for proper strain analysis (Sutton et al., 2009). The speckle pattern was created using an air deposition technique developed by Schwarzkopf (2013) using toner powder from a black ink cartridge (Schwarzkopf et al., 2013). The device is shown in Figure 15. Air was forced into the closed container, directly above a Petri dish filled with the ink toner. The toner became airborne, moved across the middle barrier, and settled evenly and smoothly across the surface of the wood sample.

Figure 15. Air deposition speckle pattern application using ink toner; red arrow pointing at specimen.

The sample was then carefully placed in an oven at 103ºC for 15 minutes to allow the ink pattern to fix onto the sample. The sample was stored in a controlled environment chamber maintained at 20 ºC and 65% relative humidity until reaching equilibrium, prior to mechanical testing. The low temperature and short amount of time in the oven should not affect any of the properties of the composite specimen. Allowing the ink to heat and fix onto the specimen is a critical step to ensure that the speckle pattern does not smear and lose contrast, as well as insuring that the speckle stays intact on the surface throughout the entire test. If there is a brittle failure and the ink toner is not fixed to the surface, it can “pop” off and the reference location is lost. In addition, if the speckle pattern moves independent of the sample, incorrect strain measurements will be recorded.

Appropriate lighting is crucial to obtain adequate contrast between the unique speckle pattern and the wood surface, so a fiber optic gooseneck lamp with a circular

fixture was attached onto the front of the stereomicroscope to provide uniform lighting. Even the slightest external movements of the DIC system can cause noise during the acquisition of the images. Therefore, the DIC test apparatus was mounted to a rigid, custom-built, aluminum t-slot cart with locking wheels and lead weights attached to the base to provide stability and reduce vibration during the test, (Figure 17). Before testing, the DIC system was calibrated using specific tools provided by the manufacturer (Correlated Solutions).

The calibration includes a distortion correction, which involves tracking a glass slide with a printed speckle pattern. The distortion correction adjusts any internal camera distortions. The target calibration then references the location of the camera to the sample being tested (Figure 16). Both of these steps must be successfully completed before testing can begin. Once the DIC system is fully calibrated, the rigid equipment cannot be moved, or else the calibration steps must be repeated. At such a high resolution and small scale, any change in the system setup can alter the data analysis.

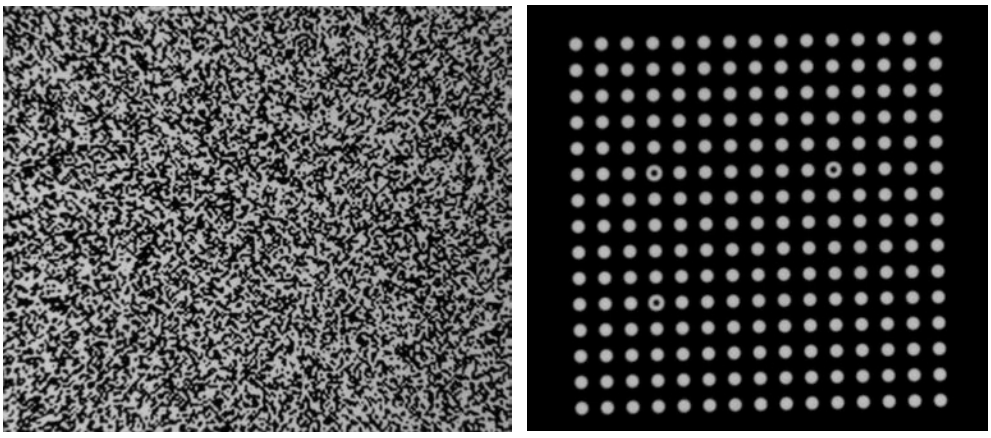

Figure 16. DIC distortion correction speckle pattern shown on the left; calibration target shown on the right.

The DIC FOV was roughly 7 mm x 7 mm and the spatial resolution was 3.2^2 µm/pixel. The extensometer and load cell data were logged to the DIC software throughout the duration of the test. This allowed for a synchronized recording of the image, with overall specimen displacement and applied load throughout the test.

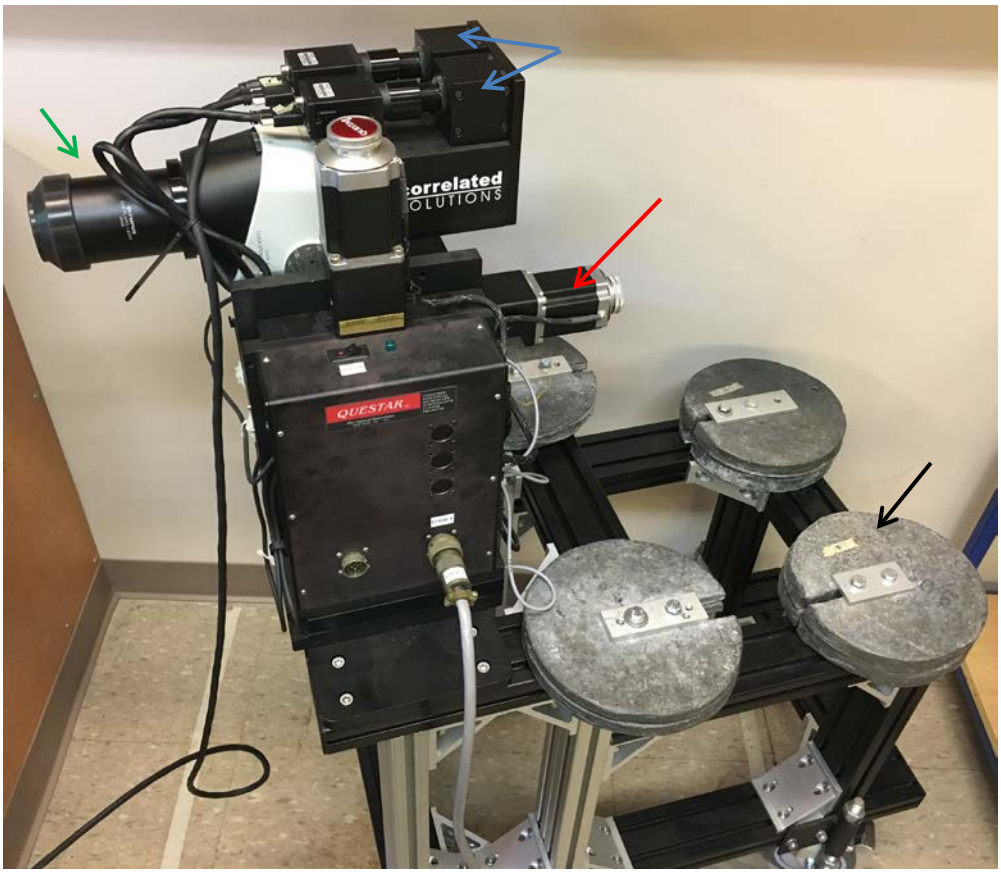

Figure 17. DIC stereomicroscope equipment on weighted cart; green arrow indicates microscope; blue arrows indicate cameras; red arrow indicates stage; black arrow indicates weighted cart.

The captured DIC images were analyzed using VIC 3D analytical software (Correlated Solutions, Columbia, SC). DIC was used to measure displacement around the bonded interphase for each macroweathered sample. The area of interest (AOI) was manually chosen to contain a central bondline, with a width of 2.56 mm and a height of

5.12 mm, and was kept consistent across all samples. This AOI was chosen in attempt to eliminate any noise related to variability within specimens and to keep a consistent AOI throughout the duration of the test, even if the specimen moved out of the FOV. Two start points were chosen, one on each side of the bondline, to ensure convergence across the whole sample during the analysis (Figure 18).

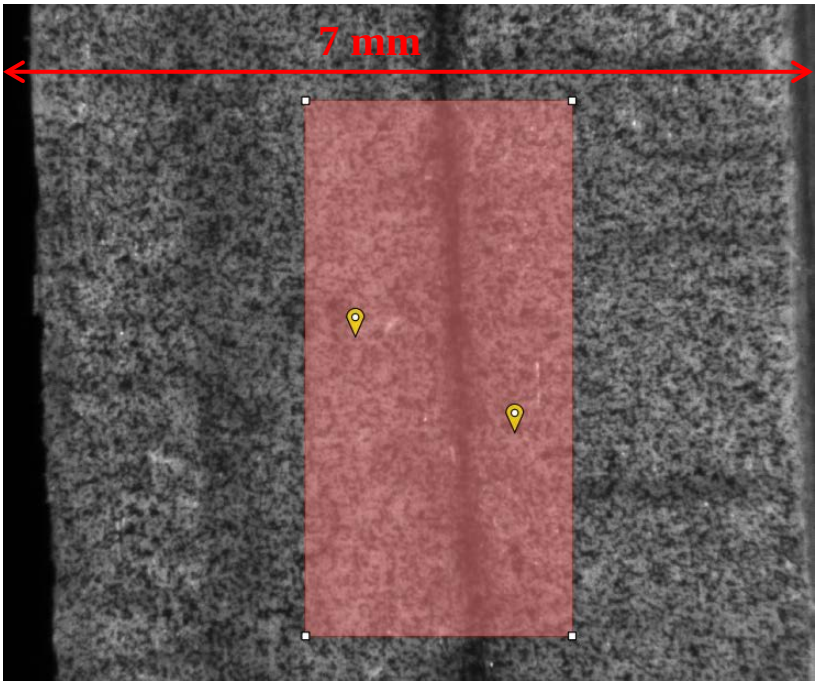

Figure 18. Example of the selected AOI and reference points across a speckled specimen.

The shear strain was calculated using the Lagrangian finite strain tensor approximation within VIC 3D. After matching the corresponding calibration information, the images were analyzed using a subset size of 49 and a step size of 11. The subset size defines the neighboring pixels around each unique point to analyze and the step size defines the number of pixels the algorithm moves through to define each unique point. The subset and step size should be chosen based on the specimen size and speckle pattern fineness. The step size should be roughly one quarter of the subset size to yield adequate

convergence (Sutton et al., 2009). In the pre-processing tool, a consistency threshold of 0.10 was used, a confidence margin of 0.20, and a matchability factor of 0.20. These values were determined based on trial and error and from information found in the VIC 3D Correlated Solutions documentation.

The shear strain (ε_{xy}) output was then exported to a .csv file, with each point (within the AOI) containing a shear strain value. Since the AOI includes the two sides of the bondline being pulled in opposing directions, every value in each image was converted to an absolute value in RStudio (ver. R 3.2.3) (RStudio, 2015). The average was calculated for each resulting magnitude shear strain value for every image captured throughout the test. That average shear strain for that particular loading point was used to create stress vs. shear strain comparisons for each sample. This data was ultimately used for the statistical analysis, although the Sintech and clip gauge data were used to verify certain unusual behaviors found in some of the DIC results.

3.2.4 Mechanical Test Statistical Analysis

Various methods were used to measure the results from the macroweathered tension tests: Sintech test machine load and crosshead displacement data; channeled Sintech load data and extensometer clip gauge displacement data (one recording per second to match the DIC images); channeled Sintech load data and DIC shear strain measurements of the AOI. Section 4.1 reports the statistical analysis using both techniques. The energy/work of the bondline was calculated, along with the effective shear modulus. Energy was chosen to represent the performance of the bondline because it includes both the force (or stress) the sample is able to withstand, as well as the deflection (or strain) induced during the test. In this study, the energy was found by

integrating the stress vs. shear strain curve. In the initial calculations, the energy was measured up to proportional limit for all samples. The proportional limit was defined as the point at which the sample transitioned from the linear (elastic) region, which was determined using a change in R^2 method. R^2 is defined as the coefficient of determination which is a measure of how well data fits to a model, in this case, a straight line. The R^2 was calculated for every point along the linear region, starting at 20% of the maximum load and continuously fitting a line to the subsequent data points. Once a maximum R^2 was reached, the proportional limit was identified. Due to some mechanical testing behaviors during the tension test, the author decided that the proportional limit was not a consistent measurement and therefore could not be used to compare against sample groups. The energy to failure was also calculated, where failure is defined as 80% of the maximum load, after maximum load. Some samples failed outside of the notched area, which is not how the test is designed. It can be assumed that the strength of the bondline is at least that of the recorded value for these samples. The energy to failure was calculated for every sample and a statistical analysis was conducted on both sets of samples: all samples and only those that failed within the notched area.

In addition, an effective shear modulus of the bondline was calculated to measure the apparent stiffness of the bonded interphase. The effective shear modulus gives information about how stiff the bonded interphase is based on the slope in the linear region of the stress vs. strain curve. The effective shear modulus was also used as an evaluation of the performance of the bonded area. Effective shear modulus is the slope of the linear region of the stress vs. shear strain curve. The linear region was defined as 20%

of the maximum load up to 80% of the previously identified proportional limit. All samples (those that failed within the notched area and those that failed outside the notched area) will be considered in all of the modulus calculations, since stiffness is a measurement in the elastic region. All of the measurement techniques were evaluated to decide the best measurement of the bondline performance and ultimately the DIC data was used for the final conclusion. DIC is the only method that can measure the shear strain.

A statistical analysis was conducted in RStudio (ver. R 3.2.3) with a three-way Analysis of Variance (ANOVA) test and a Least Squares Means (LSM) test (RStudio, 2015) to determine differences in weathering. The statistics were conducted for the failure load, effective shear modulus, and energy to failure. An α-priori of 0.10 was used to report significant differences. Based on the residual plots and to justify the assumptions, the data was log-transformed. The main objective was to detect significant differences in weathered vs. non-weathered for adhesive types.

The three-way ANOVA test takes into account any possible interaction within samples, including the three-way interaction of bonded wood surface, adhesive, and weathering. However, for a direct analysis of the effect of weathering on each interaction, a pairwise comparison was conducted using a LSM test on each measurement. The effect of weathering on the bonded wood surface was analyzed. This test only included those samples that were bonded with IPL and IPH, since they were the only sample groups that included all three possible bonded wood surfaces (Table 2 and Table 3). The effect of

weathering on the adhesive was compared using only the EL samples, since they were the only sample groups that included all four adhesive formulations.

3.2.5 Micro X-ray Computed Tomography

To compliment the mechanical test results, micro-XCT was conducted on bonded samples. The XCT results give information about anatomical features within the samples, and adhesive penetration in lumens and in the cell substance, for each adhesive type. All of the XCT scanning was performed at Argonne National Laboratory, at the Advanced Photon Source (APS). The micro-XCT scanning was performed on APS 2BM beamline (Figure 19). Beamtime at the APS is limited and therefore the number of scans attempted was based on the allocated time provided through the competitive General User Program. For both of the micro-XCT experiments, beamline scientist Dr. Xianghui Xiao provided assistance on operation of the beamline and on the appropriate scanning parameters.

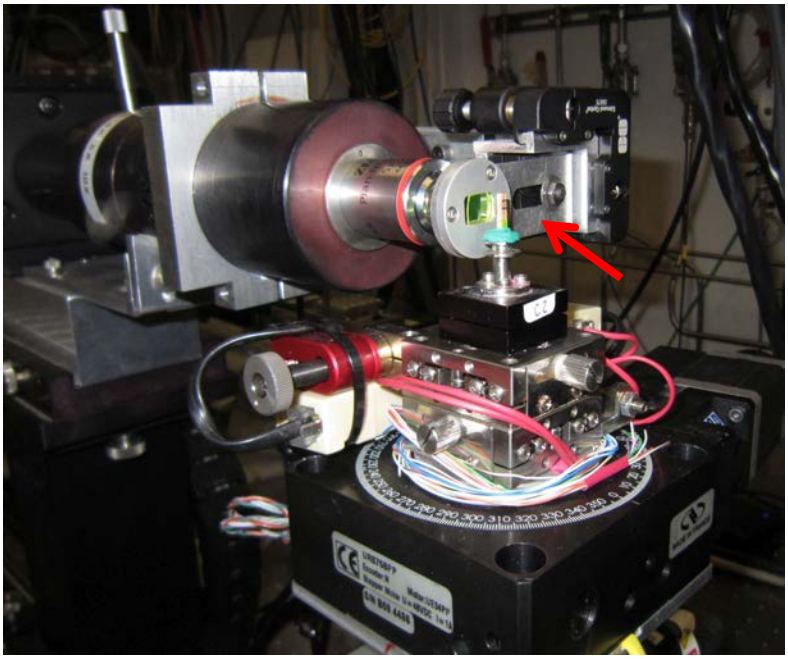

Figure 19. APS 2BM beamline hutch; sample on rotating stage (arrow).

The microweathered XCT specimens were bonded and weathered according to the details listed previously. All of the microweathered samples were scanned before any moisture exposure and then subjected to the weathering regime before the second round of scanning. The scanning parameters are listed in Table 5. The tomograms were reconstructed based on adsorption contrast with fast filtered back projection algorithms (Dowd et al., 1999; Haibel, 2008). The reconstructions were stored as image stacks (cross-section view) of floating point grayscale slices. The microweathered specimens were qualitatively analyzed in FIJI (Schindelin et al., 2012) to compare internal microcracking between the IPL and IPH specimens.

After the mechanical testing of the matched dry and macroweathered specimens, the samples were cut into smaller sections to be scanned at the APS. The micro-XCT samples were cut from a region outside the notched lap-shear area, where the sample was not damaged from the mechanical testing. A small bandsaw was used to cut the 2 mm x 2 mm x 10 mm samples, with a central bondline. Due to the small size of the sample, a push stick was used to clip the sample onto and maneuver it through the bandsaw to keep it steady. A piece of veneer was clamped to the base of the bandsaw since the clearance opening was too large and the sample would fall through once cut (Figure 20). The new macroweathered, micro-XCT samples were stored in a small bag and labeled with the original specimen code.

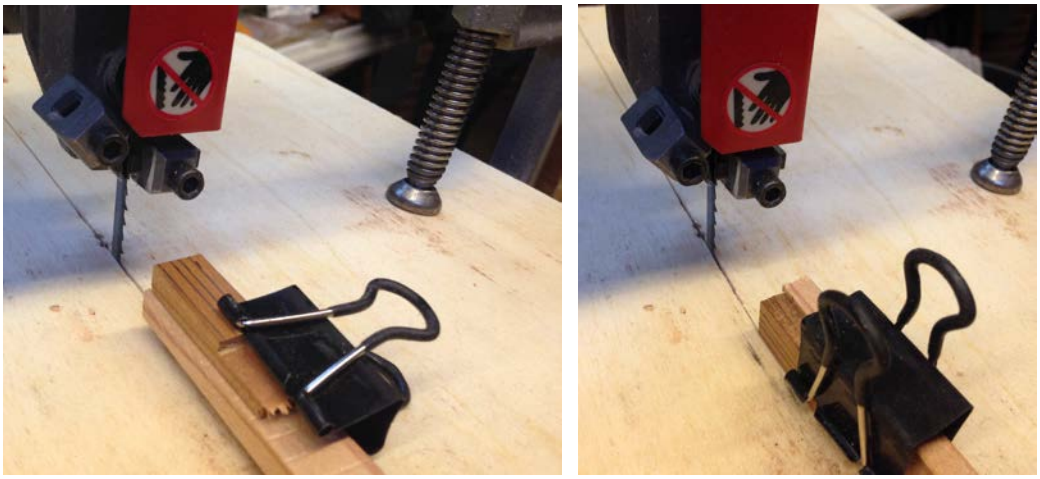

Figure 20. Preparation of the macroweathered, micro-XCT samples on the bandsaw.

The micro-XCT samples were then measured using a caliper to ensure that the dimensions did not exceed 2 mm in either diagonal. If the sample exceeds the FOV of the rotational stage, the resulting tomograms appear blurry. Therefore any edges that were slightly too large were carefully removed using a razor blade. The specimens were labeled using a color scheme and marked on one end, which was the end that sat in the specimen holder at the APS, and thus marked the bottom of the specimen with respect to the XCT data. A color was assigned to each adhesive and each bonded wood surface. A small number was written in pencil on the side of the specimen to indicate the master sample it was cut from. They were then placed in a small container with a screw-on lid. Both the lid and the base of the container were marked with the specimen code. Once at the APS, the containers were opened so that the specimens could equilibrate to the laboratory environment overnight before scanning. Scanning parameters for the APS 2BM beamline are listed in Table 5.

Table 5. Scanning parameters for APS 2BM beamline for the microweathered and macroweathered experiments.

	Microweathered experiment	**Macroweathered experiment**
Beam energy (KeV)	15.5	25
Exposure time (ms)	300	150
Total scan time (min)	25	7
Number of images collected	1500	1500
Rotation increment between images (º)	0.12	0.12
Scintillator film to specimen distance (mm)	8	50
Field of view (mm^3)	2.97 x 2.97 x 2.97	3.33 x 3.33 x 2.77
Resolution (μm^3)	1.45 x 1.45 x 1.45	1.34 x 1.34 x 1.34

Tomograms from the macroweathered specimens were reconstructed using TomoPy version 0.0.3 (Gürsoy et al., 2014) using phase retrieval. The reconstruction algorithm contains many functions in order to provide the best image quality to be used for segmentation. These functions include ring removal, zinger removal, and locating the center. The reconstructed slices (cross-section views) were stored as 32-bit, floating point grayscale images. Phase contrast imaging was selected for the macroweathered experiment in an attempt to improve contrast between cell wall substance and adhesive. To enhance the contribution of phase retrieval, a greater distance between the specimen and scintillator film was used. The macroweathered experiment was conducted at the same time as another experiment, and used some of the specimens. The other experiment was time-sensitive, and thus reducing the scan time was desired. Consequently, higher beam energy and shorter exposure time were used for the macroweathered experiment compared to the microweathered experiment.

In order to quantitatively measure the amount of adhesive penetration in the cell substance, the distribution of grayscale values must be fit to the appropriate phases within

the sample. These phases (listed in increasing grayscale value) include a peak for the void air space, wood substance, adhesive penetration into the cell substance, and pure adhesive (Figure 21).

The author attempted using a multimodal Gaussian package in RStudio called mixtools to fit the grayscale distributions to appropriate phases, but MATLAB (ver. R2015b, The MathWorks Inc., Natick, MA) was ultimately used due to the variety of built in packages for image analysis and the ability to easily manipulate datasets. The reconstructed datasets were first manipulated using FIJI (Schindelin et al., 2012) and MATLAB was used to crop, segment, and calculate the effective (EP) and weighted penetration (WP) for each sample.

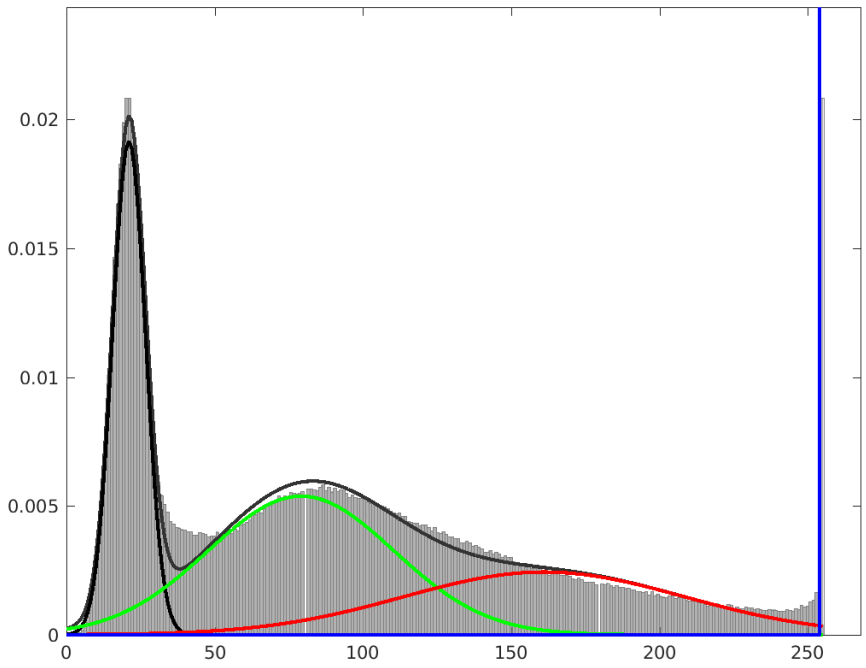

Figure 21. Segmentation of the multi-Gaussian grayscale distribution; black is void, green is wood substance, red is adhesive penetration into the cell substance, blue is pure adhesive; the x-axis represents the 8-bit grayscale values.

Each tomogram was first rotated so that the bondline was horizontal. Then, the sample was cropped so that just the void space surrounding the sample was removed. The selected 8-bit subset volume was then run through the MATLAB script, which identifies random areas that contain adhesive (based on high grayscale values) and fits the four distributions to the full volume, based on the probability that the range of grayscale values will be assigned to a certain phase within the volume. To detect the three phases on the upper end of the grayscale range, a power law gamma transform was used.

The number of peaks was fit to four distributions. Sometimes x-ray diffraction, which leaves a dark circle lining the LW cell wall lumens, or crushed EW cells, caused smaller side peaks on the phases. X-ray diffraction is caused where two substances of varying density meet. If the sample contains mainly LW cells, the volume can appear to have a small, additional peak that lies within the lower end of the void space. The crushed EW cells appear slightly darker than the cell substance grayscale values but lighter than the void, due to the mixture of the cell and void appearing as one phase.

Once the appropriate phases are identified, a bondline “plane” is chosen throughout the volume (Figure 22). The plane of the bondline is needed to calculate the EP and WP of the sample. The plane is chosen manually using the multi-point tool in FIJI (Schindelin et al., 2012). Twenty-five points were chosen along the distance of the bonded interphase, at five image slices throughout the volume. This matrix of coordinates was saved in a .csv file and input into an additional MATLAB script which calculated the EP and WP of that sample.

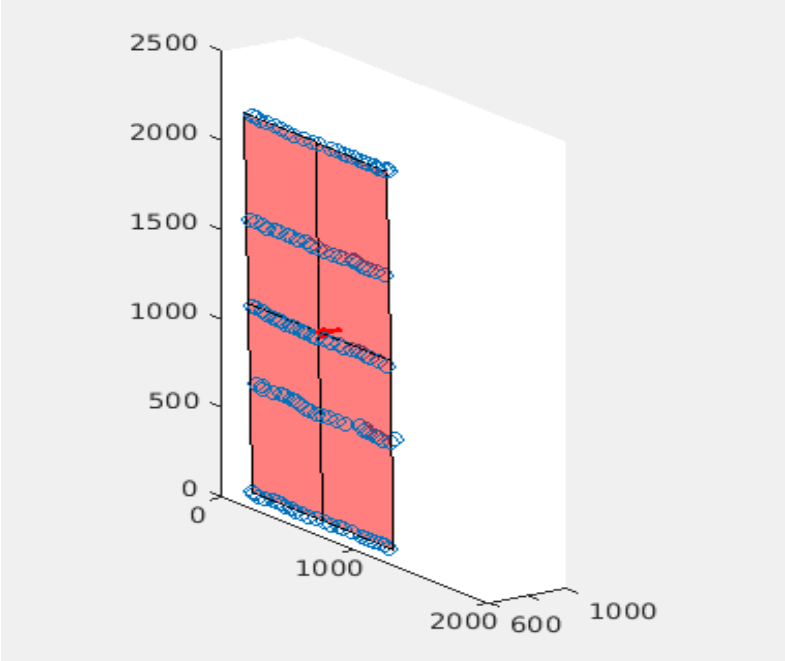

Figure 22. Plane picking of the bondline within the micro-XCT dataset.

Equations for the EP and WP calculations are shown below:

$$Effective\ Penetration = \frac{\sum A_i}{X_{image}}$$

$$Weighted\ Penetration = \sqrt{\frac{\sum {Y_i}^2 A_i}{\sum A_i}}$$

where A_i is the area of an adhesive element, measured in voxels^2, X_{image} is the width of the image (in voxels), and Y_i is the distance from the centroid for each A_i object from the identified bonded interface (Paris & Kamke, 2015). Both the pure adhesive and the adhesive penetration into the cell wall phases were used to calculate the EP and WP. An island removal technique was used to filter any artifacts from the specimen that were not adhesive. Often the compound middle lamella (CML) has a higher x-ray attenuation than the rest of the cell substance. Objects with an area of less than 100 pixels and connected

by 8 neighboring pixels were removed. Paris previously used these methods in his study of adhesive penetration into different wood species (Paris & Kamke, 2015).

During the macroweathering micro-XCT experiment, the IMDI samples did not provide sufficient contrast between the wood substance and adhesive. However, the IPL and IPH samples did provide sufficient contrast for segmentation. Since the two adhesive systems were tagged with iodine using different procedures, the author was skeptical about the tag efficacy and mobility of the iodine. Complementary analyses using EDS and XFM were conducted and are discussed in sections 3.2.7 and 3.2.8.

3.2.6 Nano X-ray Computed Tomography

Nano-XCT experiments were conducted at the APS beamline 32 ID, with a much higher resolution than the micro-XCT experiments. This is the highest resolution hard x-ray beam in the world (Wang, 2015). High spatial resolution was needed to resolve fine details in the cell wall and pit structure. In addition, it was desired to observe evidence of adhesive penetration into the cell wall. Although gaining higher resolution, specimen size is sacrificed. The nano-XCT specimens were 40 μm x 40 μm in cross-section and roughly 150-200 μm long. Since XCT is a non-destructive test, the nano-XCT specimens were sectioned from the previously scanned, macroweathered, micro-XCT samples.

A group of 5-8 cells was located within the micro-XCT dataset and was cropped, duplicated, and saved in FIJI (Schindelin et al., 2012) as a reference. Images were taken of the micro-XCT samples using a light and fluorescence microscope (Nikon E400 epi-fluorescence microscope with white light and UV light) to locate any anatomical features of interest. Features that could be identified and matched with the XCT dataset were used as reference points. Adding a fiducial marker to the samples would have made the

procedure much easier, and should be highly considered for any future nano-XCT and micro-XCT data matching. The same area was then located on the physical sample and within the micro-XCT dataset. Careful notetaking and measurements were crucial to ensure that the location of micron size features matched with the physical sample.

The nano-XCT specimens were prepared using an ultra-microtome and razorblade. Using the specimen holder for the ultra-microtome (Leica EM UC7, Vienna, Austria), samples were carefully mounted upright and the cross-section was cleaned using a handheld razor blade and the glass knife on the ultra-microtome (Figure 23). No more than 100 μm was removed from the surface of the cross section, just enough to distinguish features. Images were taken again of the sample surface before any further sectioning was made (Figure 24). The sample was then placed under the fluorescence microscope with UV light, where the thickness of the bondline, thickness of wood on either side of the bondline, and any external anatomical features were measured and captured in a digital image (Figure 25). It was essential to match up the location of the nano-XCT samples within the micro-XCT dataset. This information was then used to cut the nano-XCT samples within the micro-XCT specimen using a handheld razorblade. A region within the micro-XCT specimen that contained adhesive was selected.

Figure 23. Leica EM UC7 ultra-microtome; red arrow indicates sample in chuck; green arrow indicates knife holder.

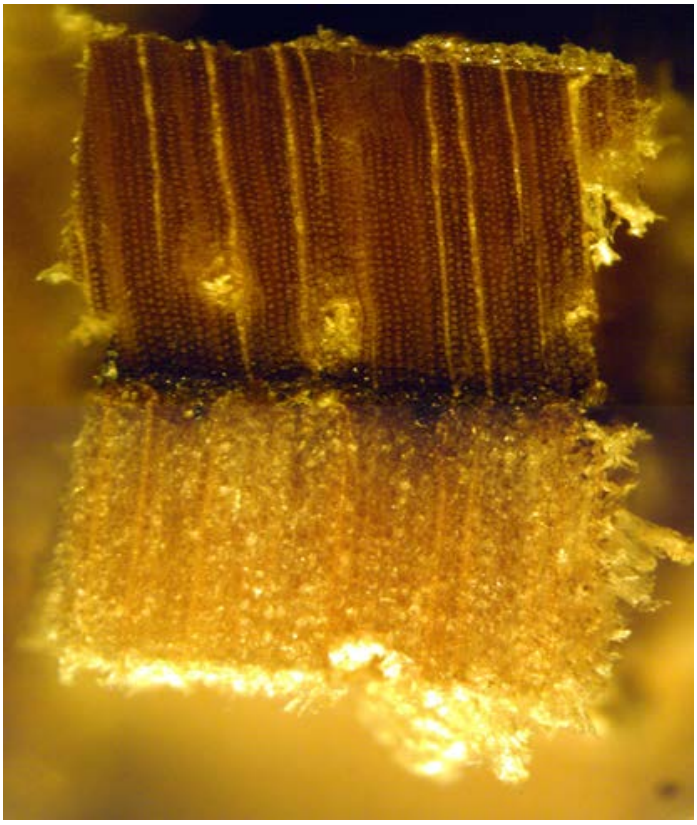

Figure 24. Cross-section (2 mm x 2 mm) of previously scanned micro-XCT specimen.

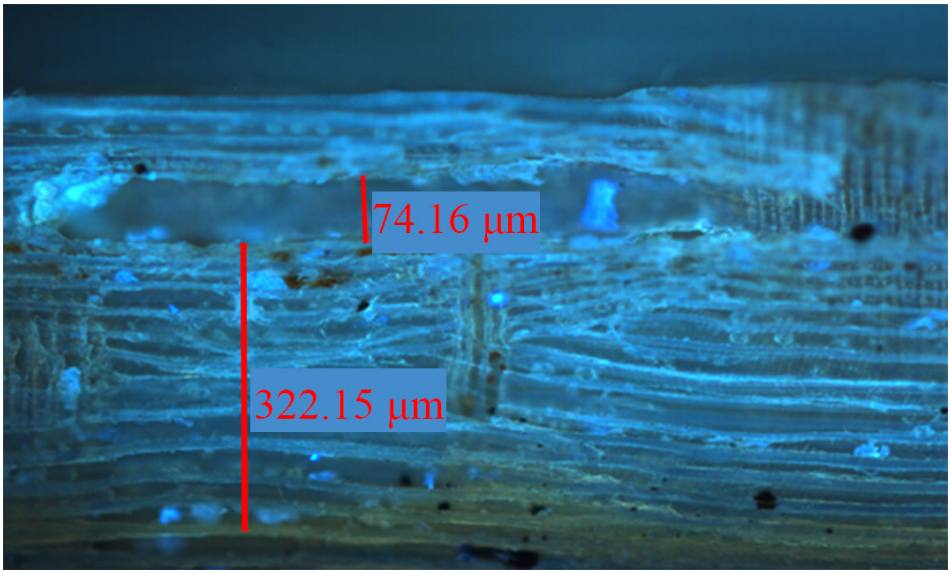

Figure 25. Fluorescence micrograph of a resin canal (74 µm wide) on the side of a previously scanned micro-XCT sample; radial surface is shown with longitudinal direction oriented horizontally.

Nano-XCT specimens were glued to a metal pin (sewing needle), which fits the specimen holder at the 32ID beamline. Mounting of the nano-XCT specimens had to be done extremely carefully due to the small size of the sample, indexing of the original orientation, and precise vertical mount of the specimen to stay within the FOV of the 50 μm x 50 μm beamline. In addition, the specimen must be mounted properly before the JB Weld Quick-Setting Epoxy (Clear Weld, JB Weld Company, Sulphur Springs, TX, USA) begins to cure within the 5 minute cure time frame. The sectioned specimens were handled under a microscope. The specimen (40 μm x 40 μm x 200 μm) was laid flat on a glass microscope slide. The tip of the sewing needle was dipped into the epoxy mixture so that just a drop of epoxy was on the end of the needle. The needle was held upside down for roughly 3 minutes so that the epoxy could partially cure. Otherwise, the epoxy droplet encompasses the entire specimen. Holding the needle with fine forceps that are closed when no pressure is applied to the sides, the needle was moved to just come in contact with the end of the specimen (previously noted orientation from the micro-XCT master sample) and mounted it to the end of the needle, seen in Figure 26.

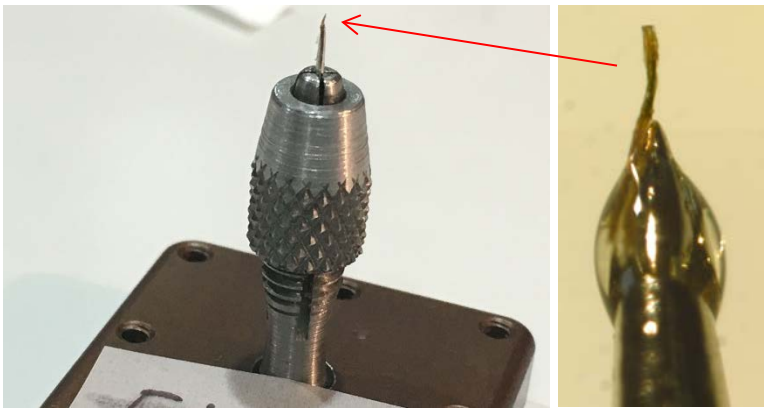

Figure 26. Nano-XCT specimen held in micro chuck on the left; sample mounted on top of a needle with epoxy on the right.

Vertical alignment adjustments were made under the microscope before the epoxy fully cured. The forceps held the needle, with the nano XCT sample on the tip, upside down for another five minutes, until the epoxy fully cured. The mounted sample was placed in a small, cylindrical container and held steady by being stuck in a small piece of Styrofoam (Figure 27). The container and lid were both labeled with the master XCT sample identifier, location identifier, and any extra treatment, discussed next.

Figure 27. Mounted nano-XCT sample fixed in container with Styrofoam (arrow indicates nano XCT sample on top of needle).

It was observed that in the micro-XCT datasets, the CML had a greater X-ray attenuation value than the rest of the cell wall, even in areas far away from the bondline where there is not adhesive present (Figure 28). Since the CML is rich in lignin and also has a higher attenuation value than the rest of the cell substance, the author decided that

delignification of the cell wall might provide better contrast between cell substance and adhesive for the nano-XCT scans.

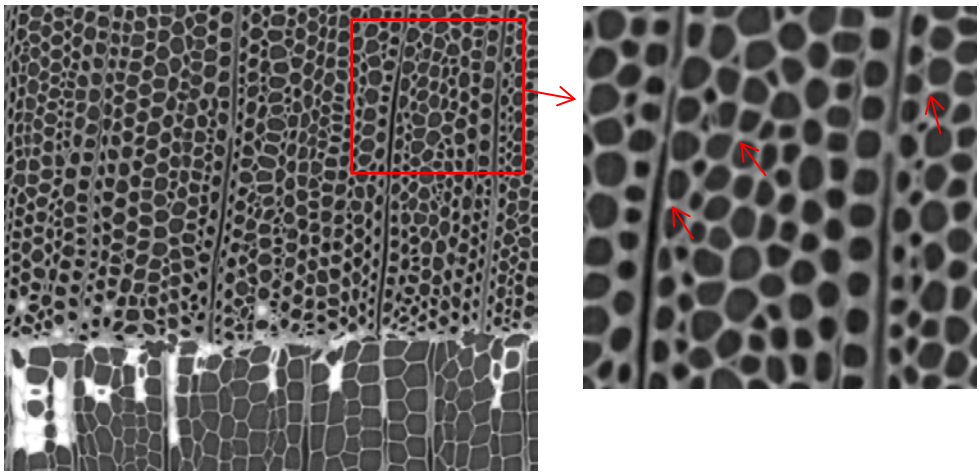

Figure 28. Micro-XCT slice (red arrows show examples of higher attenuation in CML).

A paracetic acid (PAA) treatment consisting of 32 weight % in dilute acetic acid was used to delignify the samples (Sigma-Aldrich, St. Louis, MO, USA). This type of treatment has been successfully used to delignify cellulosic biomass samples in previous research (Kumar et al., 2013). The specimens were placed in glass vials and filled with PAA using a glass dropper. They were placed in a fume hood at room temperature for 9 hours and more PAA was added every 3 hours to replace what had evaporated. At the end of the treatment, the specimens were carefully removed using forceps and placed on a glass plate where they were dehydrated in acetone. Some of the samples were also stained using potassium permanganate ($KMnO_4$) stain (UN 1490, EMD Chemicals, Gibbstown, NJ, USA). The large metal ions from the stain should penetrate the remaining hemicellulose structure, after the cell structure is opened up from the delignification treatment. This staining procedure was based on previous work conducted on staining

cellulose microfibrils (Xu et al., 2007), and was hoped would provide some definition to the cell wall layers in the resulting tomograph.

SEM and fluorescence microscopy were used to determine delignification of the CML. Cross-sections of the PAA treated samples were viewed using SEM (Figure 29). The PAA treated samples and the untreated samples were compared by visually evaluating the difference in CML intact from the SEM. SEM was found to be more effective than the fluorescence microscope due to the larger FOV and greater magnification. It was determined that some of the CML had been removed, but that the sample was still intact enough to be sectioned for the nano-XCT samples.

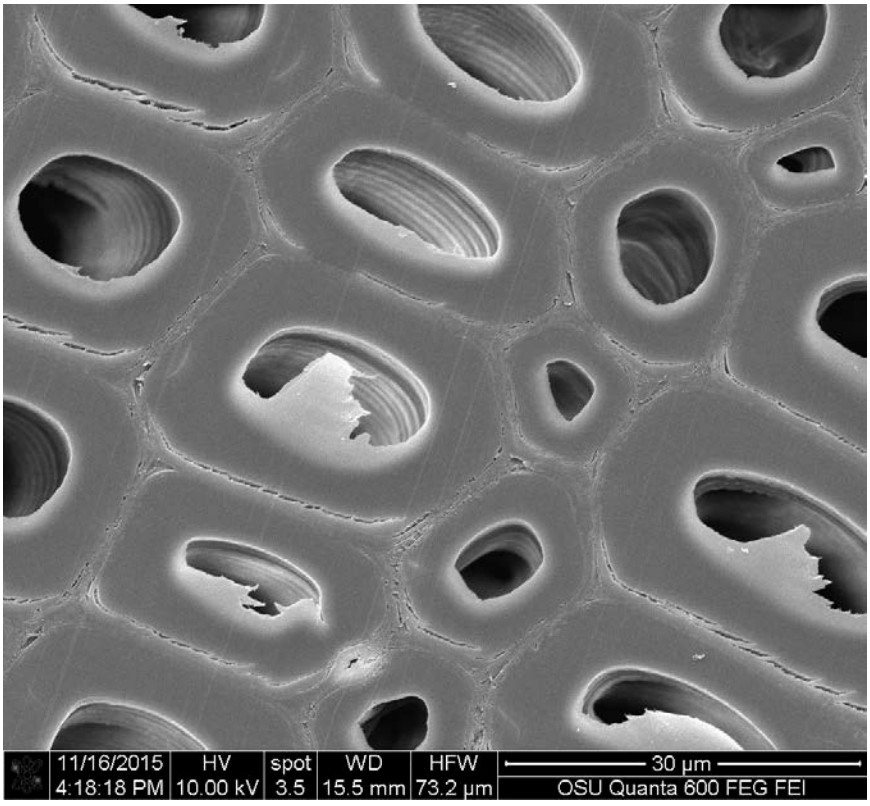

Figure 29. SEM cross-section of Douglas-fir wood cells after PAA treatment.

The nano-XCT samples were cut from the PAA treated micro-XCT dimension samples in the same manner as previously described and mounted on the needle. These samples were much more fragile after the treatment and more difficult to track from the original micro-XCT sample, due to the increase in handling. The samples that had been stained with the potassium permanganate could not be tracked to the original sample and often the dark IPF could not be visually distinguished from the stained wood cells.

The nano-XCT samples were transported to the APS, where the sample containers were opened and the samples were allowed to equilibrate to the laboratory conditions overnight. During XCT scanning, movement of a fraction of a micron resulted in blurred tomograms. Movement could occur due to moisture content change or sample degradation due to radiation exposure. The first few specimens scanned all experienced some motion during the scan. Consequently, a “pre-cooking” procedure was developed. The specimens were exposed to the beam and rotated for roughly 20 minutes before capturing the XCT data. This “pre-cook” was an attempt to deform/degrade the sample before capturing the data. After about 20 minutes, the visible sample movement was minimal, and scanning began.

The nano-XCT scans were performed at a beam energy of 8 KeV, with a 500 ms exposure time. A total of 361 projections were collected through 180 degrees of rotation and the total scan time was 10 minutes. Only 361 projections were selected in an effort to reduce the scan time and minimize movement of the sample. These scan parameters resulted in a resolution of 60 nm^3/voxel. A list of captured nano-XCT datasets are listed in Table 6.

Table 6. Nano-XCT collected datasets.

Master micro-XCT sample	Nano-XCT scans	PAA treatment	PAA treatment and stain
EE-IPL-1	2	-	-
EE-IPL-2	2	2	-
EE-IPL-3	7	-	-
EL-IPH-4	3	2	-
EL-IPH-6	5	-	-
EL-IMDI-5	2	2	3
DF tracheid	2	-	-
TOTAL	23	6	3

The nano-XCT datasets were matched to the micro-XCT sample in FIJI (Schindelin et al., 2012) using the 3D Analyzer plug-in and the orthogonal view tools. Using detailed notes taken when sectioning the nano-XCT samples, certain anatomical features were used to match the location of the nano-XCT sample within the micro-XCT dataset.

Adhesive penetration calculations were conducted in FIJI using a box analysis technique on the 32-bit images. The author identified a location within the cross-section of the nano-XCT sample that contained a lumen filled with adhesive and an adjacent cell wall that was free from any obvious scanning artifacts. The sample was rotated to create a line that was perpendicular to the AOI. A box was drawn that was five pixels in height, and the grayscale values were measured within that box. A box was used in attempt to smooth out any noise within the dataset, since the resulting grayscale value is an average of the height of the box at a given x coordinate. This procedure was conducted on three of the best quality datasets.

3.2.7 Energy Dispersive Spectroscopy

Scanning Electron Microscopy (SEM) and Energy Dispersive Spectroscopy (EDS) were conducted at the Oregon State University Electron Microscopy Laboratory on a FEI QUANTA 600F environmental SEM. EDS was used to determine if areas that contained adhesive also contained iodine, due to the issues with the IMDI during the micro-XCT scanning. Paris (2014) had previously verified that the iodine remained covalently bonded to the PF polymer. Therefore, detection of iodine confirmed the presence of PF. Samples of each adhesive type were carefully prepared using the ultra-microtome (Leica UM UC7, Vienna, Austria). In addition, some samples were embedded using a Spurr Low Viscosity EpoFix embedding kit (Ted Pella, Redding, CA, USA). In addition to confirming that iodine was present where adhesive was present, the author attempted to detect adhesive penetration into the cell substance using EDS. Therefore, a clean surface was created to distinguish cell wall and lumen edges. Without the embedding medium, the EW cells collapse or tear out, making it hard to distinguish the CML from other layers, and the lumen. The specimens were embedded and the cross-section surface was cleaned on the ultra-microtome with a diamond knife.

Before EDS analysis, the surface of the specimen was coated with a gold/palladium sputter coating for 35 seconds. Some of the samples had an additional osmium soak, also in an attempt to prevent charging of the poorly conductive wood sample. This step was skipped on later specimens because the fragile sample was altered during the osmium soak and drying process. Samples were placed on small stubs and secured with a carbon tape before being placed in the SEM chamber. A high vacuum and voltage of 8-10 kV with a spot size of 4.5-6 µm was used for scanning. A voltage of 8 kV

is required to excite the iodine element (Z=53). The resolution of the image was 0.111 µm/pixel. Line scans were then performed to trace the presence of iodine across a double cell wall where adhesive was known to be present in an adjacent lumen.

3.2.8 X-ray Fluorescence Microscopy

X-ray Fluorescence Microscopy (XFM) was performed by Joseph Jakes (US Forest Products Laboratory, Madison, WI) at the APS on 2ID-E beamline. This was a complementary method to confirm the presence of adhesive in the cell wall for the IMDI samples, since there was a lack of contrast in the adhesive during micro-XCT scanning. A description of the XFM technique was reported by Jakes et al. (2015).

IMDI and IPH samples that were previously scanned with micro-XCT were sent to Jakes, who prepared 2 µm thick cross-sections for transmission XFM that included areas with adhesive near the bondline. XFM elemental maps of iodine were captured and calibrated to determine iodine concentration. The resolution of the IMDI samples was 0.2 μm^2/pixel and the IPH was 0.3 μm^2/pixel.

CHAPTER 4: RESULTS AND DISCUSSION

4.1 Lap-shear Tests

4.1.1 Results Summary

A total of 75 lap-shear tests were analyzed, across all four adhesive types, out of which 39 were control samples and 36 were tested after weathering. The average failure load for non-weathered samples (all adhesives combined) was 924 N (46% COV) while that for weathered was 824 N (50% COV). The difference in weathering for failure load was not statistically significant. There were two methods of measuring the displacement, an extensometer clip gauge, and the DIC technique. Both were compared for the full analysis, reported in the following sections. This section summary only reports the DIC results, for simplicity.

A typical shear stress vs. shear strain curve from the DIC technique is shown in Figure 30. The average effective shear modulus for non-weathered samples (all adhesive combined) was 13,159 MPa (63% COV) while that for weathered was 11,787 MPa (65% COV). The difference in weathering for effective shear modulus was statistically significant for the IPH samples (p-value = 0.013). During the lap-shear test, 38 samples did not fail within the notches. The average energy to failure for only those samples that failed within the notches, non-weathered samples (all adhesives combined) was 0.008 J (88% COV) while that for weathered was 0.046 J (173% COV). The high variability observed in these measurements is due to the grouping of multiple adhesive types and different bonded wood surfaces. The difference in weathering for energy to failure was not statistically significant for either sample group. The lack of statistically significant

difference in weathering between the IPL and IPLFE adhesive systems indicated that these two systems performed similarly after weathering as they did before.

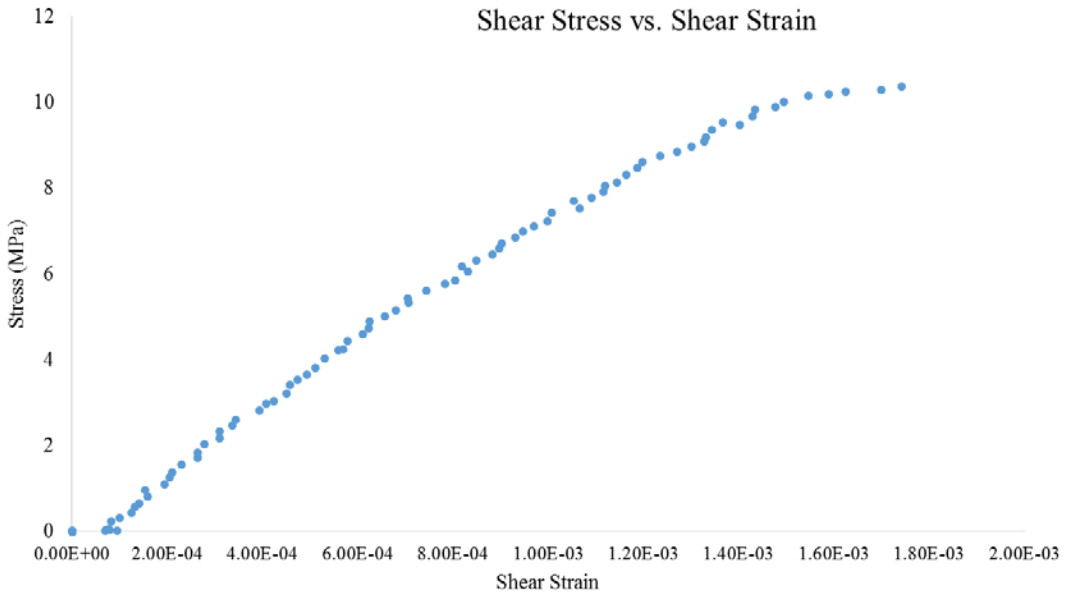

Figure 30. Shear stress vs. shear strain from DIC of sample EL-IPL-18.

Table 7 is an overview of the average and COV for each measurement, with each specimen group, and the number of specimens that were weathered and non-weathered. The percent change after weathering is also listed, with a negative percent change meaning that the sample average increased after weathering exposure. Additional tables are listed later for the energy to failure statistics for only those that failed between the notches, percent wood failure, and a comparison of the clip gauge results to the DIC results.

Table 7. Summary results for DIC lap-shear test results; mean values shown with COV in parentheses.

Specimen Group	Non-weathered				Weathered				Percent Change After Weathering		
	n	Failure Load (N)	Effective Shear Modulus (MPa)	Energy to Failure (J)	n	Failure Load (N)	Effective Shear Modulus (MPa)	Energy to Failure (J)	Failure Load	Effective Shear Modulus	Energy to Failure
EE-IPL (n=10)	5	415 (16%)	4,488 (42%)	0.003009 (20%)	5	403 (48%)	4,520 (57%)	0.003034 (56%)	2.9 %	-0.7 %	-0.8 %
LL-IPL (n=10)	5	1325 (36%)	26,005 (47%)	0.012384 (41%)	5	1321 (21%)	32,055 (74%)	0.011227 (90%)	0.3 %	-23.3 %	9.3 %
EL-IPL (n=7)	6	1050 (39%)	10,455 (47%)	0.010673 (61%)	1	1208*	11,355*	0.004734*	-15.0 %	-8.6 %	55.6 %
EE-IPH (n=9)	5	362 (31%)	4,265 (46%)	0.00218 (73%)	4	486 (46%)	4,866 (82%)	0.009329 (51%)	-34.3 %	-14.1 %	-327.9 %
LL-IPH (n=10)	5	1631 (23%)	9,797 (30%)	0.031144 (46%)	5	1381 (53%)	13,715 (58%)	0.161739 (211%)	15.3 %	-40.0 %	-419.3 %
EL-IPH (n=9)	3	955 (22%)	18,894 (59%)	0.005273 (96%)	6	586 (79%)	8,756 (115%)	0.013372 (104%)	38.6 %	53.7 %	-153.6 %
EL-IMDI (n=8)	4	480 (60%)	8,590 (9%)	0.003287 (140%)	4	855 (42%)	20,160 (59%)	0.00619 (118%)	-78.1 %	-134.7 %	-88.3 %
LL-IMDI (n=4)	3	1063 (2%)	25,304 (72%)	0.003695 (32%)	1	259*	2,835*	0.000436*	75.6 %	88.8 %	88.2 %
EL-IPLFE (n=8)	3	1039 (56%)	10,637 (15%)	0.019705 (132%)	5	925 (29%)	7,823 (16%)	0.021931 (65%)	11.0 %	26.5 %	-11.3 %

Furthermore, weathering caused five samples to delaminate. These samples were added to a separate statistical analysis. They were entered as a value of 1 for the effective modulus measurement and a value of 10^{-05} for the energy to failure measurement. The difference in weathering on effective shear modulus was statistically significant for the EL and EL-IMDI samples, when including the delaminated samples (p-value = 0.015, p-value = 0.075 , respectively). Typically, the percent wood failure was greater in the weathered samples than in the non-weathered, with the exception of the LL-IMDI samples, which had three weathered samples completely delaminate. Few of the LL specimens failed within the notches, as the test is designed. These samples also had a higher overall failure load than the EE and EL specimens. No clear correlation could be made between the failure mode and the percent wood failure. The DIC surface shear strain maps showed the IPH and IMDI samples had a greater amount of shear strain near the bonded interphase at the same loads as the IPL and IPLFE samples, with the same bonded wood surface. When comparing the IPL and IPH weathered samples, there was more shear strain in the IPH samples than in the IPL samples, which also correlated to an overall lower stiffness in the IPH groups.

4.1.2 Specimen Variability

Preliminary analysis of the results revealed some inconsistent behavior, which required reexamination of the specimens for possible causes. The DIC measurement technique for this application is sensitive to fine detail on the observed surface. Although care was taken to prepare surfaces for bonding with well-defined EW and LW, and to create surfaces that were perfectly aligned with the longitudinal-tangential plane, some deviations still existed. To identify misaligned specimens, the fluorescence bondline

images were evaluated to ensure that the bonded surfaces matched the label of the specimen. After evaluation of the fluorescence reference images, as well as investigating the opposite side of the bondline with a light microscope, ten of the specimens were changed to an updated label with the correct bonded wood surfaces. Nine of the specimens were found to have a mixture in bonded wood surface throughout the sample (i.e. half of the bond appeared to be EW bonded to LW but throughout the bonded area it changed to EW bonded to EW). The samples that exhibited this transition from EW to LW at the bondline are listed in Table 8. These specimens retained their original labels, based on the bonding procedure.

Table 8. Specimens that exhibited a transition between EW and LW at the bonded surface.

Original Specimen Label	**Bonded Surface**		**Quantity**
	Side 1	Side 2	
LL-IPL	LL	EL	3
EL-IPL	EL	EE	2
EE-IPH	EE	EL	1
LL-IPH	LL	EL	1
EL-IPH	EL	EE	1
EL-IMDI	EL	EE	1

Some of the specimens also had an EW/LW transition region within the AOI of the DIC analysis (Figure 31). This transition region lead to higher amount of strain and noise in the results. In addition, an EW/LW transition region outside the AOI can also cause variability (Figure 32). The variability of the sample morphology contributed to the variability in the statistical analysis.

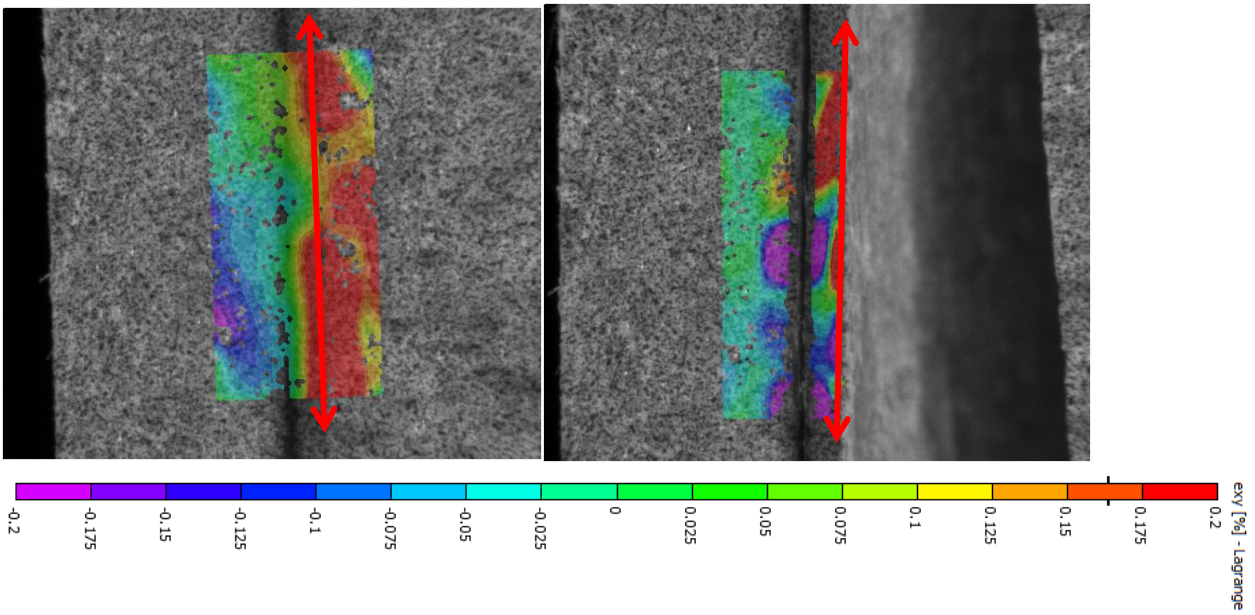

Figure 31. Sample EL-IPL-7 with EW/LW transition region within the AOI; high shear strain can be seen around the red arrow in the left image at the max load (2011 N); the specimen immediately after failure is shown in the right image.

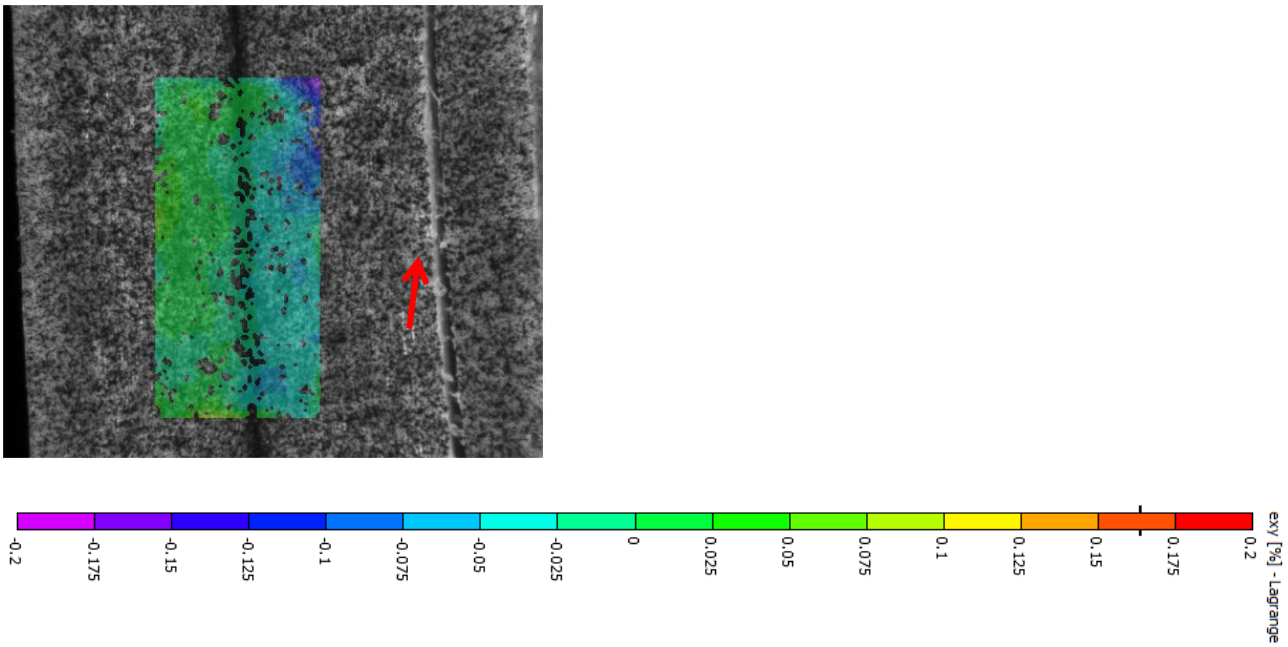

Figure 32. Sample EE-IPL-5 after failure; EW/LW failure (red arrow) in FOV, but not within the AOI.

Some of the specimens were produced inconsistently and had notches that were either cut too far past the bondline, or not cut far enough (> 0.1 mm). The 38 specimens that were produced incorrectly were removed from the statistical analysis. This left a sample size of 75 for the final statistical analysis.

4.1.3 Statistical Analysis

A statistical analysis was conducted in RStudio (ver. R 3.2.3) with a three-way Analysis of Variance (ANOVA) test and a Least Squares Means (LSM) test (RStudio, 2015) to determine differences in weathering. An α-priori of 0.10 was used to report significant differences. Based on the residual plots and to justify the assumptions of the ANOVA and LSM tests, the data was log-transformed. The main objective was to detect significant differences in weathering vs. non-weathering for adhesive types. Table 9 represents each unique sample variation and the number of specimens that were weathered and non-weathered. Any changes in sample sizes for an analysis are listed in respective sections. The following sections report the statistical results for the failure load, effective shear modulus, and energy to failure. Additionally, statistics including the delaminated samples are listed in a later section.

Table 9. Replications used for the full statistical analysis, including specimens that failed outside of the notches and excluding the delaminated samples; w = weathered and nw = non-weathered.

adhesive / wood	IPL		IPH		IMDI		IPLFE	
	w	nw	w	nw	w	nw	w	nw
EE	5	5	4	5	-	-	-	-
LL	5	5	5	5	1	3		-
EL	1	6	6	3	4	4	5	3

4.1.3.1 Failure Load

The average failure load of non-weathered samples (all adhesive combined) was 924 N (46% COV) while weathered was 824 N (50% COV). The average and COV for the failure load for each sample are listed in Table 10 and shown in Figure 33. The failure load was defined as 80% of the maximum load, post-peak. The EE-IPH, EL-IPL, and EL-IMDI sample groups had an increase in average failure load after weathering.

Table 10. Average and COV for failure load; *LL-IMDI and EL-IPL weathered only had one specimen.

Sample	non-weathered average (N) (COV)	weathered average (N) (COV)
EE-IPL (n=9)	415 (16%)	403 (48%)
LL-IPL (n=10)	1,325 (36%)	1,321 (21%)
EL-IPL (n=8)	1,050 (39%)	1,208*
EE-IPH (n=9)	362 (31%)	486 (46%)
LL-IPH (n=10)	1,631 (23%)	1,381 (53%)
EL-IPH (n=9)	955 (22%)	586 (79%)
EL-IMDI (n=8)	480 (60%)	855 (42%)
LL-IMDI (n=4)	1,063 (2%)	259*
EL-IPLFE (n=8)	1,039 (56%)	925 (29%)

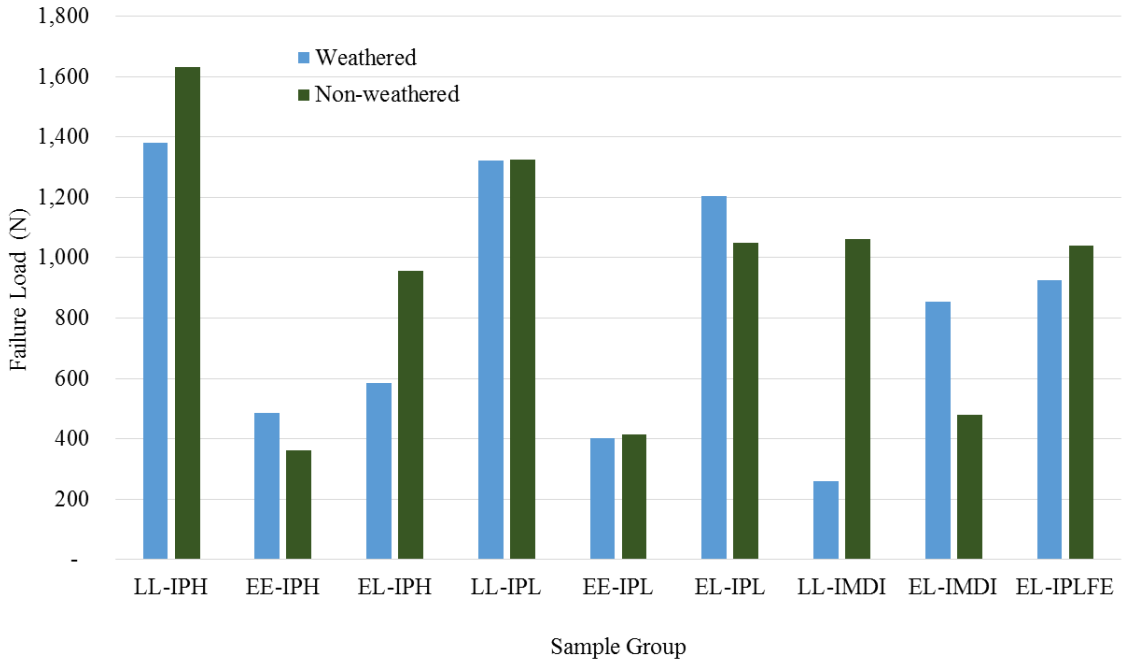

Figure 33. Average failure load for each sample group, separated by weathered and non-weathered samples.

Table 11 shows the results of the three-way ANOVA test for the failure load. The LSM test evaluated the effects of weathering on bonded wood surface and on adhesive type (Table 12 - Table 13). The three-way ANOVA results show that bonded surface and adhesive alone have significant effects on failure load, as well as the three-way interaction between bonded surface, adhesive, and weathering. However, there was no significant difference in the failure loads after weathering, for any of the interactions.

Table 11. Three-way ANOVA for the failure load statistics; ** denotes p-values that are significant.

Interactions	Failure Load (n=75)
Bonded surface	0.00000024**
Adhesive	0.058**
Weathering	0.447
Bonded surface : adhesive	0.379
Adhesive : weathering	0.676
Bonded surface : weathering	0.287
Bonded surface : adhesive : weathering	0.046**

Table 12. Effect of weathering on wood surface for the failure load.

Effect of weathering on wood surface	Failure Load (n=54)
EE	0.960
EL	0.187
LL	0.249

Table 13. Effect of weathering on adhesive for the failure load.

Effect of weathering on adhesive	Failure Load (n=30)
IMDI	0.161
IPH	0.167
IPL	0.104
IPLFE	0.825

4.1.3.2 Effective Shear Modulus

The average effective shear modulus for non-weathered samples (all adhesive combined) was 13,159 MPa (63% COV) while that for weathered was 11,787 MPa (65% COV), calculated from the DIC output. The average effective shear modulus generated from the DIC data is listed in Table 14 and shown in Figure 34. The effective shear modulus was calculated from the stress vs. shear strain data. The average effective shear modulus generated from the clip gauge extensometer data is listed in Table 15 and shown in Figure 35. The effective shear modulus from the clip gauge was calculated from the

stress vs. clip displacement data. The effective shear modulus was defined as the slope of the linear region of the curve. The two methods resulted in different measurements for the effective shear modulus, and in some cases, opposite trends in differences in values before and after weathering.

Table 14. Average and COV for effective shear modulus from the DIC output; *LL-IMDI and EL-IPL weathered groups only had one specimen.

DIC Sample	non-weathered average (MPa) (COV)	weathered average (MPa) (COV)
EE-IPL (n=10)	4,488 (42%)	4,520 (57%)
LL-IPL (n=10)	26,005 (47%)	32,055 (74%)
EL-IPL (n=7)	10,455 (47%)	11,355*
EE-IPH (n=9)	4,265 (46%)	4,866 (82%)
LL-IPH (n=10)	9,797 (30%)	13,715 (58%)
EL-IPH (n=9)	18,894 (59%)	8,756 (115%)
EL-IMDI (n=8)	8,590 (9%)	20,160 (59%)
LL-IMDI (n=4)	25,304 (72%)	2,835*
EL-IPLFE (n=8)	10,637 (15%)	7,823 (16%)

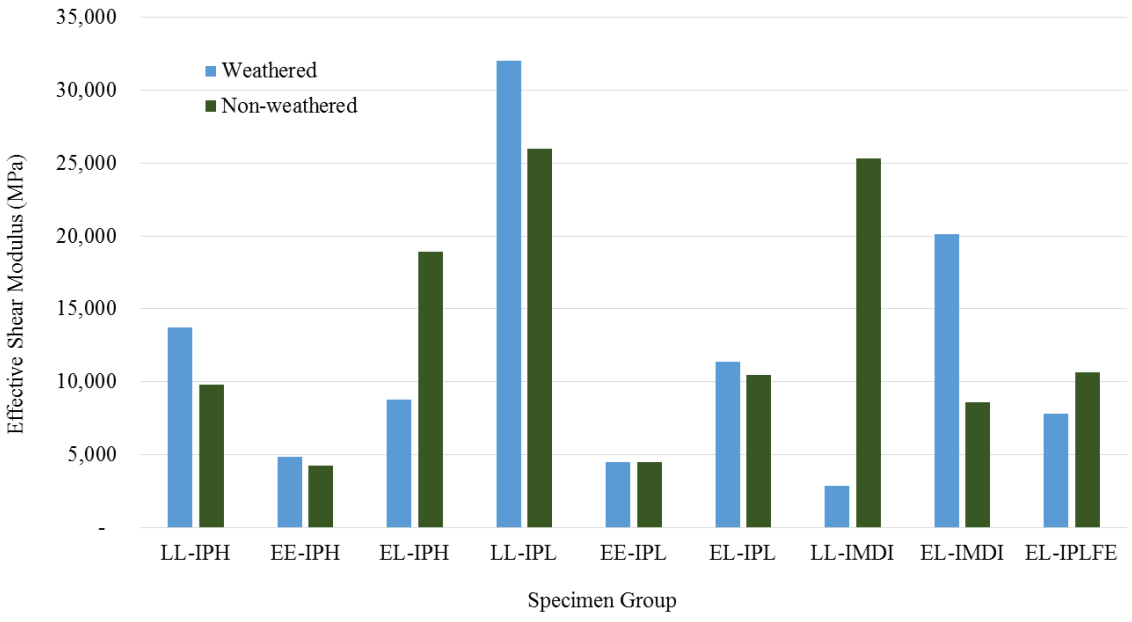

Figure 34. Average effective shear modulus for each sample group from DIC, with error bars, and separated by weathered and non-weathered samples.

Table 15. Average and COV for effective shear modulus from the clip gauge; *LL-IMDI and EL-IPL weathered groups only had one specimen.

Clip Sample	non-weathered average (MPa) (COV)	weathered average (MPa) (COV)
EE-IPL (n=9)	6,497 (26%)	5,625 (69%)
LL-IPL (n=10)	9,680 (22%)	8,482 (19%)
EL-IPL (n=8)	9,727 (26%)	14,461*
EE-IPH (n=9)	5,330 (58%)	6,044 (16%)
LL-IPH (n=10)	17,536 (38%)	10,671 (49%)
EL-IPH (n=9)	11,204 (53%)	4,688 (63%)
EL-IMDI (n=8)	5,643 (64%)	7,889 (53%)
LL-IMDI (n=4)	10,489 (34%)	6,112*
EL-IPLFE (n=8)	9,012 (48%)	9,744 (42%)

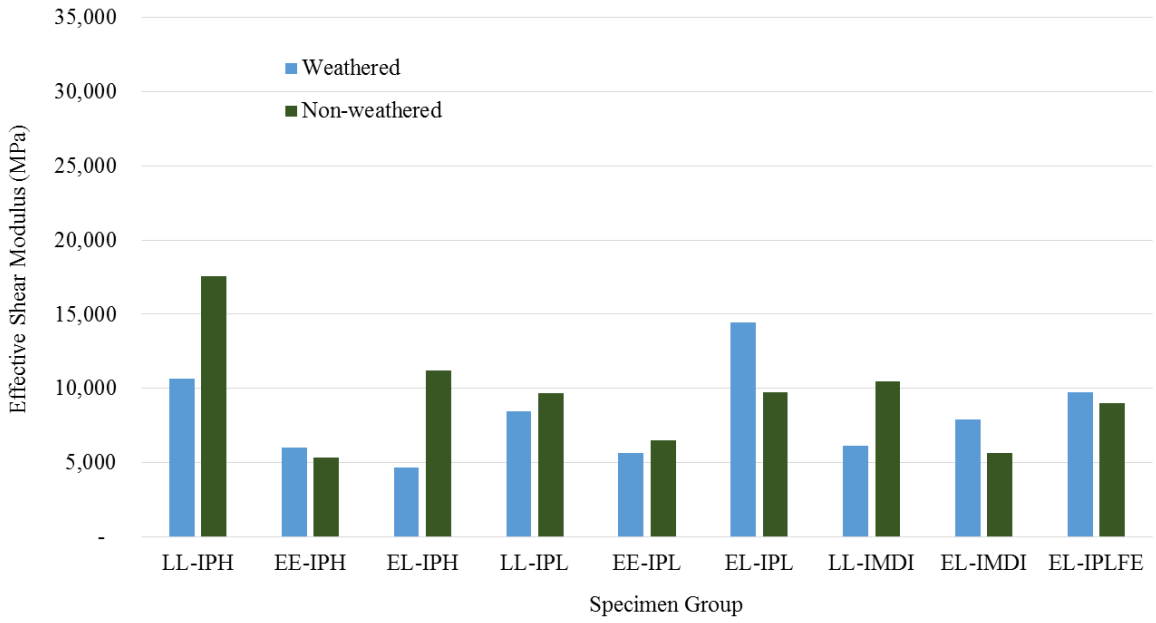

Figure 35. Average failure load for each sample group from the clip gauge, separated by weathered and non-weathered samples.

Table 16 shows the results of the three-way ANOVA test, for both the DIC and the clip gauge effective shear modulus. The LSM test evaluated the effects of weathering on bonded wood surface and on adhesive type (Table 17 - Table 18). The effective shear modulus for the EL non-weathered specimens was twice as great than the EL weathered

specimens, from the clip gauge data (Table 17). The effective shear modulus was 3 times greater for the non-weathered specimens, than the weathered specimens for the IPH specimens, from both the DIC and clip gauge data (Table 18).

The EL samples were less stable after weathering, due to the uneven shrinkage and swelling rate of the EW cells vs. LW cells. The brittleness of the IPH may not create the flexibility needed to withstand weathering exposure. The IPL might be resulting in a more even rate of shrinkage and swelling, potentially due to penetration of the adhesive into the cell wall, and stabilization of the interphase region.

Table 16. Three-way ANOVA results; ** denotes p-values that are significant.

Interactions	Effective Shear Modulus DIC (n=75)	Effective Shear Modulus Clip Gauge (n=75)
Bonded surface	.000000323**	0.001**
Adhesive	0.116	0.505
Weathering	0.614	0.215
Bonded surface : adhesive	0.018**	0.057**
Adhesive : weathering	0.833	0.679
Bonded surface : weathering	0.972	.625
Bonded surface : adhesive : weathering	0.016**	.086**

Table 17. Effect of weathering on wood surface from the effective shear modulus; ** denotes p-values are significant; numbers listed in bold and italicized represent the magnitude that the non-weathered specimens are greater than the weathered specimens.

Effect of weathering on wood surface	Effective Shear Modulus DIC (n=54)	Effective Shear Modulus Clip Gauge (n=54)
EE	0.829	0.970
EL	0.121	0.043** ***(2.018)***
LL	0.829	0.422

Table 18. Effect of weathering on adhesive from the effective shear modulus; ** denotes p-values are significant; numbers listed in bold and italicized represent the magnitude that the non-weathered specimens are greater than the weathered specimens.

Effect of weathering on adhesive	Effective Shear Modulus DIC (n=30)	Effective Shear Modulus Clip Gauge (n=30)
IMDI	0.209	0.669
IPH	0.013** ***(2.841)***	0.033** ***(2.672)***
IPL	0.783	0.468
IPLFE	0.445	0.927

4.1.3.3 Energy to Failure

Some of the results from the DIC data (scattered between sample groups) exhibited a behavior unexpected for a wood sample in tension. In these samples, the stress vs. shear strain curve exhibited an increase in stiffness, seen clearly in Figure 36.

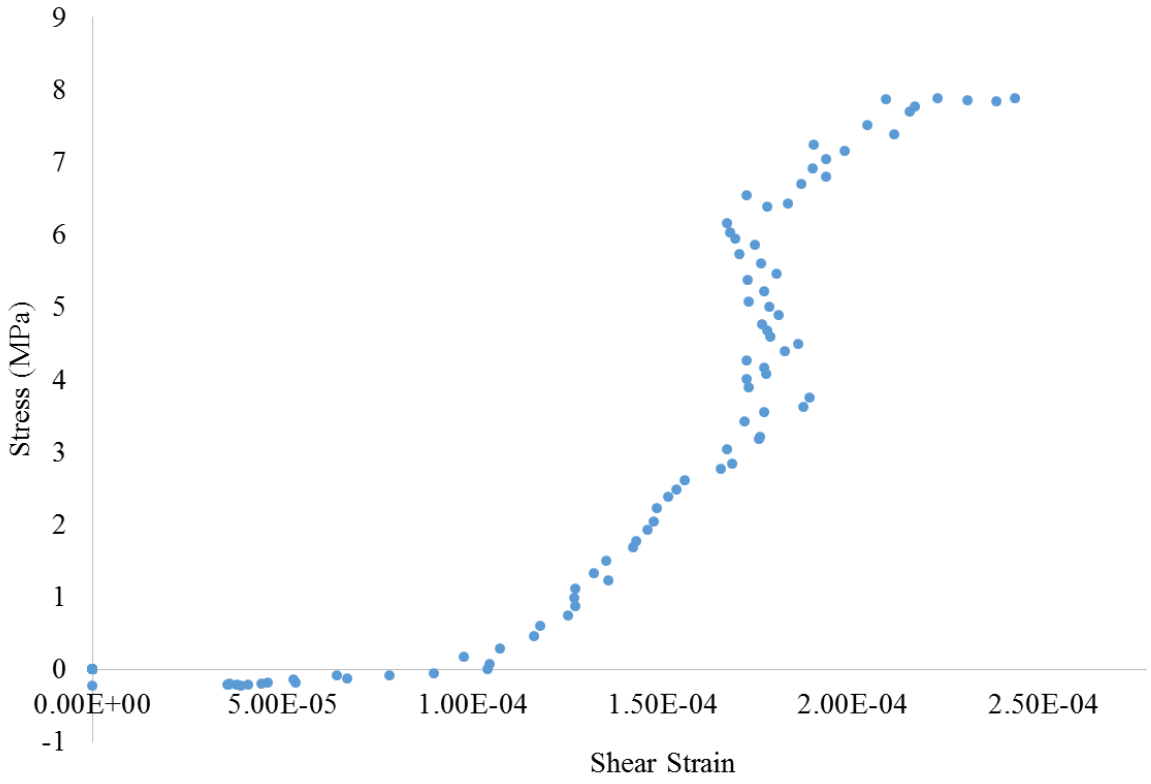

Figure 36. Example of stress vs. shear strain from DIC data; increase in slope is seen around 4 MPa.

After the removal of the specimens that were prepared incorrectly, there was only one remaining sample that exhibited the strange behavior in both the DIC and clip gauge data, seen in Figure 37 - Figure 38, which are results from the same sample. However, some of the DIC data remained with this unusual increase in stiffness behavior. Therefore, the proportional limit was not a consistent measurement and was not used as a measurement for comparison. The energy to failure was used since the failure load could be calculated consistently in all specimens. However, failure mode will be taken into consideration in a separate statistical analysis. The linear region used to define the effective shear modulus was kept at the previously defined linear region.

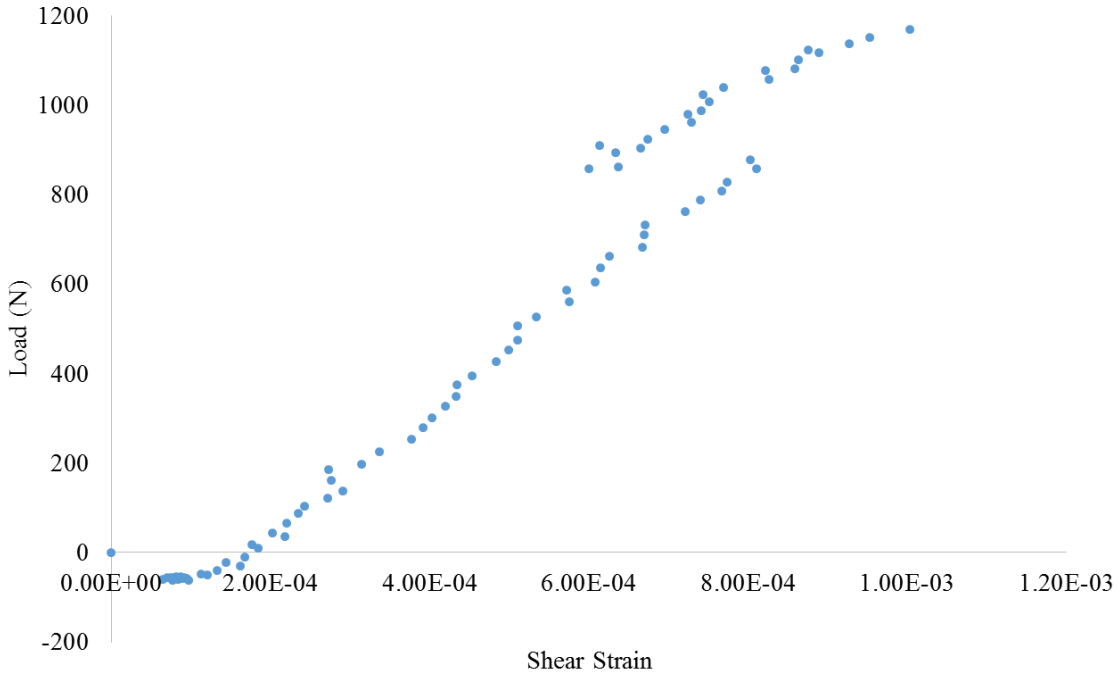

Figure 37. Load vs. shear strain from DIC for sample EL-IPH-10; behavior at 800 N is also seen in Figure 38.

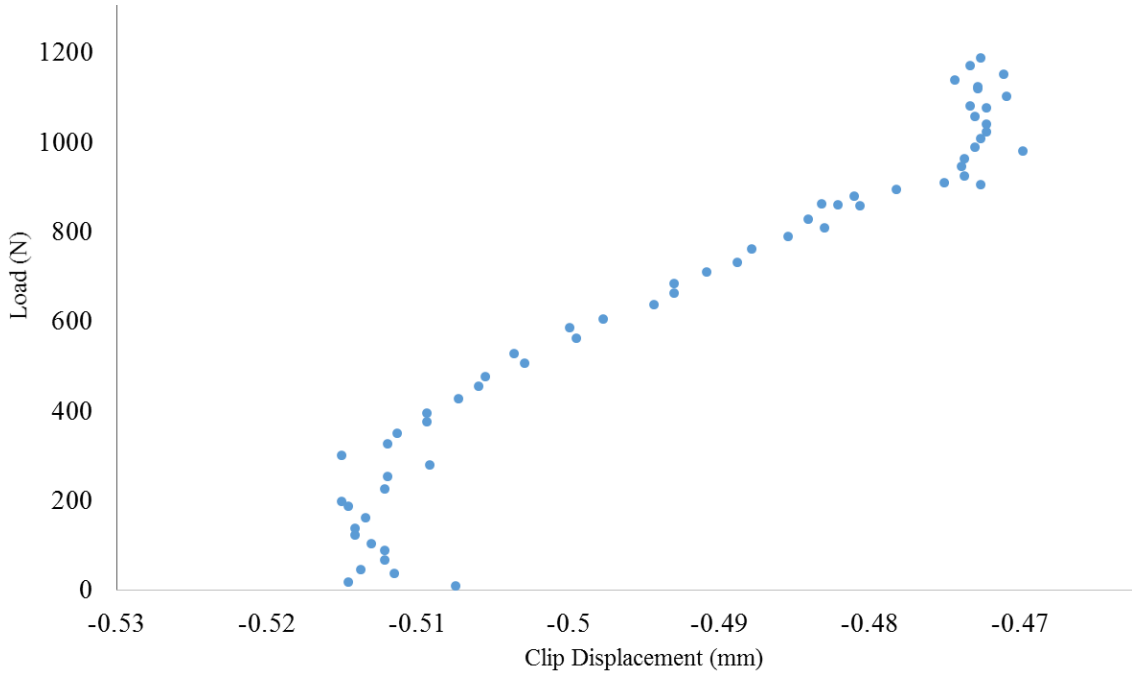

Figure 38. Load vs. clip gauge displacement for sample EL-IPH-10; behavior at 800 N shows an increase in stiffness

Potential causes of variability were further investigated. After examining the DIC shear strain maps, it was clear that any slack movement occurred early in the test, before the linear portion of the stress vs. shear strain curve. Therefore, this would not hinder the results. In addition, the DIC technique is inherently designed to account for any rigid, full sample movement, since the system was only tracking change in displacement over the imaged area. DIC assumes that the sample has a uniform amount of strain throughout the depth of the sample. If there was variation in the bonded surface, there could be deformation behavior present that is not captured by the DIC techniques. This observation could also be a consequence of the image capture rate.

Some of the lap-shear specimens deformed out of plane during the test. When this happens, the stress distribution changed in direction and magnitude. Some of the energy applied to the specimen was consumed to bend the specimen at the notches and less of

the energy was consumed by shear deformation. Therefore, when the specimen yielded in bending at the notches, little or no additional shear deformation was detected between the notches, causing further inconsistencies (Lu et al., 2013).

An additional verification experiment was conducted with Douglas-fir samples that represented half of the bonded lap-shear specimen (3 mm x 13 mm x 60 mm), with the same test setup as the lap-shear samples (Figure 39). A comparison was made using the DIC and clip gauge data to examine any discrepancies in the test setup. None of the abnormal behavior was observed, and the DIC and clip data had very similar behavior, seen in Figure 40 - Figure 41. This indicated that the test setup was not causing this increase in stiffness effect, but instead the sample morphology. Still, the effect of the carbon fiber and epoxy used to bond the carbon fiber to the specimen cannot be ignored, since the clip gauge rested on the edge of the carbon fiber tab (Figure 39). The samples that did exhibit this unusual behavior were mostly those that were manufactured incorrectly, with a notch either cut too far past the bondline, or not far enough.

Figure 39. Verification experiment setup to test slippage and abnormal behavior in DIC and clip gauge data.

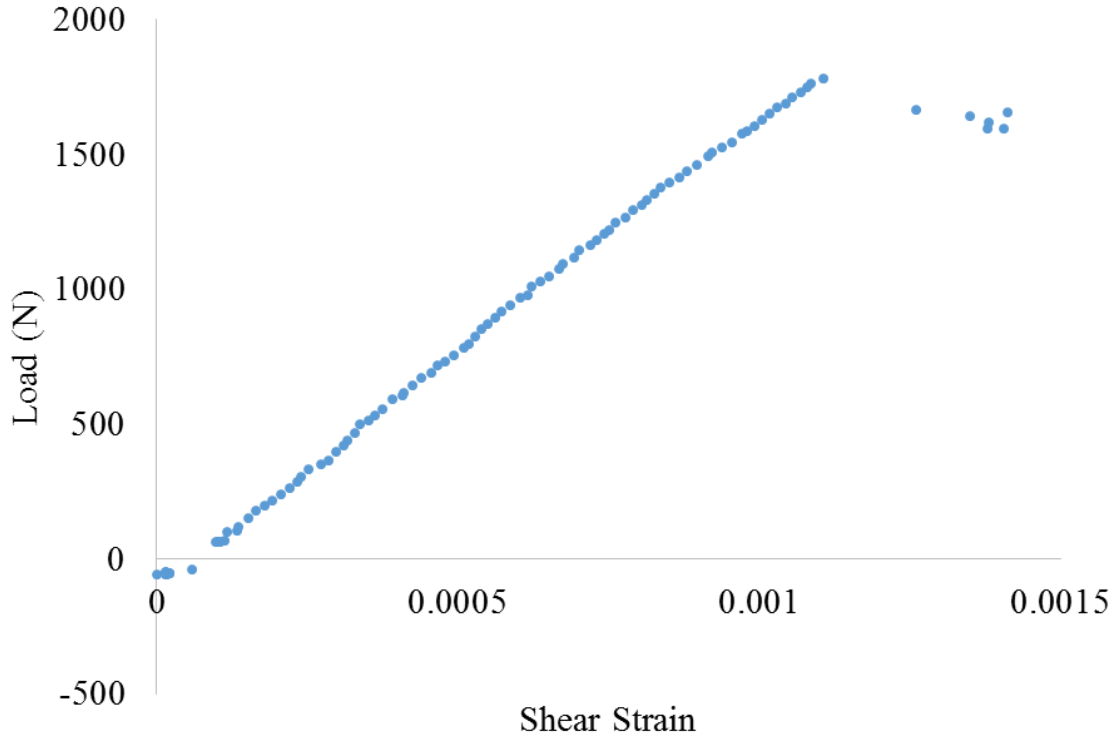

Figure 40. Load vs. DIC shear strain from verification experiment; the same sample is shown in Figure 41 with the clip gauge data.

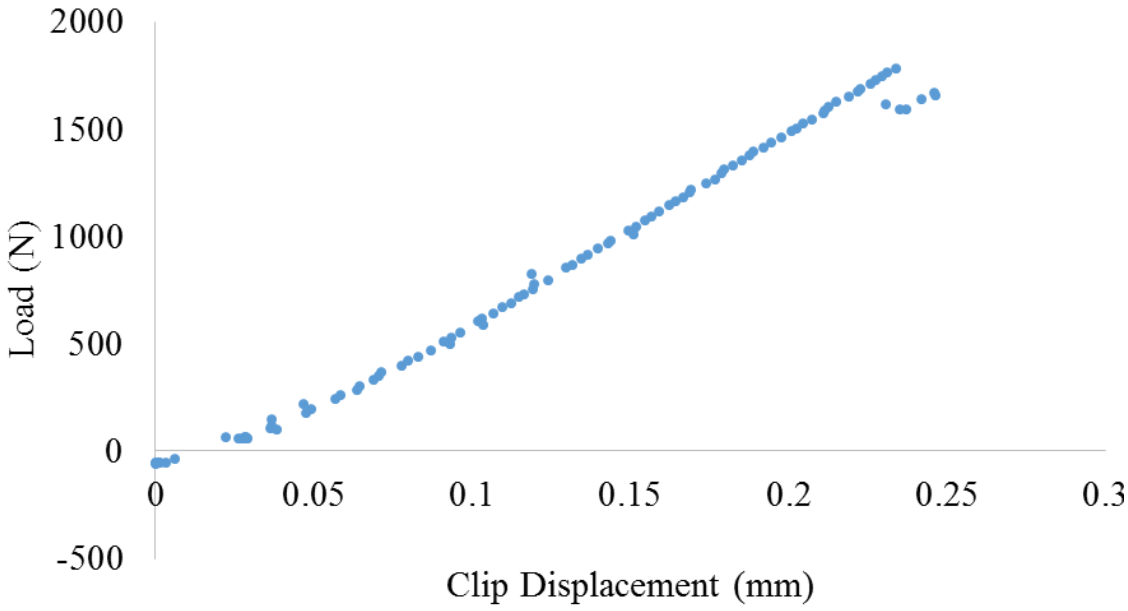

Figure 41. Load vs. clip gauge displacement from verification experiment; the same sample is shown in Figure 40.

The average energy to failure (all samples), for non-weathered samples (all adhesives combined) was 0.010 J (96% COV) while that for weathered was 0.026 J (199% COV), calculated from the DIC output. The average energy to failure generated from the DIC data is listed in Table 19 and graphically represented in Figure 42. The energy to failure was calculated from the load vs. shear strain data. The average energy to failure generated from the clip gauge extensometer data is listed in Table 20 and shown in Figure 43. The energy was calculated as the area under the curve, up to 80% of the maximum load, post peak.

Table 19. Average and COV for energy to failure from the DIC output; *LL-IMDI and EL-IPL weathered groups only had one specimen.

DIC Sample	non-weathered average (J) (COV)	weathered average (J) (COV)
EE-IPL (n=9)	0.003009 (20%)	0.003034 (56%)
LL-IPL (n=10)	0.012384 (41%)	0.011227 (90%)
EL-IPL (n=8)	0.010673 (61%)	0.004734*
EE-IPH (n=9)	0.00218 (73%)	0.009329 (51%)
LL-IPH (n=10)	0.031144 (46%)	0.161739 (211%)
EL-IPH (n=9)	0.005273 (96%)	0.013372 (104%)
EL-IMDI (n=8)	0.003287 (140%)	0.00619 (118%)
LL-IMDI (n=4)	0.003695 (32%)	0.000436*
EL-IPLFE (n=8)	0.019705 (132%)	0.021931 (65%)

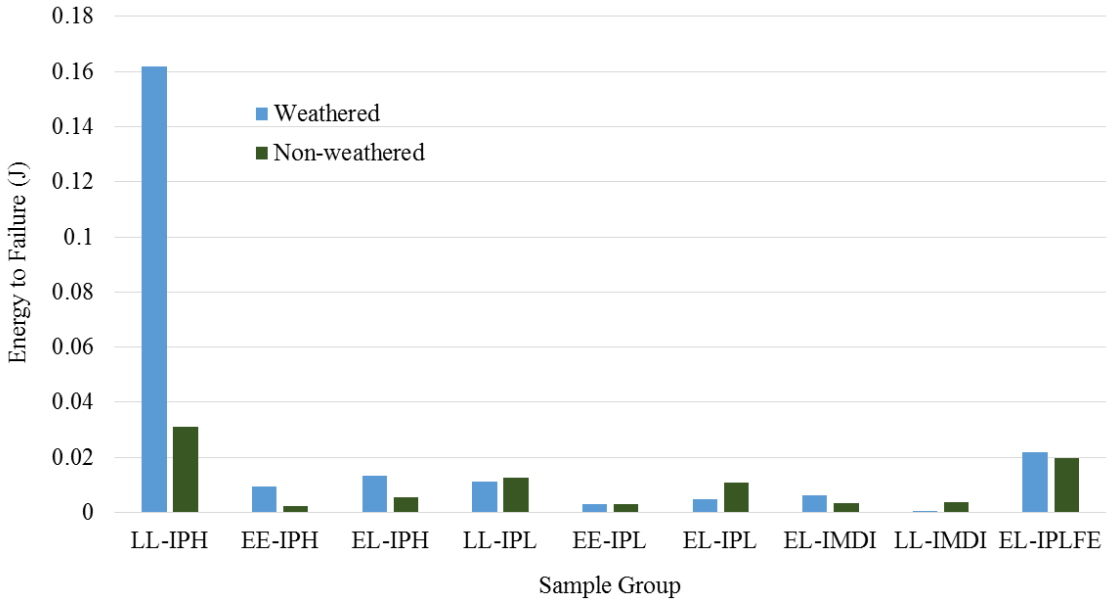

Figure 42. Average energy to failure for each sample group from DIC, with error bars and separated by weathered and non-weathered samples.

Table 20. Average and COV for energy to failure from the clip gauge; *LL-IMDI and EL-IPL weathered groups only had one specimen.

Clip Sample	weathered average (J) (COV)	non-weathered average (J) (COV)
EE-IPL (n=9)	76 (104%)	87 (66%)
LL-IPL (n=10)	927 (101%)	770 (62%)
EL-IPL (n=8)	554*	661 (107%)
EE-IPH (n=9)	220 (118%)	82 (71%)
LL-IPH (n=10)	904 (108%)	980 (56%)
EL-IPH (n=9)	282 (133%)	270 (59%)
EL-IMDI (n=8)	296 (42%)	206 (113%)
LL-IMDI (n=4)	18*	83 (83%)
EL-IPLFE (n=8)	359 (52%)	370 (51%)

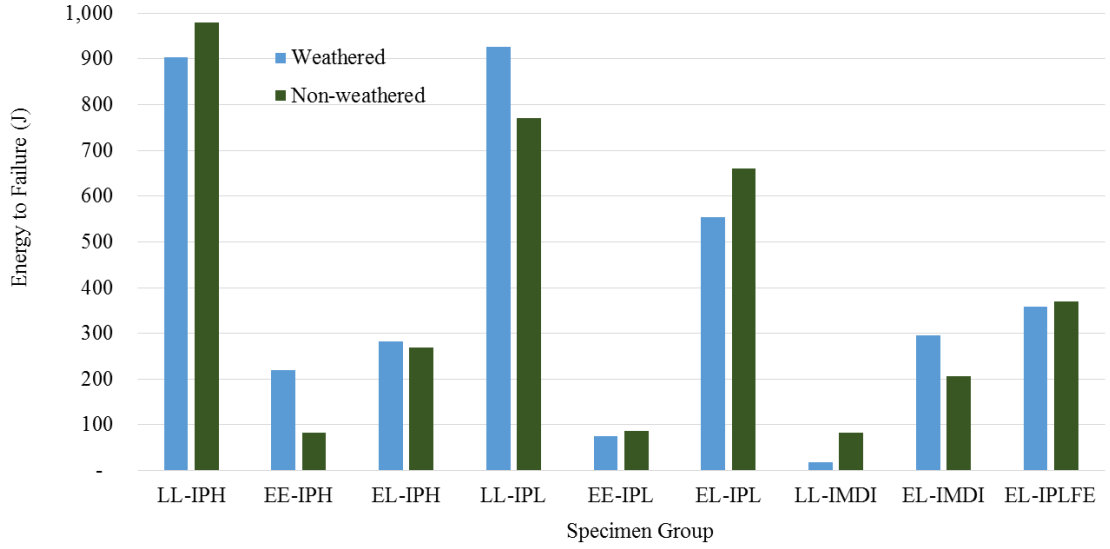

Figure 43. Average energy to failure for each sample group from the clip gauge, separated by weathered and non-weathered samples.

Table 21 shows the results of the three-way ANOVA test, for both the DIC and the clip gauge effective shear modulus. The LSM test evaluated the effects of weathering on bonded wood surface and on adhesive type (Table 22 - Table 23). There was no significant difference for the effect of weathering on wood surface, nor adhesive type. Table 24 lists only the samples that failed between the notches. The average energy to failure for only those samples that failed within the notches, non-weathered samples (all adhesives combined) was 0.008 J (88% COV) while that for weathered was 0.046 J (173% COV), calculated from the DIC output. Table 25 - Table 27 shows the same analysis for only samples that failed between the notches, and there was also no significant difference for the effect of weathering on wood surface, nor adhesive type. The energy measurement may not be the most effective way to identify differences in weathering.

Table 21. Three-way ANOVA from energy to failure measurement for all samples; ** denotes p-values that are significant.

Interactions	Energy to Failure DIC (n=75)	Energy to Failure Clip Gauge (n=75)
Bonded surface	0.003**	.0000749**
Adhesive	0.004**	0.129
Weathering	0.699	0.803
Bonded surface : adhesive	0.365	0.008**
Adhesive : weathering	0.653	0.983
Bonded surface : weathering	0.179	0.539
Bonded surface : adhesive : weathering	0.255	0.371

Table 22. Effect of weathering on wood surface for energy to failure (all samples).

Effect of weathering on wood surface	Energy to Failure DIC (n=54)	Energy to Failure Clip Gauge (n=54)
EE	0.324	0.949
EL	0.978	0.422
LL	0.394	0.729

Table 23. Effect of weathering on adhesive for energy to failure (all samples).

Effect of weathering on adhesive	Energy to Failure DIC (n=30)	Energy to Failure Clip Gauge (n=30)
IMDI	0.306	0.489
IPH	0.589	0.464
IPL	0.724	0.762
IPLFE	0.627	0.941

Table 24. Only samples that failed between the notches.

adhesive / wood	IPL		IPH		IMDI		IPLFE	
	w	nw	w	nw	w	nw	w	nw
EE	3	5	3	1	-	-	-	-
LL	0	2	3	0	1	0	-	-
EL	0	4	4	2	2	2	3	3

Table 25. Three-way ANOVA for energy to failure for only those samples that failed between the notches; three-way interaction not present due to lack of non-weathered specimens; ** denotes p-values that are significant.

Interactions	Energy to Failure DIC (n=37)	Energy to Failure Clip Gauge (n=37)
Bonded surface	0.057**	0.009**
Adhesive	0.015**	0.053**
Weathering	0.421	0.729
Bonded surface : adhesive	0.108	0.018**
Adhesive : weathering	0.485	0.397
Bonded surface : weathering	0.315	0.766
Bonded surface : adhesive : weathering	N/A	N/A

Table 26. Effect of weathering on wood surface for energy to failure (only samples that failed between the notches).

Effect of weathering on wood surface	Energy to Failure DIC (n=26)	Energy to Failure Clip Gauge (n=26)
EE	0.536	0.981
EL	0.881	0.289
LL	0.244	0.983

Table 27. Effect of weathering on adhesive for energy to failure (only samples that failed between the notches).

Effect of weathering on adhesive	Energy to Failure DIC (n=20)	Energy to Failure Clip Gauge (n=20)
IMDI	0.247	0.287
IPH	0.971	0.341
IPL	N/A	N/A
IPLFE	0.386	0.765

4.1.3.4 Statistics Including Delaminated Samples

After running the statistical analysis with the above data, the samples that delaminated during the weathering were added to the analysis (Figure 44). The delaminated samples included one EL-IPH, two LL-IMDI, and two EL-IMDI. The

statistical analysis would not permit zero values. Therefore, these samples were entered as a value of 1 for the effective modulus and a value of 10^{-05} for the energy to failure. The same analysis procedure was followed for this dataset for the effective shear modulus and energy to failure. Table 28 - Table 30 list the statistical results for the effective shear modulus and Table 31 - Table 33 list the statistical results for the energy to failure, all including the delaminated samples.

Figure 44. Two IMDI samples that delaminated during weathering cycles.

The following results include the delaminated samples. The effective shear modulus was ~5 times greater for the EL non-weathered specimens, than the EL weathered specimens, from the DIC and clip gauge data (Table 29). The effective shear modulus was ~26 times greater for the IMDI non-weathered specimens, than the IMDI weathered specimens from both the DIC and clip gauge data (Table 30). The energy to failure (all specimens) was 16 times greater for the EL non-weathered specimens, than the EL weathered specimens, from the clip gauge data (Table 32). The energy to failure (all specimens) was 483 times greater for the IMDI non-weathered specimens, than the IMDI weathered specimens from the clip gauge data (Table 33).

The impact of the delaminated samples was large enough to make a significant difference in weathering for the IMDI samples. The deep penetration of the IMDI left a starved bondline that had a greater amount of shear strain and was more susceptible to

weathering. Weathering causes uneven swelling and shrinkage between the EW and LW sides of the bondline, potentially resulting in internal cracking and weak points.

Table 28. Three-way ANOVA for effective shear modulus, including the delaminated samples; ** denotes p-values that are significant.

Interactions	Effective Shear Modulus DIC (n=80)	Effective Shear Modulus Clip Gauge (n=80)
Bonded surface	0.547	0.498
Adhesive	0.007**	0.002**
Weathering	0.013**	0.033**
Bonded surface : adhesive	0.097**	0.149
Adhesive : weathering	0.003**	0.014**
Bonded surface : weathering	0.922	0.845
Bonded surface : adhesive : weathering	0.161	0.334

Table 29. Effect of weathering on wood surface for effective shear modulus, including the delaminated samples; ** denotes p-values are significant; numbers listed in bold and italicized represent the magnitude that the non-weathered specimens are greater than the weathered specimens.

Effect of weathering on wood surface	Effective Shear Modulus DIC (n=55)	Effective Shear Modulus Clip Gauge (n=55)
EE	0.908	0.994
EL	0.015** ***(5.360)***	0.017** ***(5.795)***
LL	0.908	0.842

Table 30. Effect of weathering on adhesive for effective shear modulus, including the delaminated samples; ** denotes p-values are significant; numbers listed in bold and italicized represent the magnitude that the non-weathered specimens are greater than the weathered specimens.

Effect of weathering on adhesive	Effective Shear Modulus DIC (n=35)	Effective Shear Modulus Clip Gauge (n=35)
IMDI	0.075** ***(27.031)***	0.063** ***(26.024)***
IPH	0.222	0.222
IPL	0.955	0.858
IPLFE	0.874	0.982

Table 31. Three-way ANOVA for energy to failure (all samples), including those that delaminated; ** denotes p-values are significant.

Interactions	Energy to Failure DIC (n=80)	Energy to Failure Clip Gauge (n=80)
Bonded surface	0.073**	0.744
Adhesive	.0000178**	0.000497**
Weathering	0.315	0.073**
Bonded surface : adhesive	0.102	0.060**
Adhesive : weathering	0.181	0.017**
Bonded surface : weathering	0.250	0.852
Bonded surface : adhesive : weathering	0.309	0.566

Table 32. Effect of weathering on wood surface for energy to failure (all samples), including those that delaminated; ** denotes p-values are significant; numbers listed in bold and italicized represent the magnitude that the non-weathered specimens are greater than the weathered specimens.

Effect of weathering on wood surface	Energy to Failure DIC (n=55)	Energy to Failure Clip Gauge (n=55)
EE	0.368	0.989
EL	0.390	0.066** ***(16.281)***
LL	0.437	0.937

Table 33. Effect of weathering on adhesive for energy to failure (all samples), including those that delaminated; ** denotes p-values are significant; numbers listed in bold and italicized represent the magnitude that the non-weathered specimens are greater than the weathered specimens.

Effect of weathering on adhesive	Energy to Failure DIC (n=35)	Energy to Failure Clip Gauge (n=35)
IMDI	0.654	0.072** ***(482.992)***
IPH	0.934	0.395
IPL	0.782	0.944
IPLFE	0.703	0.986

4.1.4 Percent Wood Failure

The percent of wood vs. adhesive failure was measured for those samples that failed between the notches. The delaminated samples are also reported here, with a percent wood failure value of zero (Table 34 and Figure 45). A statistical analysis was not conducted, but typically the weathered samples had a higher percent of wood failure, with the exception of the LL-IMDI samples. The EL-IPLFE samples had almost all wood failure, with little variation, for both the non-weathered and weathered samples. This indicated a quality bond, with the adhesive performing better than the wood, both before and after weathering.

Table 34. Percent wood failure including only specimens that failed between the notches and including the delaminated samples with a percent wood failure of zero; *means only one sample present in that sample group.

Sample Group	n	non-weathered average percent (COV)	n	weathered average percent (COV)
LL-IPL	2	97 (0.4%)	1	99*
EL-IPL	2	16 (115%)	1	38*
EE-IPL	3	82 (14%)	3	86 (21%)
LL-IPH	0	N/A	2	75 (41%)
EL-IPH	2	22 (137%)	6	58 (80%)
EE-IPH	3	41 (85%)	4	72 (39%)
EL-IMDI	2	10 (85%)	4	18 (117%)
LL-IMDI	1	81*	3	0 (0%)
EL-IPLFE	3	100 (0.06%)	4	100 (0.09%)

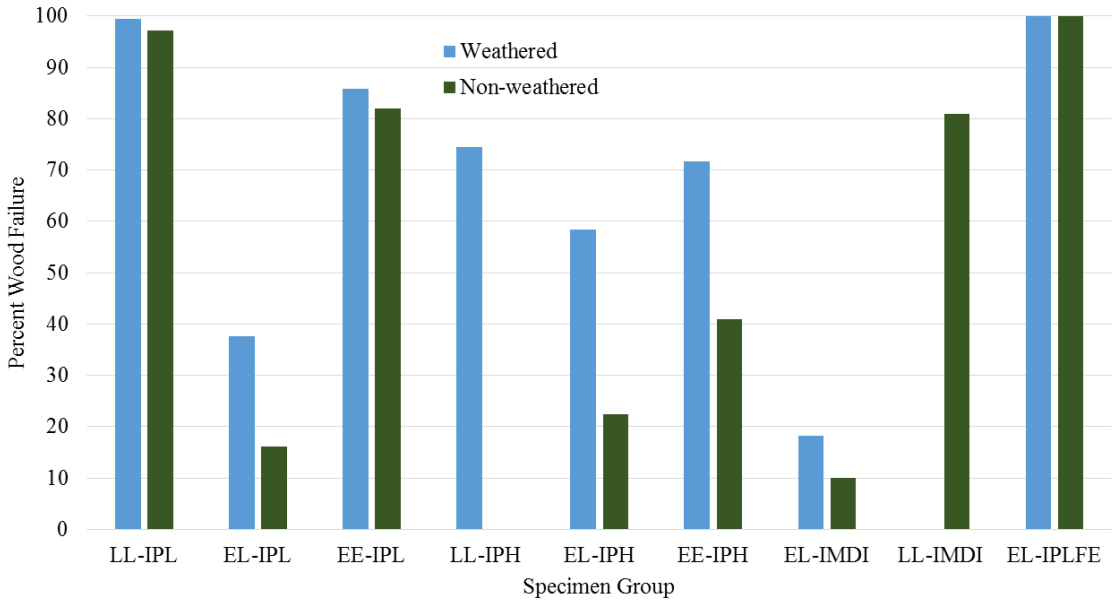

Figure 45. Percent wood failure including only specimens that failed between the notches and including the delaminated samples with a percent wood failure of zero.

4.1.5 Failure Modes

Comparisons were made on the failure mode for each sample and categorized into four modes: failure between the notches, failure outside the notches, failure both within and outside the notches, failure at the notch. Figure 46 - Figure 49 shows the percent of each sample group for each failure mode and an example image. The assessment of failure mode was performed after the test, and did not capture information regarding the initiation of failure during the test. The lap-shear test, with only a single bondline as used here, is difficult to interpret due to the complex loading that occurs. Pure shear at the bondline is sometimes not achieved, and failure occurs outside of the bonded region (outside of the notches). The calculation of effective shear modulus uses data collected early in the test before significant out-of-plane deformation occurs, and therefore, was least affected by complex loading. Nevertheless, the failure information provided some semi-quantitative evidence of bond performance.

Few LL specimens for any adhesive type failed between the notches. None of the non-weathered LL-IPH samples failed between the notches (Figure 46), therefore no assessment of ultimate shear stress can be stated. Although, the maximum load capacity of the bonded area for the LL-IPH samples was as least as great as the maximum load recorded. The LL samples had a higher average failure load than the EE and EL samples, for the IPL and IPH samples (Figure 33). Figure 47 shows that 40% of the samples in the LL-IPH group failed outside the notched area. At high applied load to an asymmetrical lap-shear specimen, the sample begins to twist and create significant bending stress in the specimen, particularly in the region of the notches. This results in failure outside of the notched region, and often in the wood.

Most of the EE samples failed between the notches and also had a lower average failure load than the LL and EL samples for the IPL and IPH adhesives (Figure 46).The EL-IPLFE samples had the most overall that failed between the notches (Figure 46) and the highest percent of wood failure, with the least variability (Figure 45). However, there is no clear trend between the failure mode and percent wood failure.

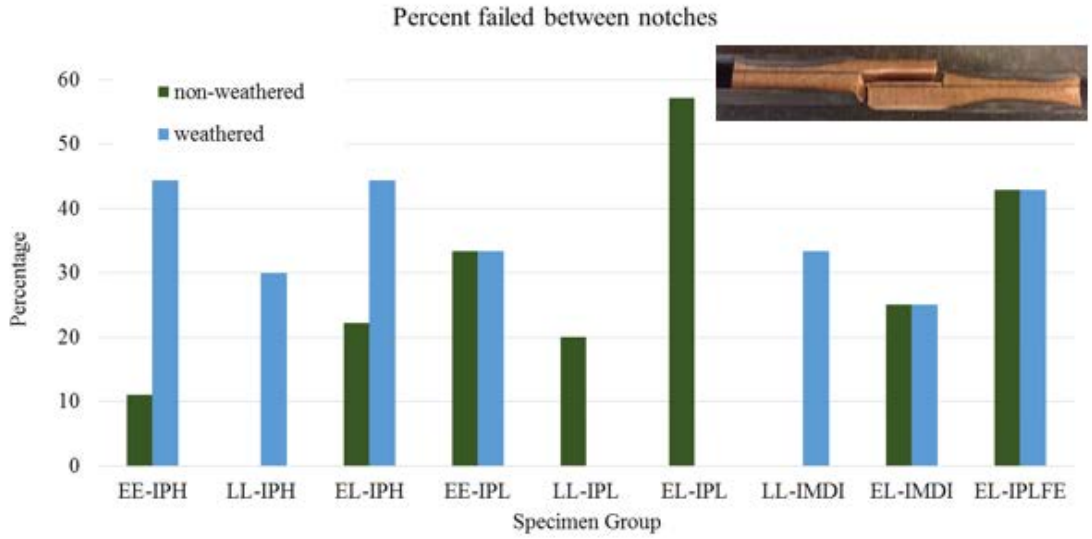

Figure 46. Percent of each sample group that failed between the notches.

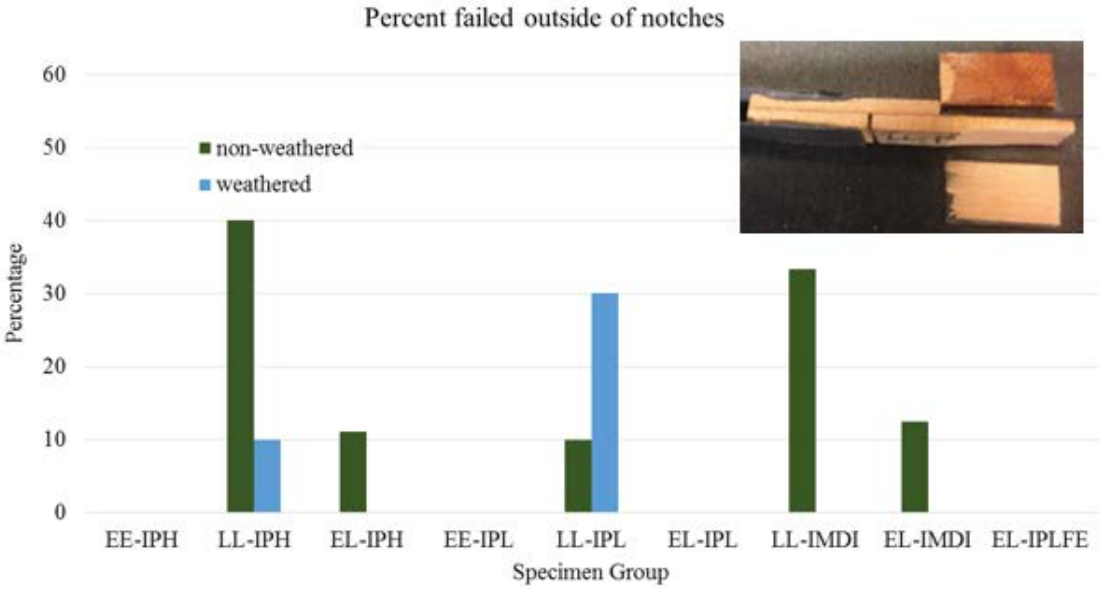

Figure 47. Percent of each sample group that failed outside the notches.

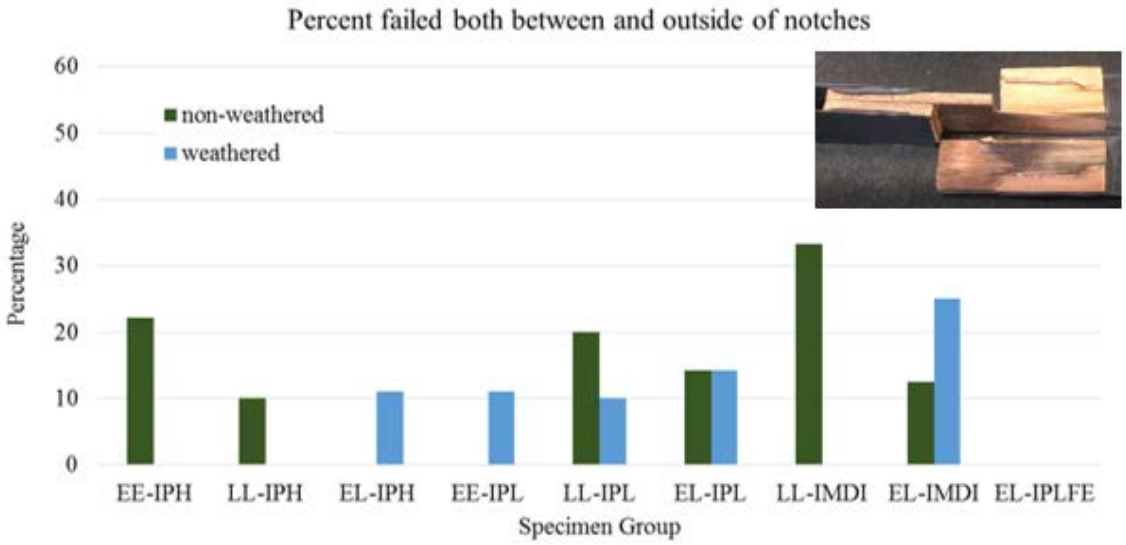

Figure 48. Percent of each sample group that failed both within and outside the notches.

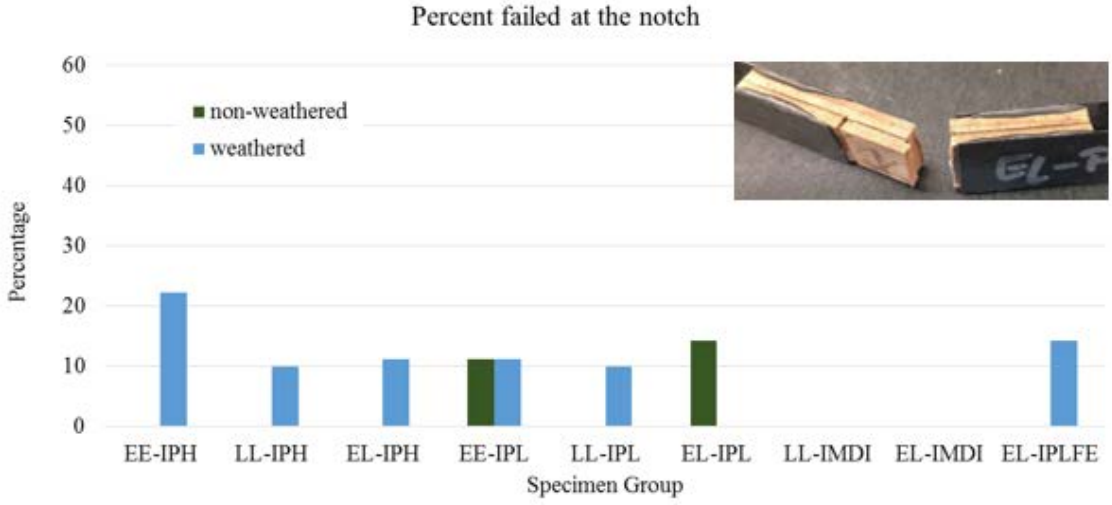

Figure 49. Percent of each sample group that failed only directly at the notch, in pure wood failure.

4.1.6 DIC Shear Strain Map Visual Comparisons

DIC shear strain maps were used to qualitatively compare the behavior of each sample type. Figure 50 shows examples of only EL samples (with EW on the left side of the bondline) for each adhesive type, after weathering exposure. This shear strain behavior is indicative of the samples within each treatment. The IPH and IMDI samples have a greater amount of shear strain at the same loads as the IPL and IPLFE samples, with the same bonded wood surface. Penetration of the adhesive at the interphase was located within the AOI, meaning that the presence of penetration should be visible and theoretically will result in a more uniform shear strain across that area. The bulkiness of the IPH seems to result in a higher amount of shear strain directly at the bondline, which could be attributed to the differences in wood and adhesive properties. The deep penetration of the IMDI seems to cause scattered shear strain around, but not directly at the bonded interphase.

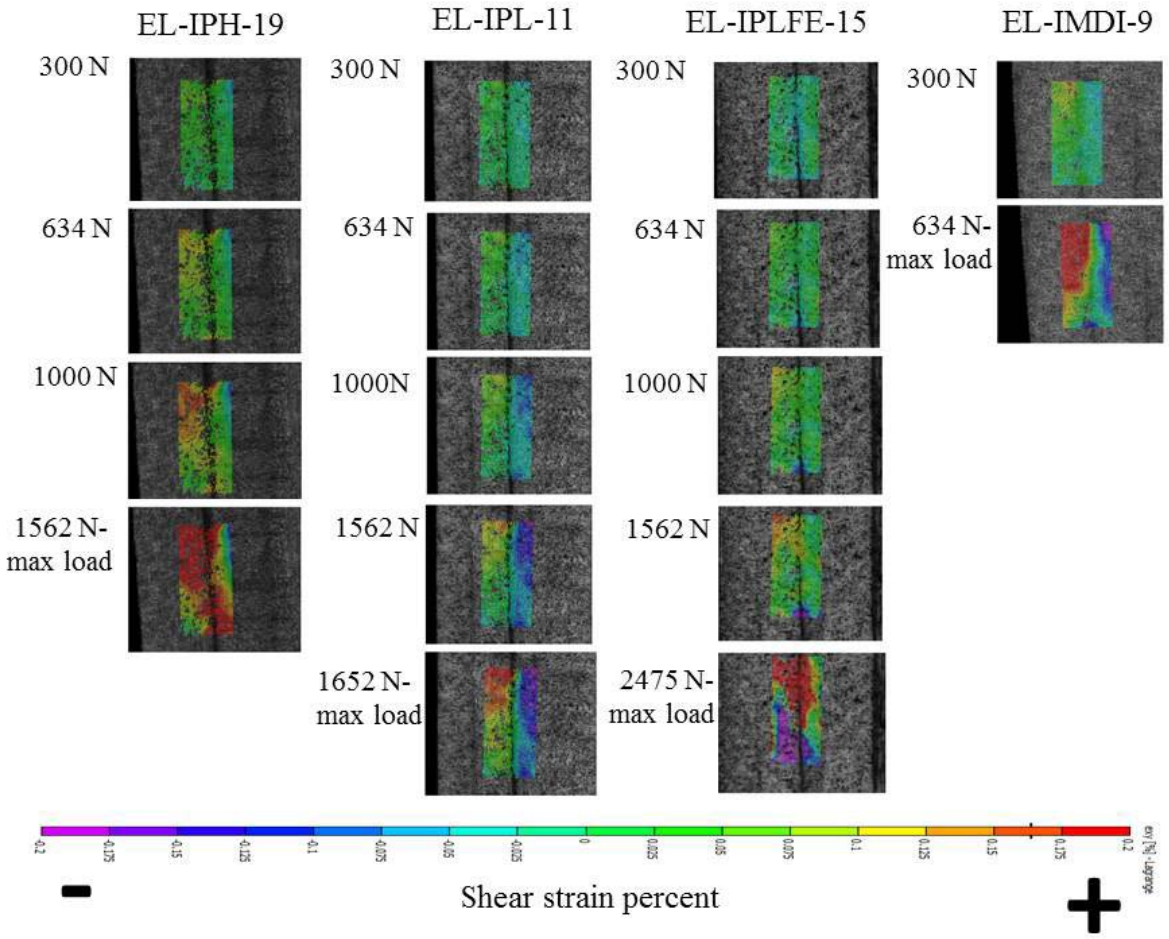

Figure 50. DIC shear strain map comparison for each adhesive type after weathering; all samples are EL with the EW on left of central bondline; load is increased as shown from top to bottom until maximum load.

The two adhesive types and bonded wood surfaces that had significant differences after weathering were the IPH and IMDI adhesives and EL bonded wood surface. Figure 51 shows a non-weathered EL-IPH sample compared to a weathered sample. Up until 600 N they both had a uniform distribution of shear strain around the bonded area. However, at 600 N the weathered sample had a much greater amount of shear strain than the non-weathered sample. This uneven shrinkage and swelling of the EW vs. LW seems to be more of an effect in the bulky bondline of the IPH. It could be that the thick, brittle

IPH bondline, which has a different rate of shrinking and swelling than the wood substance, causes internal cracking and defects that are not present with the IPL, which could have an interphase of a more even rate of shrinking and swelling.

A similar behavior is seen in the EL-IMDI samples (Figure 52) where the weathered sample had a greater amount of shear strain around 500 N than the non-weathered sample. IMDI tends to have a deep penetration, with the opposite effect of the IPH, creating a starved interphase that performs poorly after weathering exposure, especially with the differences in EW and LW on either side of the bondline.

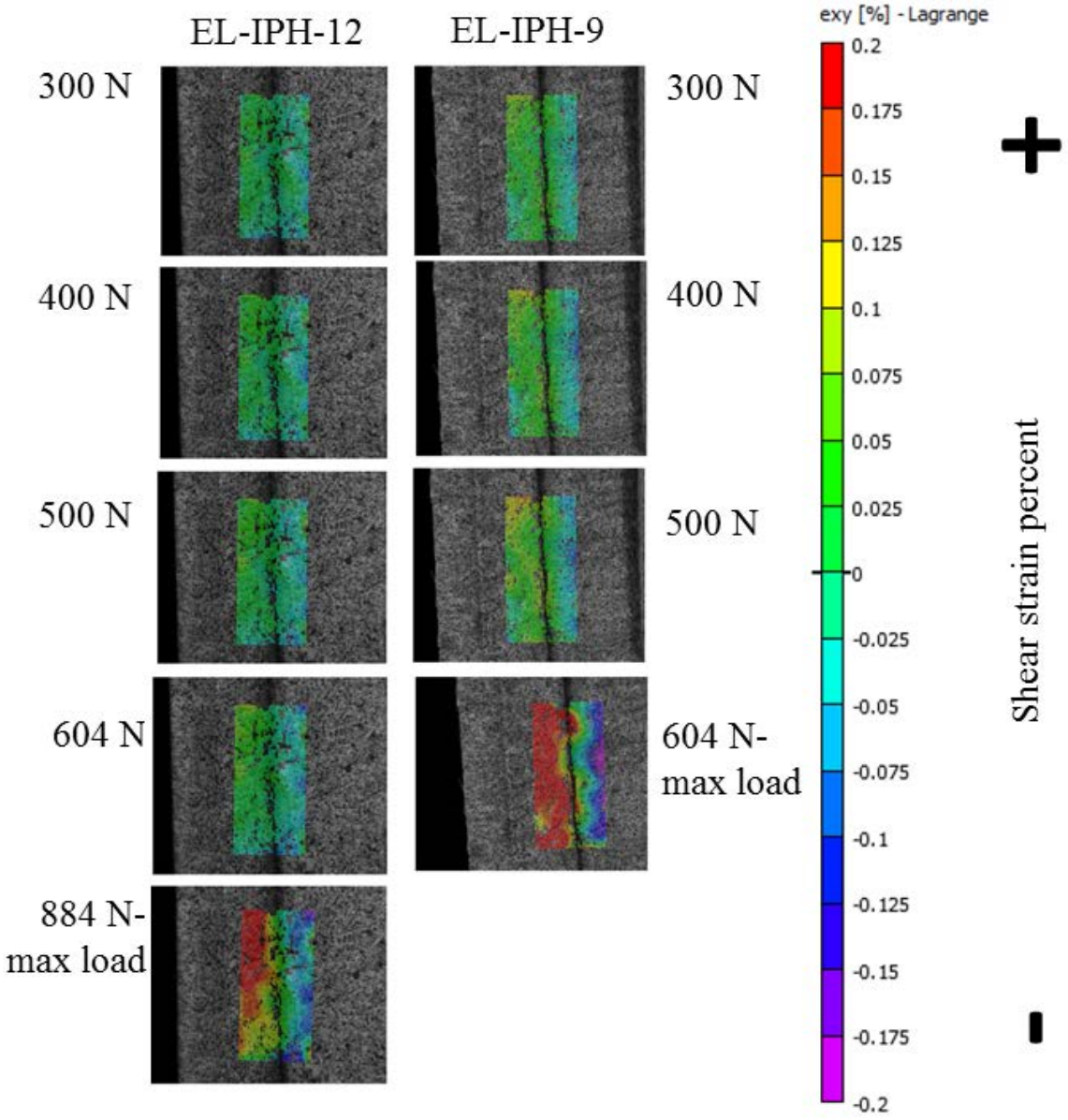

Figure 51. DIC shear strain maps of a non-weathered EL-IPH sample on left and a weathered EL-IPH sample on right; both samples are EL with the EW on left of central bondline; load is increased as shown from top to bottom until maximum load.

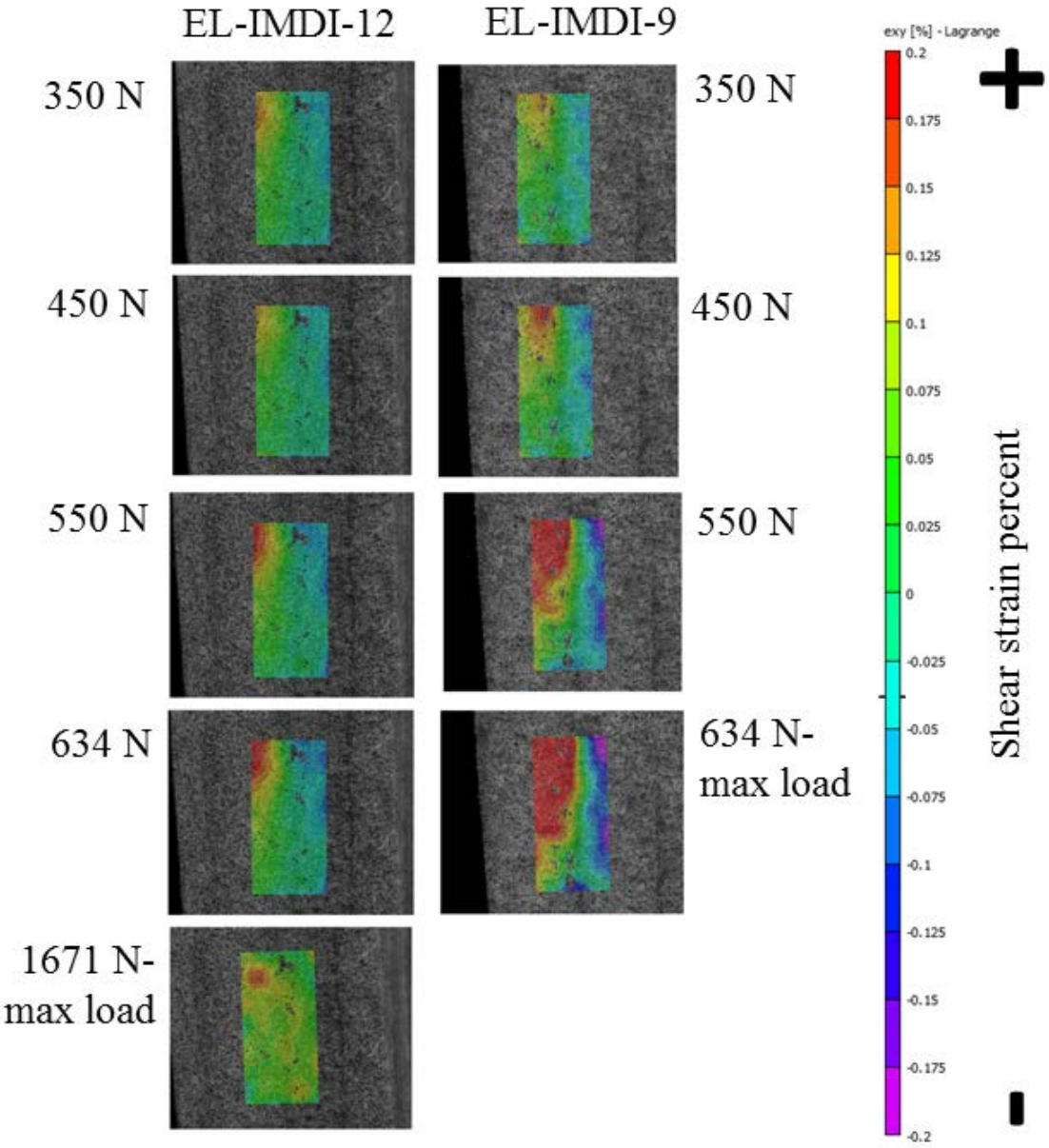

Figure 52. DIC shear strain maps for a non-weathered EL-IMDI sample on the left and a weathered EL-IMDI sample on the right; both samples are EL with the EW on left of central bondline; load is increased as shown from top to bottom until maximum load.

Although a statistical analysis with such a small sample size is unlikely to reveal significant differences, the average effective shear modulus for the weathered samples, for both the IPL and IPH were evaluated (Table 35). While there is no statistically significant difference in the two adhesives after exposure to weather cycling, the IPL tends to have a higher average effective shear modulus (stiffness), except in the EE samples, where the stiffness is very similar. As will be shown later, both IPL and IPH readily penetrated the large lumens found in the EW. Table 35 also shows a higher average effective shear modulus for LL specimens compared to EE specimens, which is expected, since less resistance to shear force is provided by the thin cell walls of EW. Unfortunately, only one EL-IPL specimen was available for comparison. The results in Table 35 suggest that there is an effect of bonded surface, as well as adhesive type, on the shear properties of the bondline for the IPH and IPL samples.

Table 35. Comparison of effective shear modulus for IPH and IPL weathered samples only, excluding any specimens that delaminated during weathering; * denotes group with only one sample.

Specimen	n	Failure Load (N)	Effective Shear Modulus (MPa)	Energy to Failure (J)
LL-IPH	5	1,381 (53%)	13,715 (58%)	0.161739 (211%)
LL-IPL	5	1,321 (21%)	32,055 (74%)	0.011227 (90%)
EE-IPH	4	486 (46%)	4,866 (82%)	0.009329 (51%)
EE-IPL	5	403 (48%)	4,520 (57%)	0.003034 (56%)
EL-IPH	6	586 (79%)	8,756 (115%)	0.013372 (104%)
EL-IPL	1	1,208*	11,355*	0.004734*

Visual comparisons were made of each of the specimen variations listed in Table 35, between the weathered and non-weathered samples (Figure 53 - Figure 55). Based on the surface shear stain maps for the IPL and IPH weathered samples, there was more

shear strain in the IPH samples than in the IPL samples. Although, the EE samples are similar (Figure 54), which is also seen in the differences in average effective shear moduli. The failure load, effective modulus, and energy to failure measurements have greater variation in the EL specimens, potentially due to differences in lumen and/or cell wall adhesive penetration. This may be attributed to the EW portion of the EL samples having adhesive penetration into the EW cell substance, creating a more uniform mixture of wood and adhesive. In turn, the LW could have little penetration and a large difference in deformation rate between the wood and adhesive, after weathering exposure (Figure 55). The LL-IPL had a similar average maximum load to the LL-IPH samples, but almost three times the effective shear modulus (Table 35). Figure 53 shows that there is a higher amount of shear strain in the LL-IPH samples at a same given load, than the LL-IPL samples. The LL-IPH samples also have a lower average stiffness (effective shear modulus) than the LL-IPL samples (Table 35).

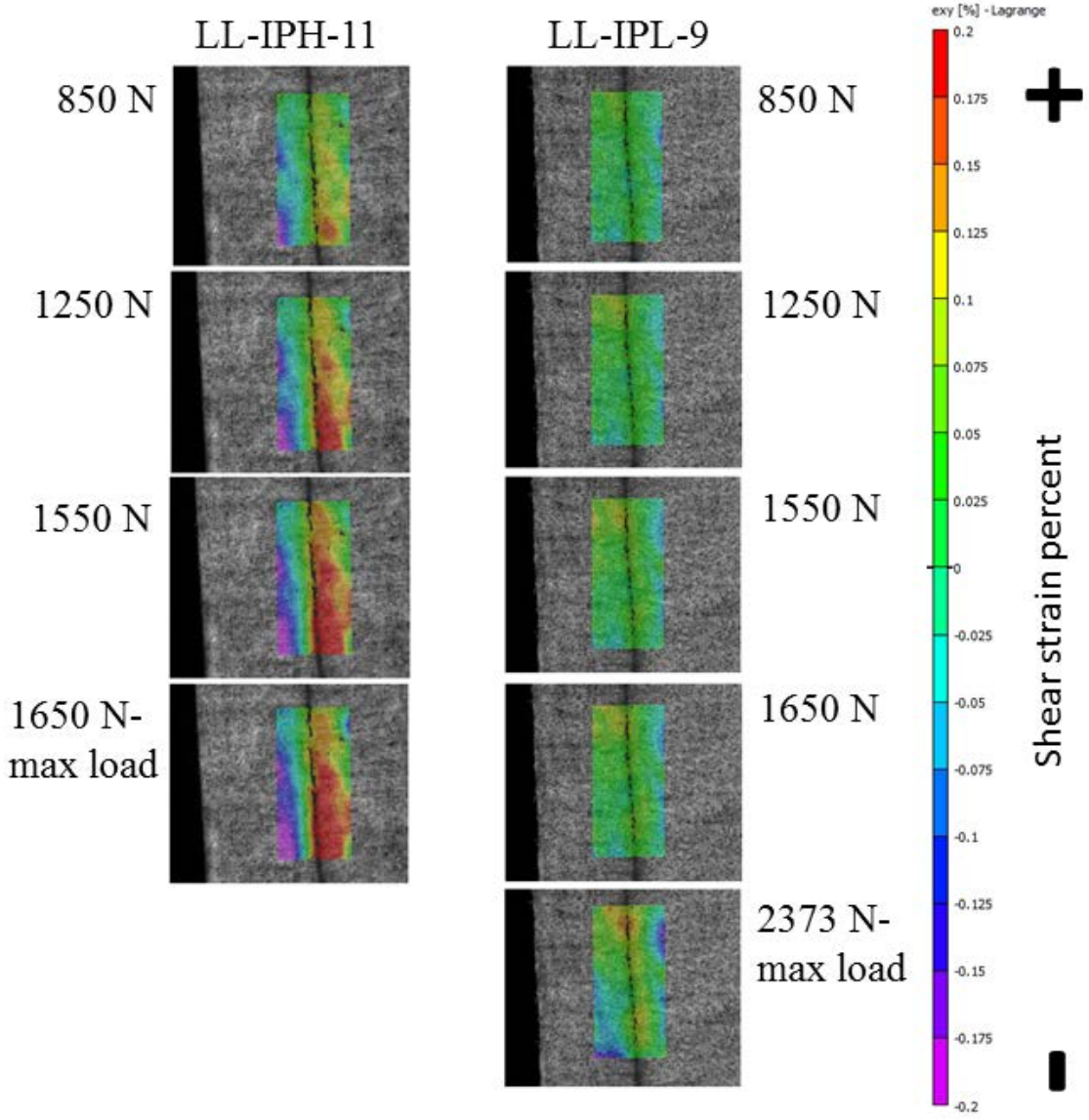

Figure 53. DIC shear strain map comparison of a weathered LL-IPH on left and a weathered LL-IPL on right; load is increased as shown from top to bottom until maximum load.

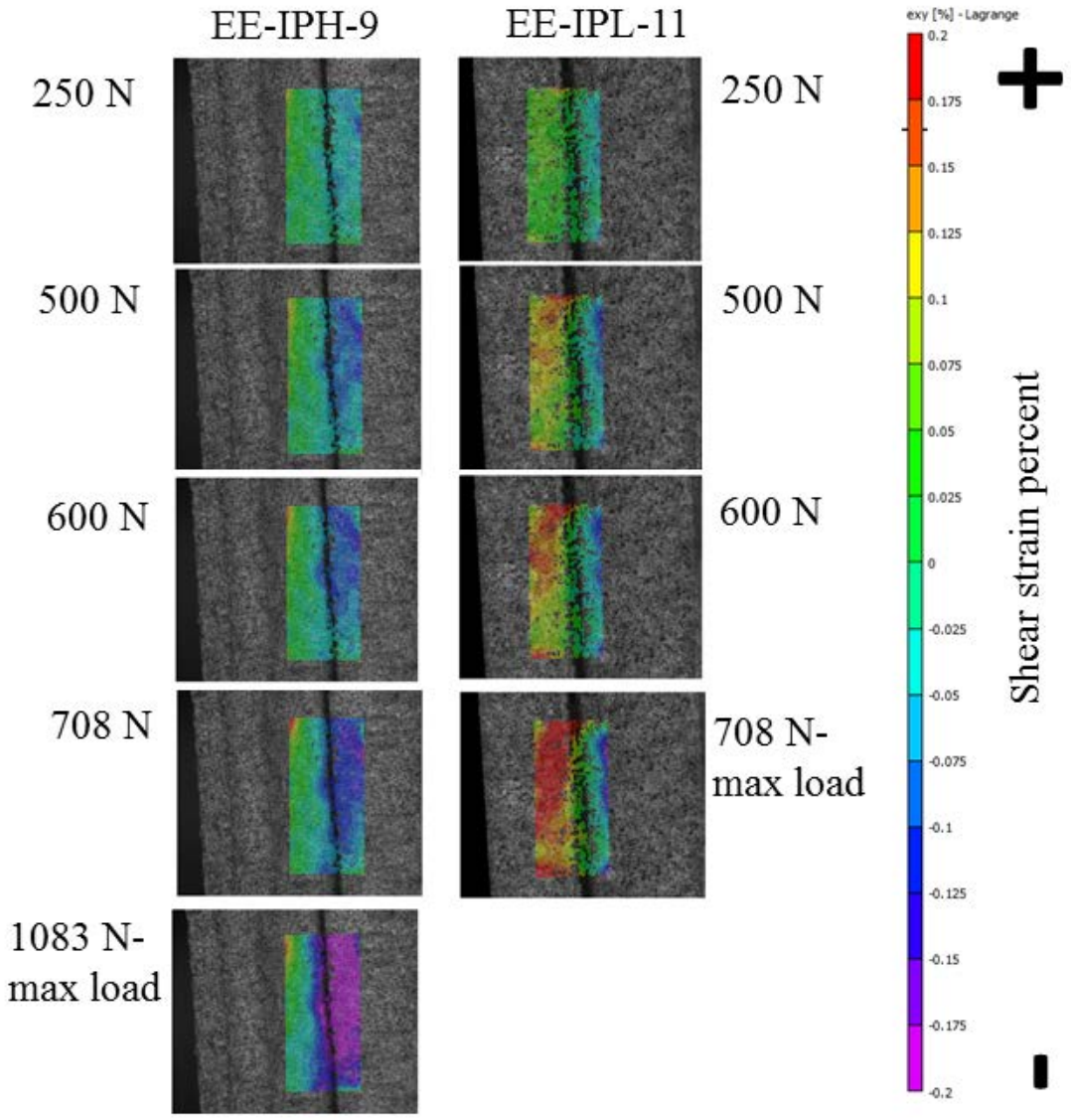

Figure 54. DIC shear strain map comparison of a weathered EE-IPH on left and a weathered EE-IPL on right; load is increased as shown from top to bottom until maximum load.

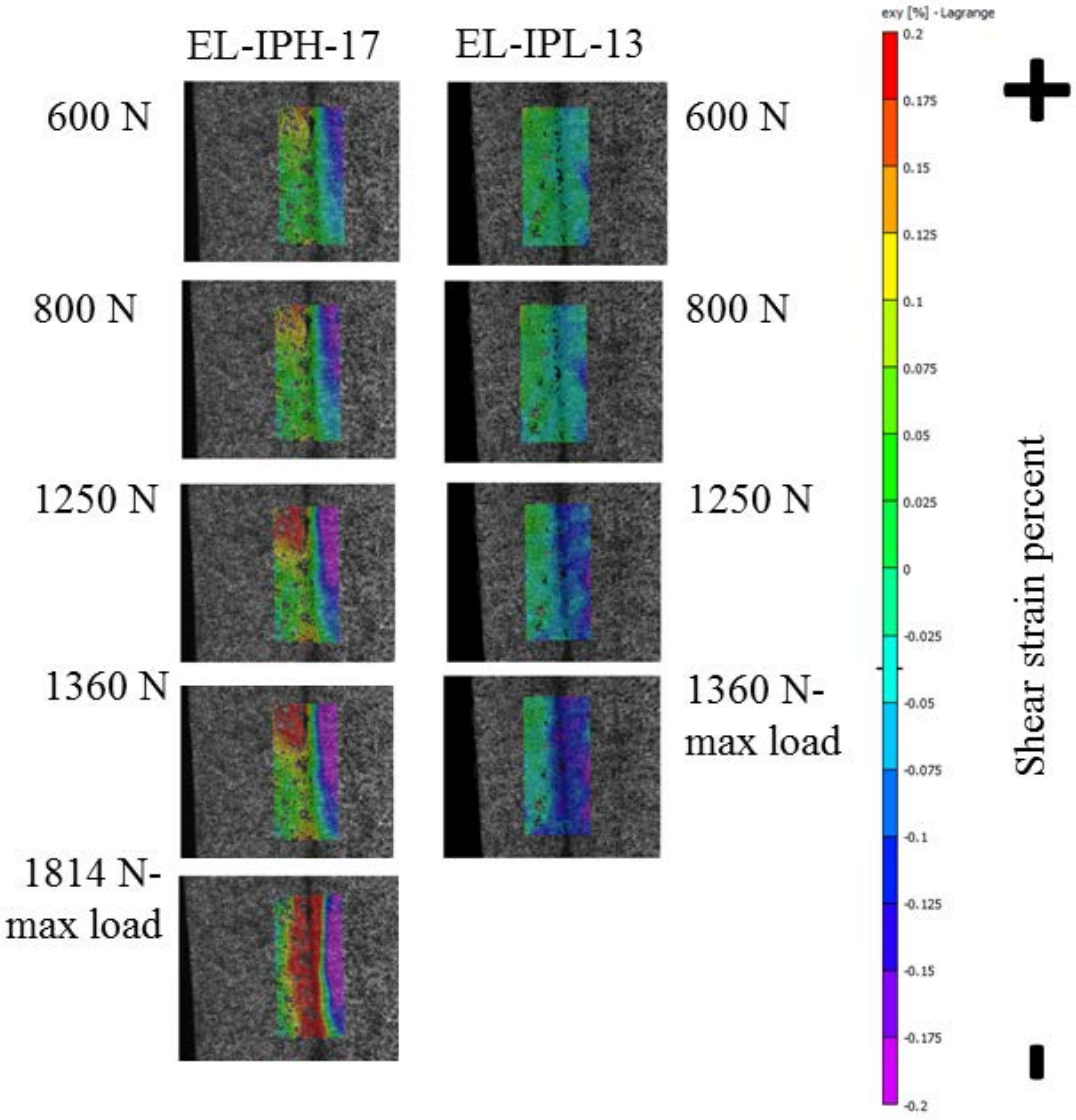

Figure 55. DIC shear strain map comparison of a weathered EL-IPH on left and a weathered EL-IPL on right; both samples are EL with the EW on left of central bondline; load is increased as shown from top to bottom until maximum load.

4.2 Micro X-ray Computed Tomography

4.2.1 Microweathered Specimens

The data collected from the microweathered micro-XCT experiment was qualitatively used to compare samples scanned before weathering and data collected after the weathering procedure. Several examples of differences in parallel and cross-laminated samples are shown in Figure 56 - Figure 59. The IPL specimen (Figure 56) shows greater adhesive penetration than the IPH specimen (Figure 58). Very little adhesive was able to penetrate the LW regions of any specimens. The cross-laminated specimen shown in Figure 59 had LW on both sides of the bondline in the slice shown, however the sample transitioned between EW and LW throughout the dataset. The parallel-laminated samples were more stable after weathering than the cross-laminated samples, due to differences in shrinkage values between the two directions. The longitudinal direction of the cross-laminated specimens provided some restrain to shrinking and swelling of the adjacent lamina, which caused some plastic deformation that was observed in the tangential direction. Plastic deformation is particularly evident in Figure 57 when comparing the width of the lower lamina before and after weathering. The IPH cross-laminated sample only had a small crack after weathering (Figure 59) whereas the IPL sample (Figure 57) had large cracking and noticeable delamination. Perhaps the greater penetration of the IPL provides less resistance to dimensional change than IPH, and therefore, provides a bondline that is less resistant to the influence of water. In some cases, the microweathered samples show evidence of compression set, which is a permanent plastic deformation of the wood in the tangential direction as a

result of the restraint imposed by the longitudinal direction of the cross-laminated specimen. Figure 57 shows an internal crack perpendicular to the bonded interface, as well as a delamination, caused by the restraint. Despite the crack present in Figure 57, the overall width of the weathered sample is less than the sample before weathering.

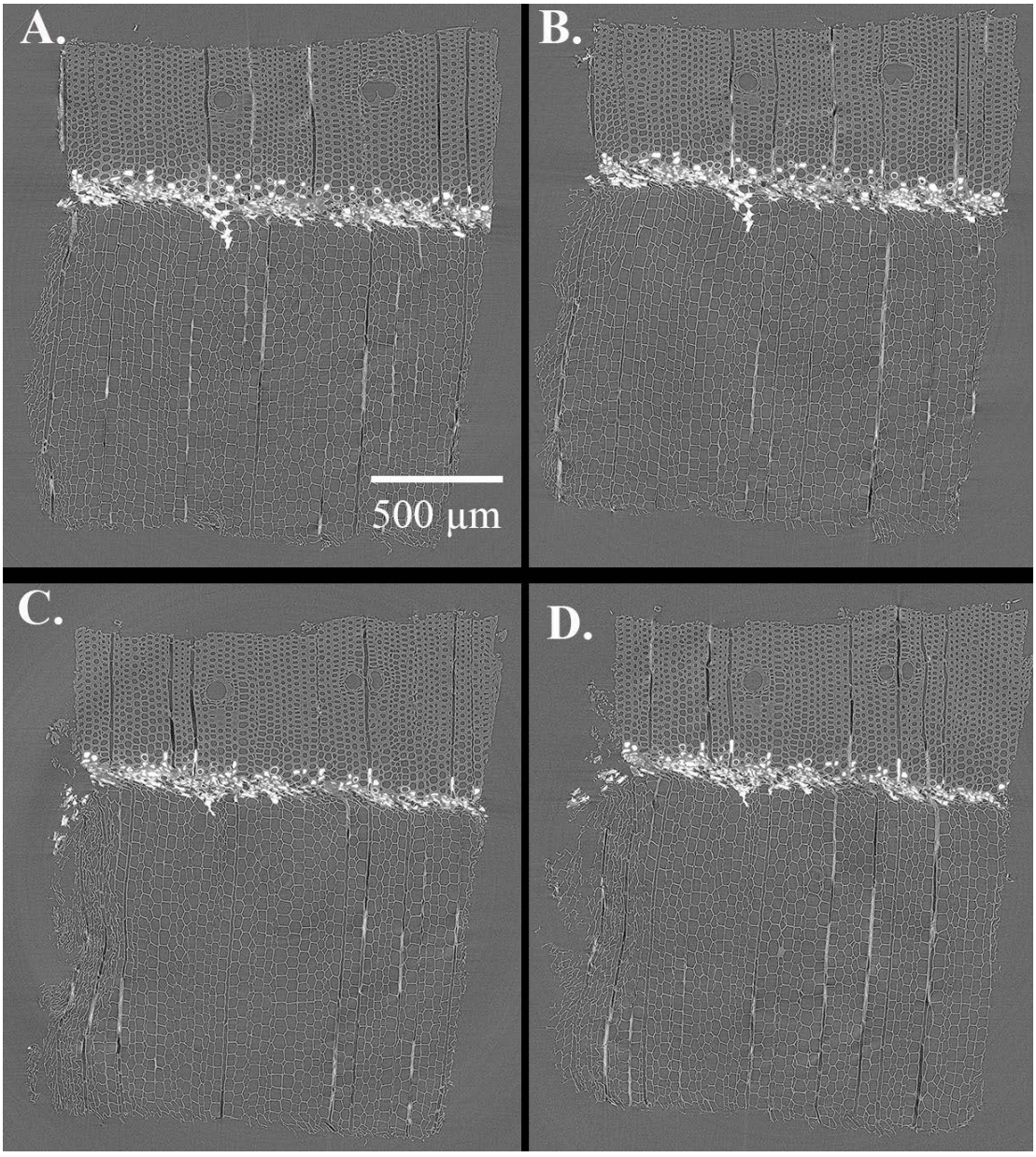

Figure 56. Parallel laminated microweathered EL-IPL-A2 micro-XCT sample; A.) before weathering (slice #506); B.) slice A after weathering (slice #699); C.) before weathering (slice #1586); D.) slice C after weathering (slice #1777).

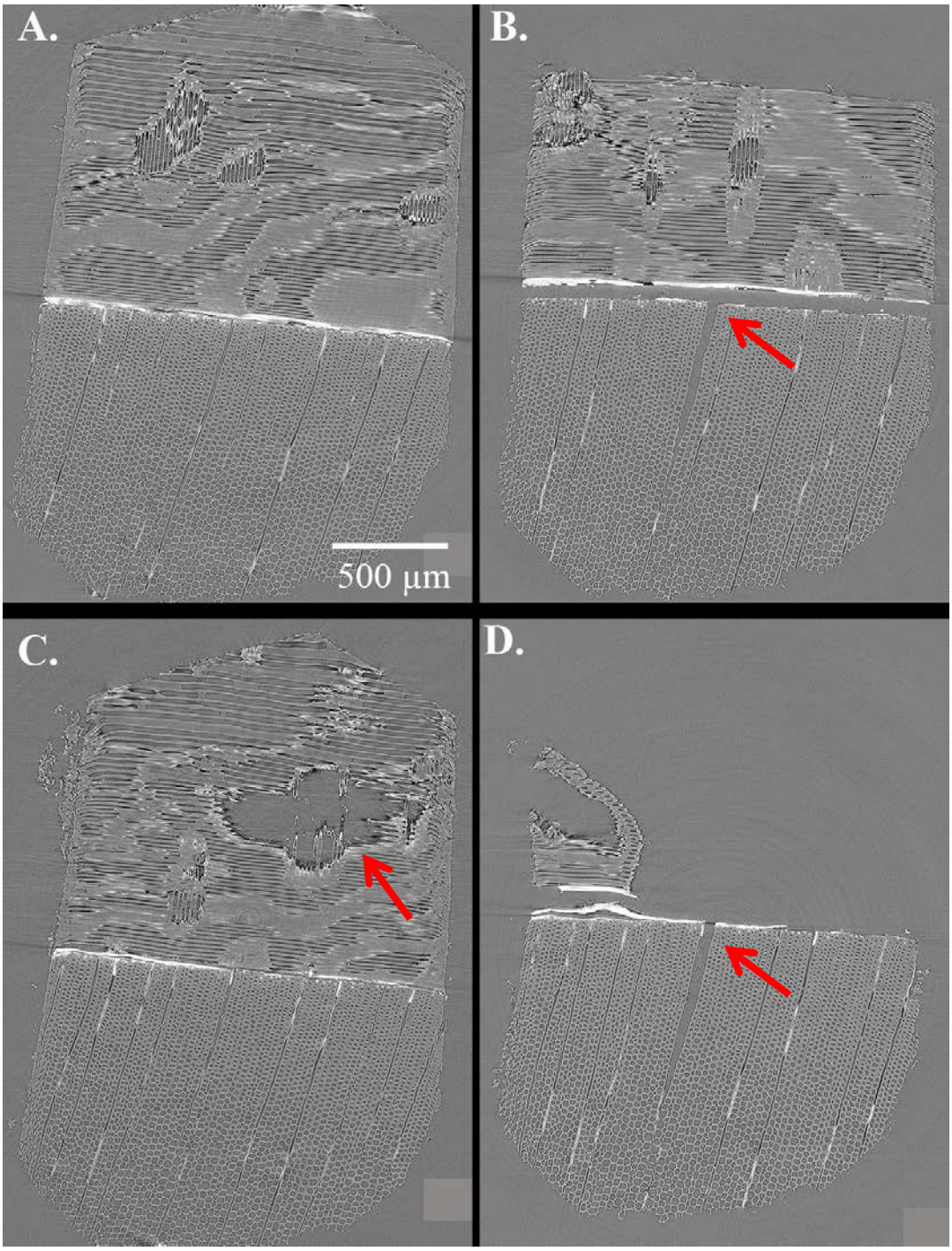

Figure 57. Cross-laminated microweathered EL-IPL-D2 micro-XCT sample, however this slice is LL and transitions to EL throughout the dataset; A.) before weathering (slice #1642); B.) slice A after weathering (slice #1483); C.) before weathering (slice #1665); D.) slice C after weathering (slice #1809).

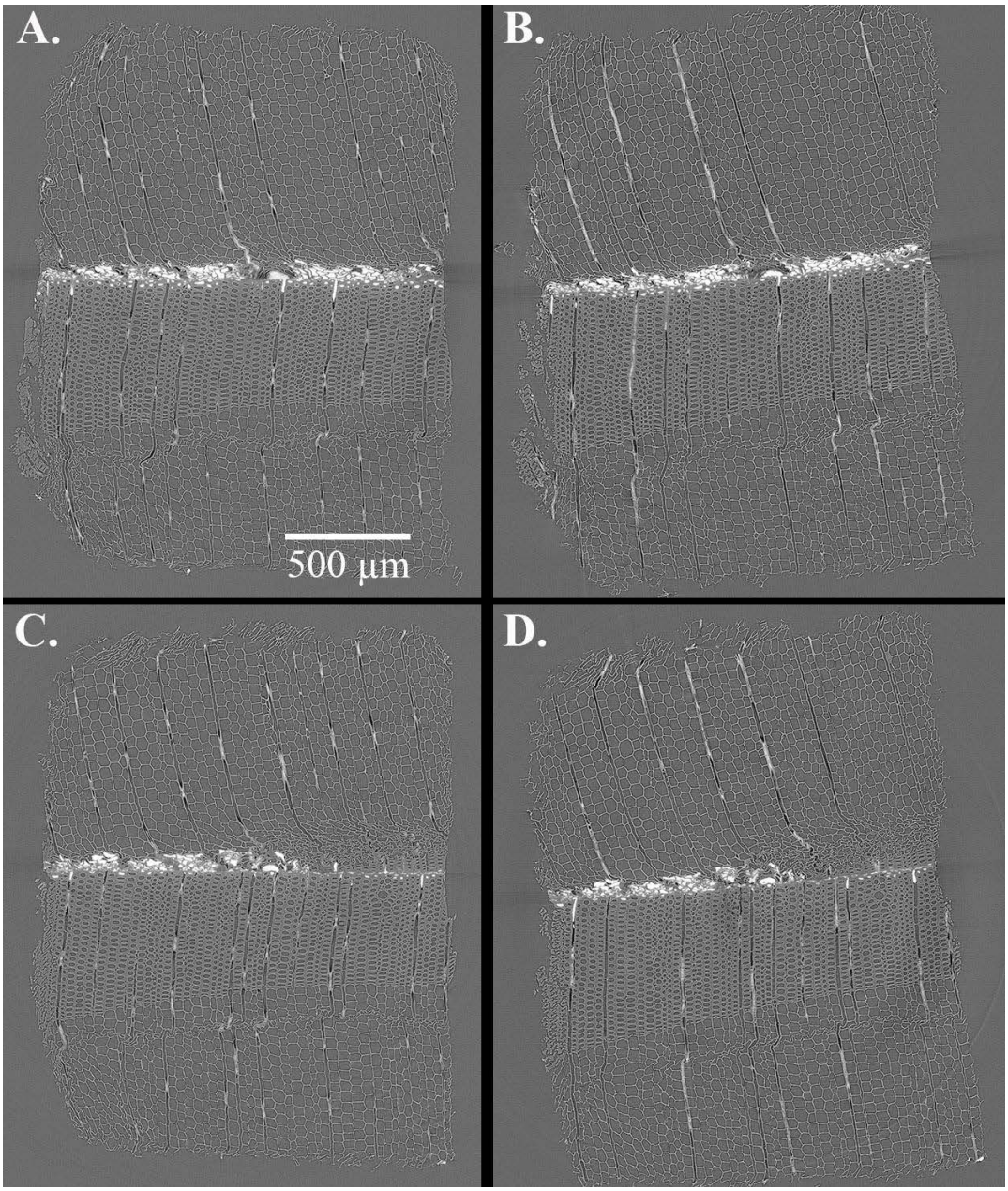

Figure 58. Parallel laminated microweathered EL-IPH-L1 micro-XCT sample; A.) before weathering (slice #1650); B.) slice A after weathering (slice #1182); C.) before weathering (slice #1012); D.) slice C after weathering (slice #556).

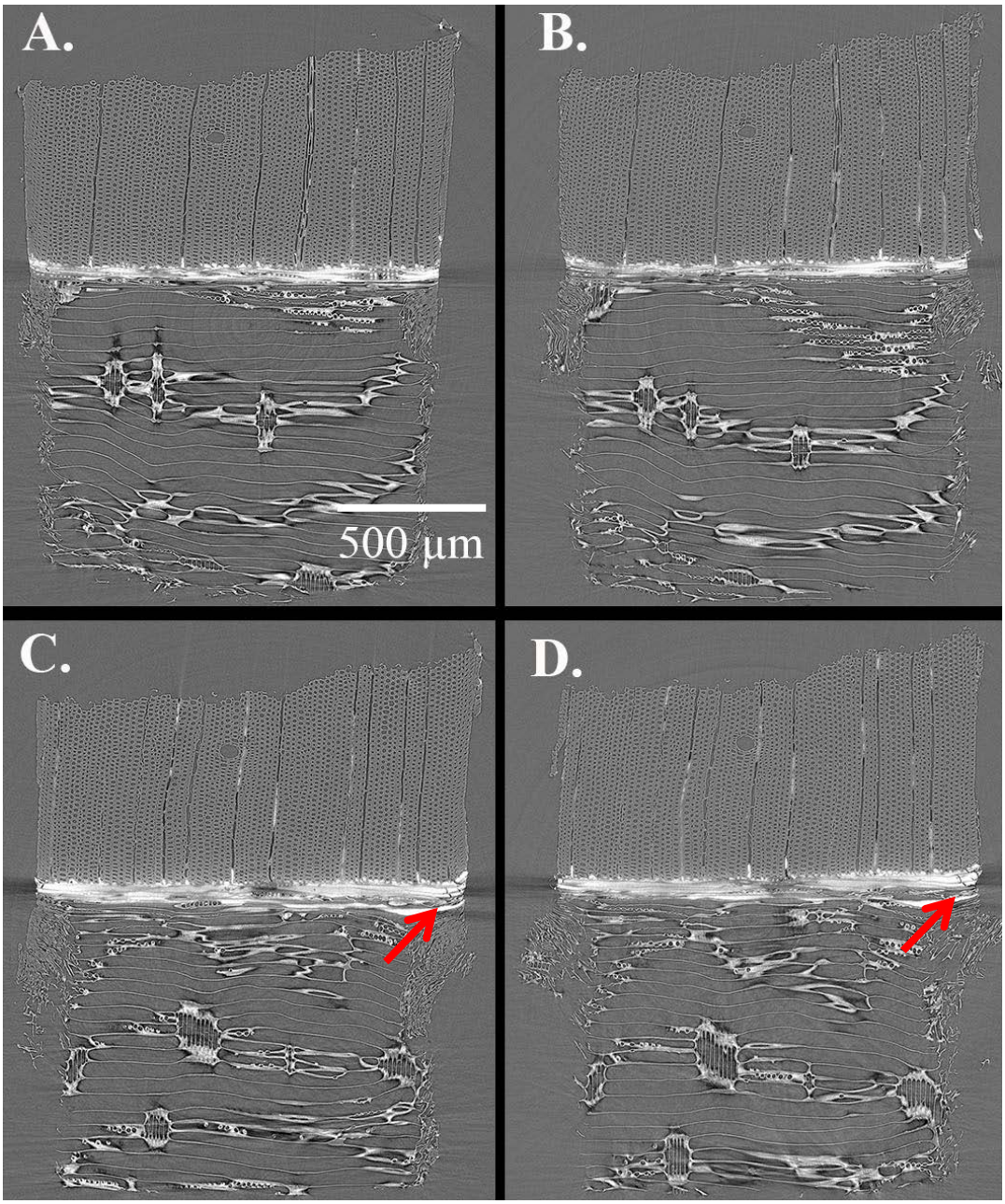

Figure 59. Cross-laminated microweathered EL-IPH-M2 micro-XCT sample; A.) before weathering (slice #646); B.) slice A after weathering (slice #499); C.) before weathering (slice #1432); D.) slice C after weathering (slice #1285).

4.2.2 Macroweathered Specimens

The macroweathered micro-XCT specimen group includes both dry and macroweathered specimens. These results were used to quantify the amount of adhesive penetration in order to make conclusions about the effect of adhesive penetration on moisture resistance. The results from the EP and WP are listed in Table 36. Examples of IPL and IPH samples are shown in Figure 62 and Figure 63. Additional datasets are listed in Appendix A. There is a greater amount of EP in the IPL samples, but with higher variation. The WP results are very similar for the two adhesive formulations. Variability can be attributed to the differences in EW vs. LW, although even within the same specimen, there are large differences in the EP calculations. When comparing only the EE samples, the average EP and WP for the EE-IPL samples is 56.5 µm and 69.9 µm, respectively. The EE-IPH samples have an average EP and WP of 42 µm and 47.4 µm, respectively. This shows a 35% and 48% increase for the EP and WP, respectively, comparing the IPL specimens to the IPH.

Table 36. Effective and weighted penetration results for each micro-XCT sample; averages for IPH and IPL with the COV listed in parentheses.

Sample	EP (µm)	WP (µm)
EE-IPH-2	45.28	63.76
EE-IPH-3	38.71	31.06
EL-IPH-4	15.52	92.06
EL-IPH-2	58.16	68.73
EL-IPH-6	33.32	86.84
EE-IPL-2	15.74	49.77
EE-IPL-1	51.97	62.74
EE-IPL-3	55.80	97.33
EE-IPL-4	102.67	67.19
EL-IPL-1	21.84	55.34
Average (COV) IPH	38.20 (41%)	68.49 (35%)
Average (COV) IPL	49.60 (69%)	66.48 (28%)

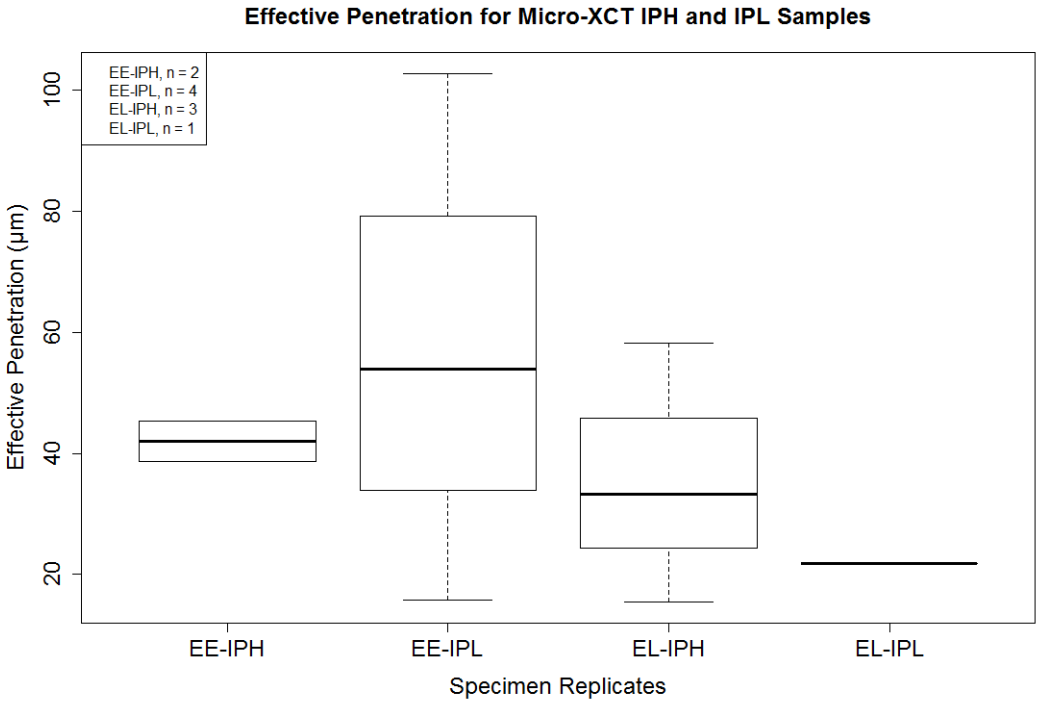

Figure 60. Effective penetration measurements for IPH and IPL samples; the black line in the middle of each box represents the median; the outer edges of the box represent the 25th and 75th percentile; the top whisker represents the maximum value and the bottom whisker represents the minimum value.

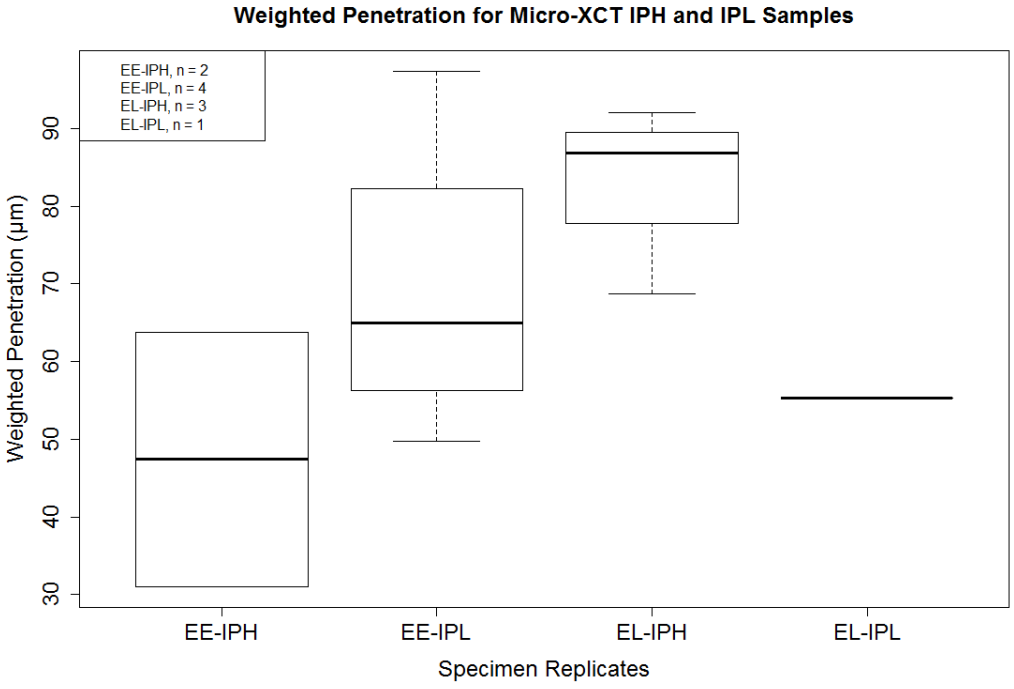

Figure 61. Weighted penetration measurements for IPH and IPL samples; the black line in the middle of each box represents the median; the outer edges of the box represent the 25th and 75th percentile; the top whisker represents the maximum value and the bottom whisker represents the minimum value.

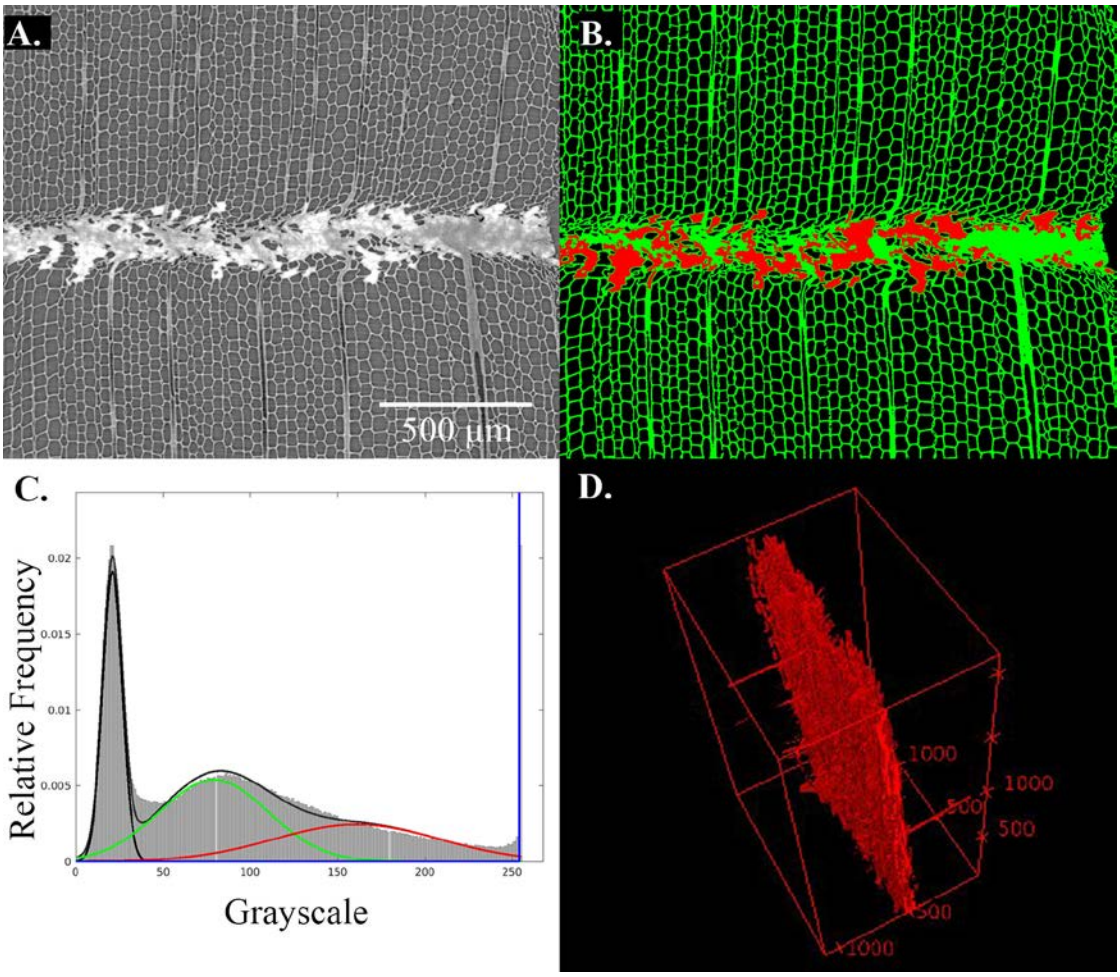

Figure 62. Micro-XCT segmentation of EE-IPL-2; A.) original micro-XCT slice; B.) micro-XCT slice after color mapping; C.) distribution of grayscale values (8-bit); black peak is void space, green peak is wood substance, red peak is adhesive penetration into cell substance, blue peak is pure adhesive; D.) combined pure adhesive and penetration phases in 3D with the full dataset outlined by the red box.

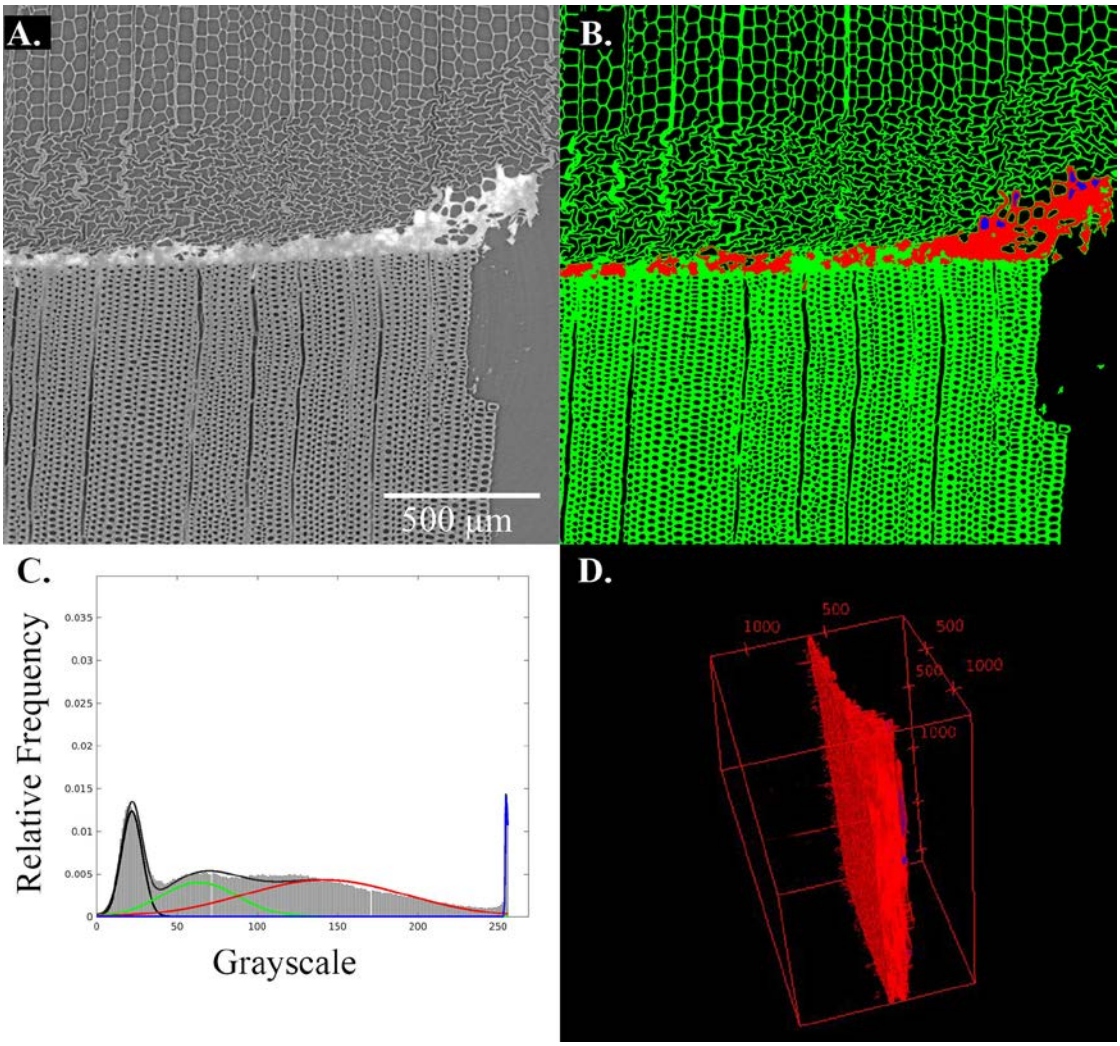

Figure 63. Micro-XCT segmentation of EL-IPH-2; A.) original micro-XCT slice; B.) micro-XCT slice after color mapping; C.) distribution of grayscale values (8-bit); black peak is void space, green peak is wood substance, red peak is adhesive penetration into cell substance, blue peak is pure adhesive; D.) combined pure adhesive and penetration phases in 3D with the full dataset outlined by the red box.

4.3 Nano X-ray Computed Tomography

Previously scanned micro-XCT samples were used as master samples to section and scan the nano-XCT samples. An objective of the nano-XCT experiment was to be able to locate the nano-XCT sample within the micro-XCT dataset. Figure 64, Figure 68, and Figure 73 show the procedure for locating the nano-XCT sample within the micro-XCT dataset. These were the best quality nano-XCT samples and the only ones used for the adhesive penetration analysis. Figure 69 shows anatomical features like ray pitting and ray cell diameter in Douglas-fir that were used to measure and locate features within the nano-XCT datasets. The other datasets had poor reconstruction quality and could not be successfully used for identification within the original micro-XCT dataset. They also could not be used for the penetration analysis. The PAA treated samples did not provide better contrast due to the variability in attenuation values within the delignified cell wall, which was not expected. In addition, these samples were difficult to locate within the original micro-XCT dataset, due to the extra handling and loss of some cell structure from the treatment. Figure 76 shows the porous cell structure of a nano-XCT sample after PAA treatment.

Comparison cannot be made between the IPH and IPL and the effect of adhesive penetration since there were not any quality datasets for the IPH samples that were scanned. The XFM data is at a lower resolution than the nano-XCT data, but XFM will be used to determine adhesive penetration in the IPH and IMDI samples. The gradient of grayscale values of the IPL samples shows that there is adhesive penetration into the cell substance, seen by the gradual slope at the lumen-cell wall interphase in Figure 65 -

Figure 67, and Figure 70 - Figure 72, and Figure 74 and Figure 75. The nano-XCT image slices were not processed, but there can sometimes be a difference in the background grayscale values when viewing different slices within the dataset. The CML has a slightly higher x-ray attenuation value, but this may be due to differences in cell wall density, and not the presence of adhesive. At 60 nm^3/voxel resolution, every adhesive molecule cannot be distinguished, but there is a definite gradient from the adhesive-filled lumen into the adjacent cell wall. If no penetration was present, the transition region between adhesive and cell substance would be nearly a vertical line. The example shown in Figure 65 suggests approximately 600 nm penetration into the cell wall, which corresponds to about 10 voxels, which is seen in the other penetration analysis figures. Figure 70 shows hardly any penetration into the cell substance whereas Figure 71 shows almost 2.5 µm of penetration. This variability makes conclusions more difficult to make. While poor image quality can produce somewhat fuzzy edges, the same grayscale profile method shows a more abrupt transition (3 to 4 voxels) between adhesive and void, and between cell wall and void. This evidence of cell wall penetration is consistent with evidence shown later using XFM.

There was a decrease in x-ray attenuation found within the cell lumen filled with adhesive, in some datasets (Figure 65-67 and Figure 72). The decrease in attenuation occurred adjacent to the cell wall and was a phenomenon that was not expected. The author is unsure if it was caused by the iodine tagging or the nature of the PF adhesive polymerizing differently next to the cell wall substance. The same trend was found in the EDS and XFM results, discussed next.

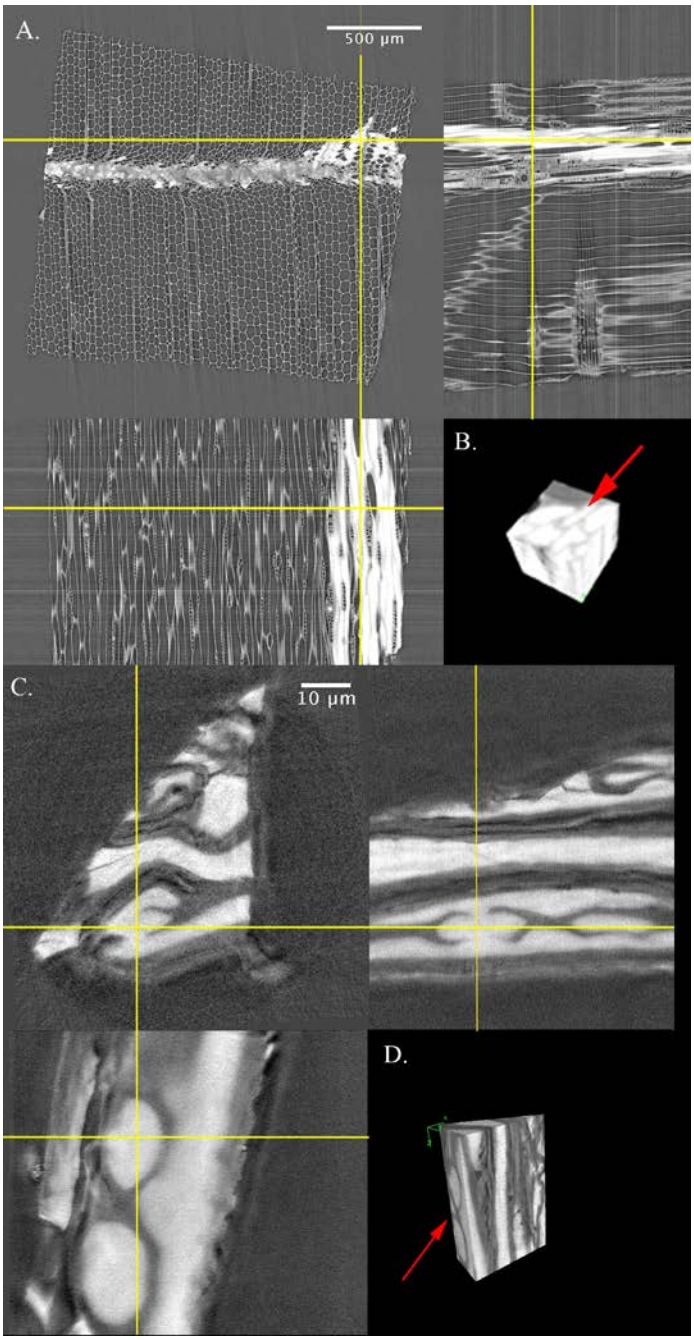

Figure 64. Locating nano-XCT specimen EE-IPL-3-I within the micro-XCT dataset; A.) original micro-XCT dataset with cross-hairs and orthogonal views showing location of nano-XCT sample; B.) 3D view of location within micro-XCT dataset with arrow emphasizing the elongated, crushed, EW cell in nano-XCT sample; C.) nano-XCT sample with orthogonal views showing bordered pits filled with adhesive; D.) 3D view of nano-XCT sample with arrow emphasizing bordered pits; right corner of 3D view shows crushed ray lumens.

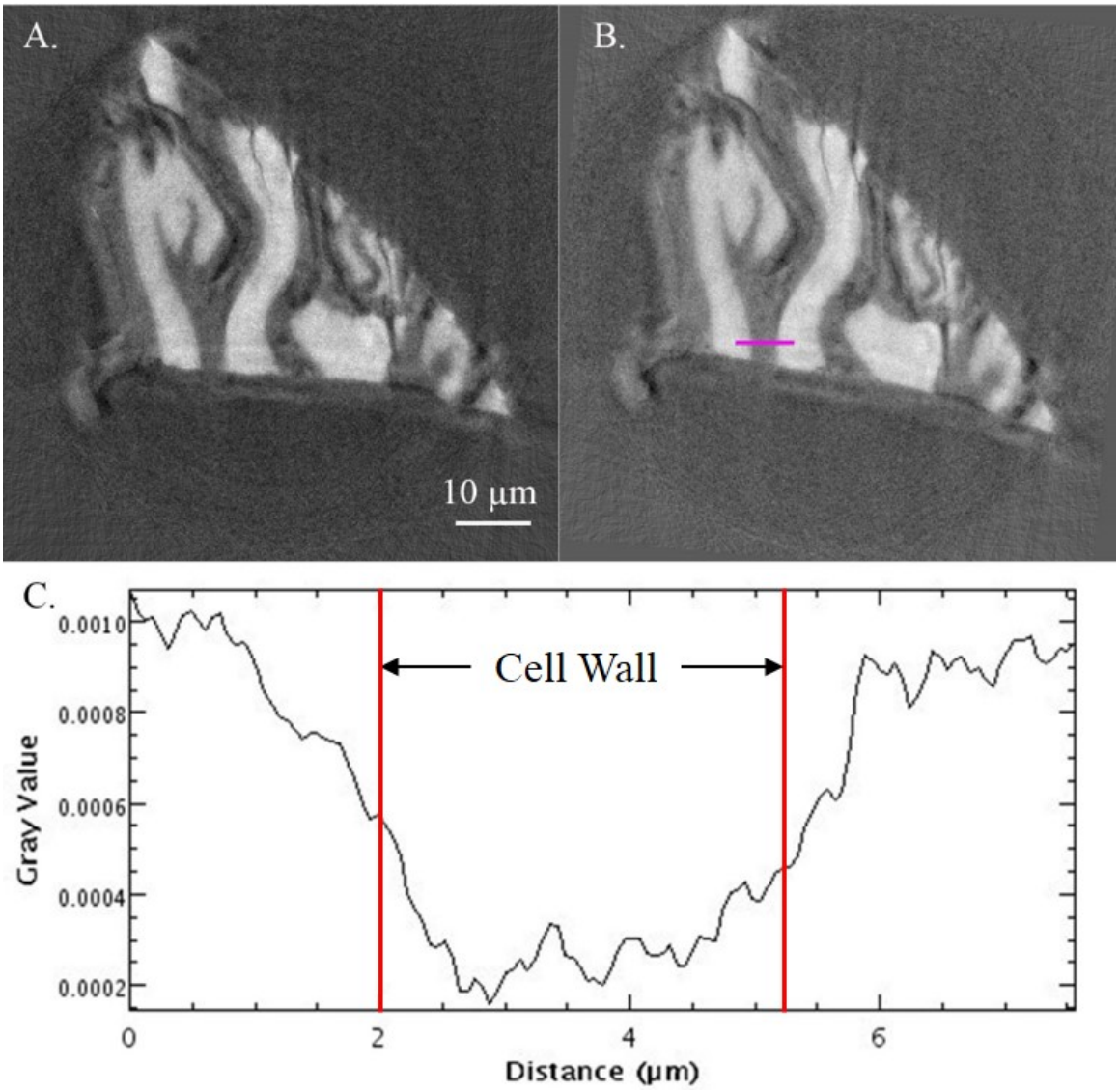

Figure 65. Adhesive penetration analysis of nano-XCT sample EE-IPL-3-I; A.) original nano-XCT slice; B.) slice after rotating CW 5º relative to slice in A; pink line indicates box scan (averaging values over 5 pixel height); C.) grayscale box analysis across pink line in B; red lines represent location of cell wall edges.

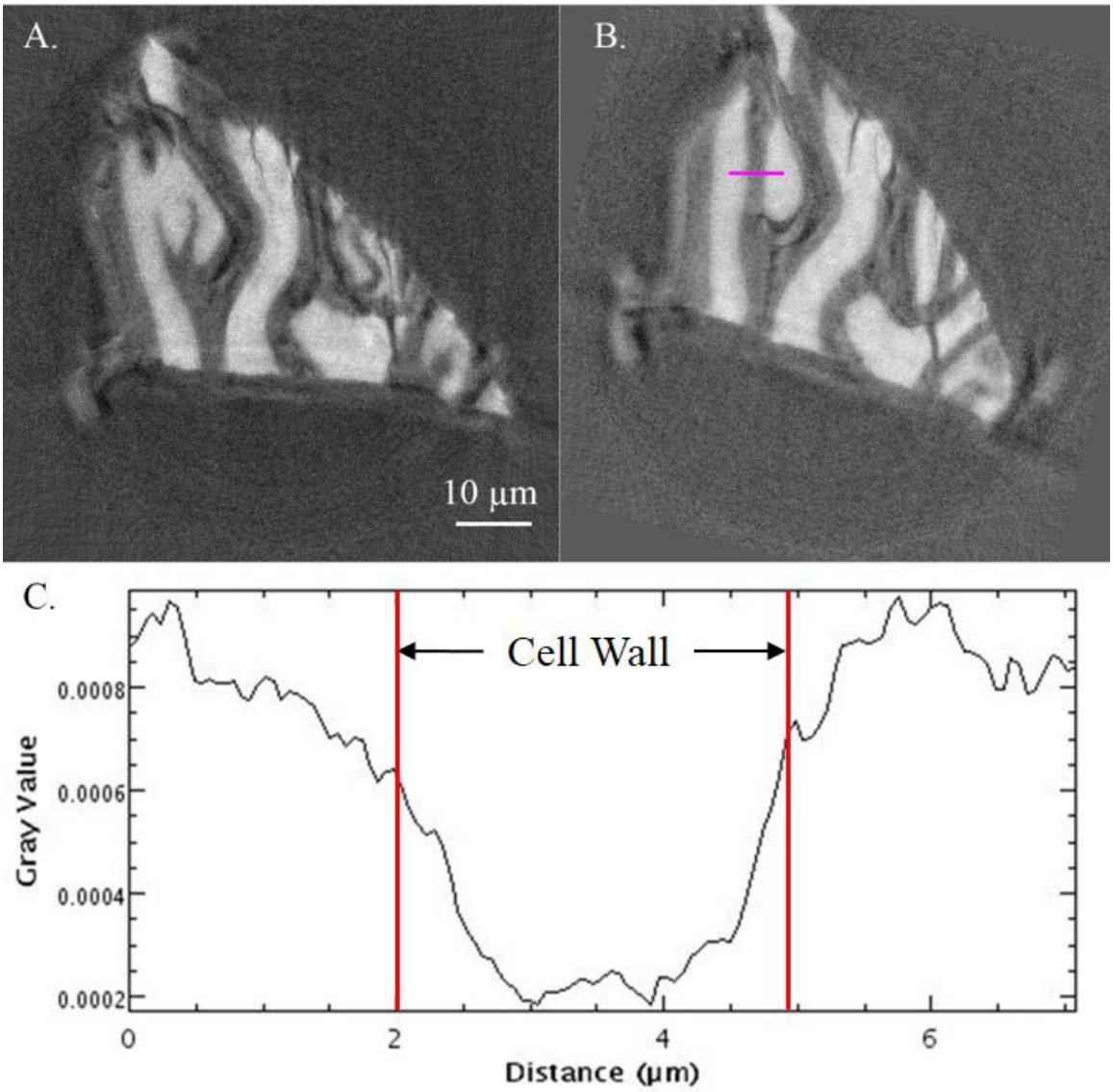

Figure 66. Adhesive penetration analysis of nano-XCT sample EE-IPL-DF-3-I; A.) original nano-XCT slice; B.) slice after rotating CW 14^{o} relative to slice in A; pink line indicates box scan (averaging values over 5 pixel height); C.) grayscale box analysis across pink line in B; red lines represent location of cell wall edges.

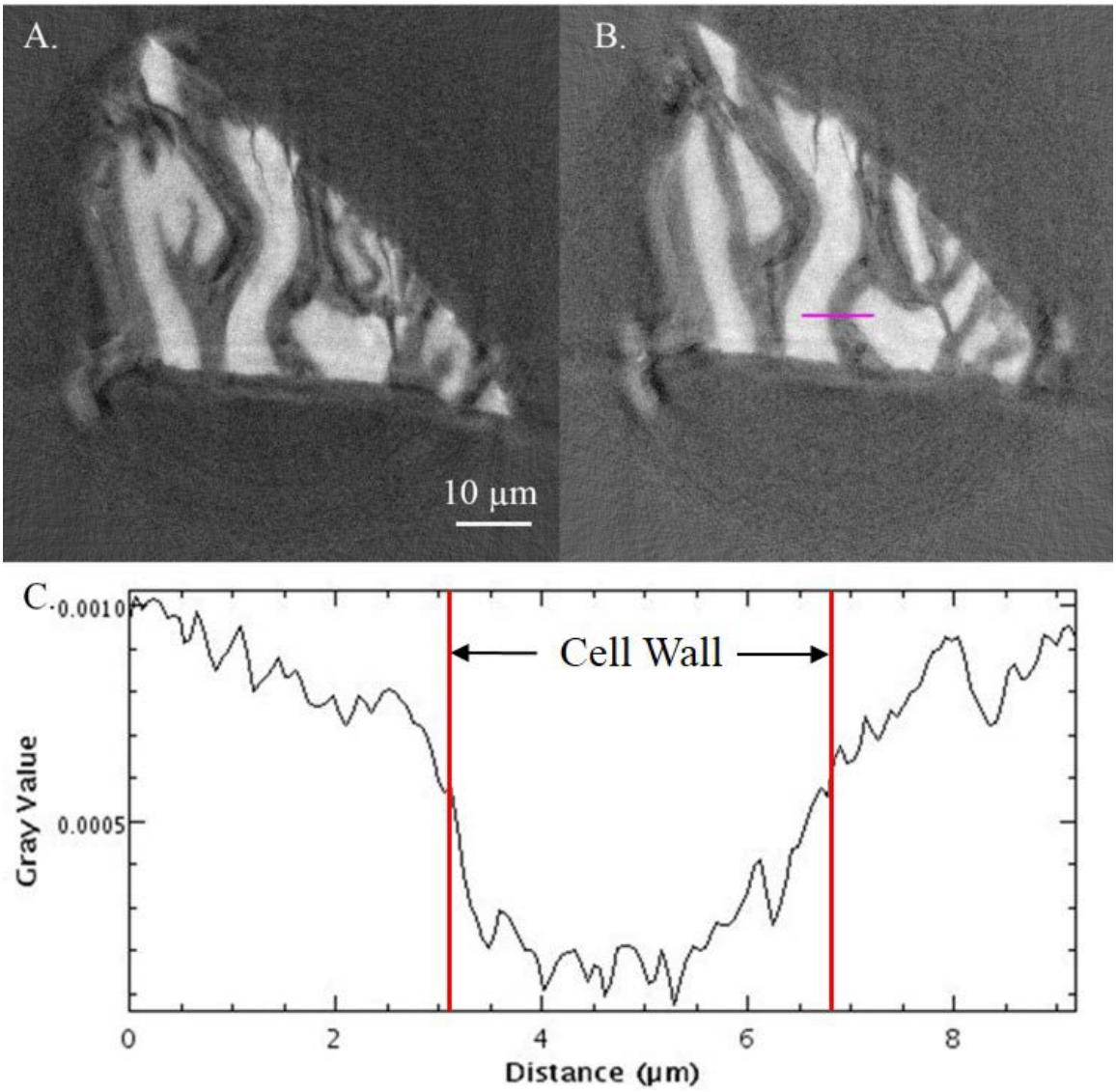

Figure 67. Adhesive penetration analysis of nano-XCT sample EE-IPL-DF-3-I; A.) original nano-XCT slice; B.) grayscale slice with pink line indicating box scan (averaging values over 5 pixel height); C.) grayscale box analysis across pink line in B; red lines represent location of cell wall edges.

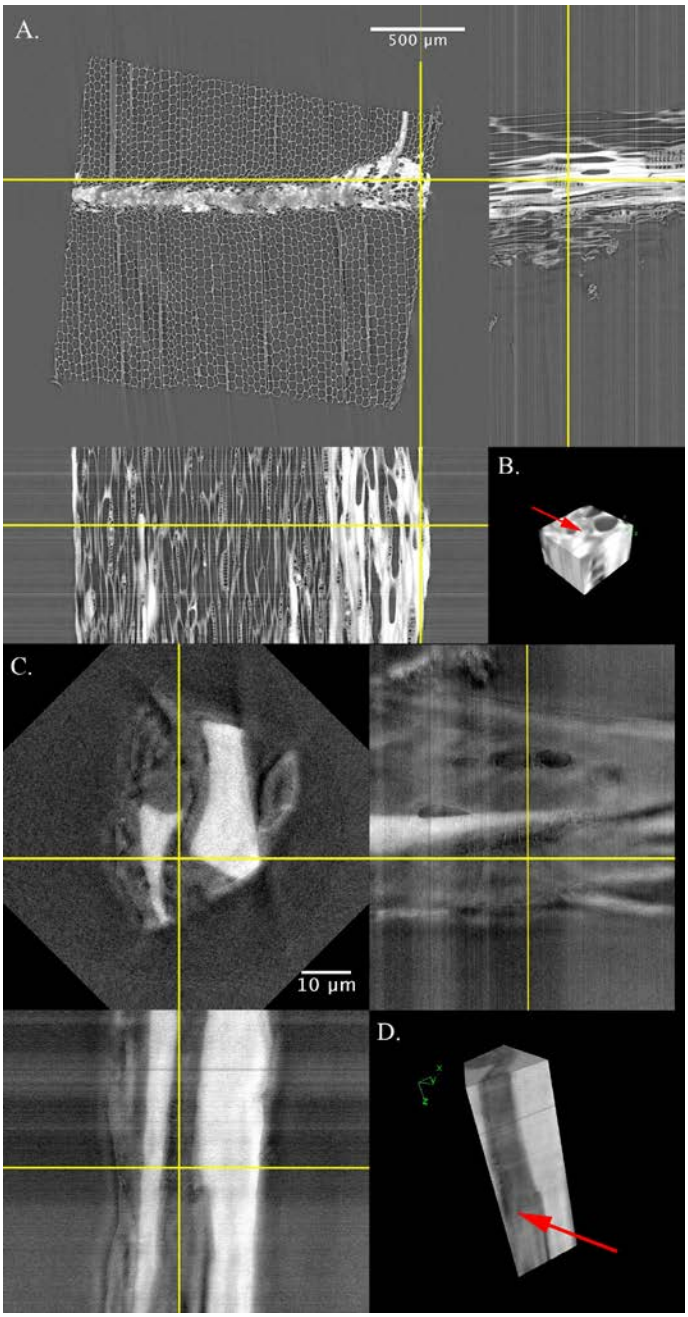

Figure 68. Locating nano-XCT specimen EE-IPL-DF-3-J within the micro-XCT dataset; A.) original micro-XCT dataset with cross-hairs and orthogonal views showing location of nano-XCT sample; B.) 3D view of location within micro-XCT dataset with arrow emphasizing the crushed ray in nano-XCT sample (Figure 69); C.) nano-XCT sample rotated CW 315° with orthogonal views showing voids in crushed ray and complex microstructure of the cell wall; D.) 3D view of nano-XCT sample with arrow emphasizing ray pitting on side of crushed ray (Figure 69).

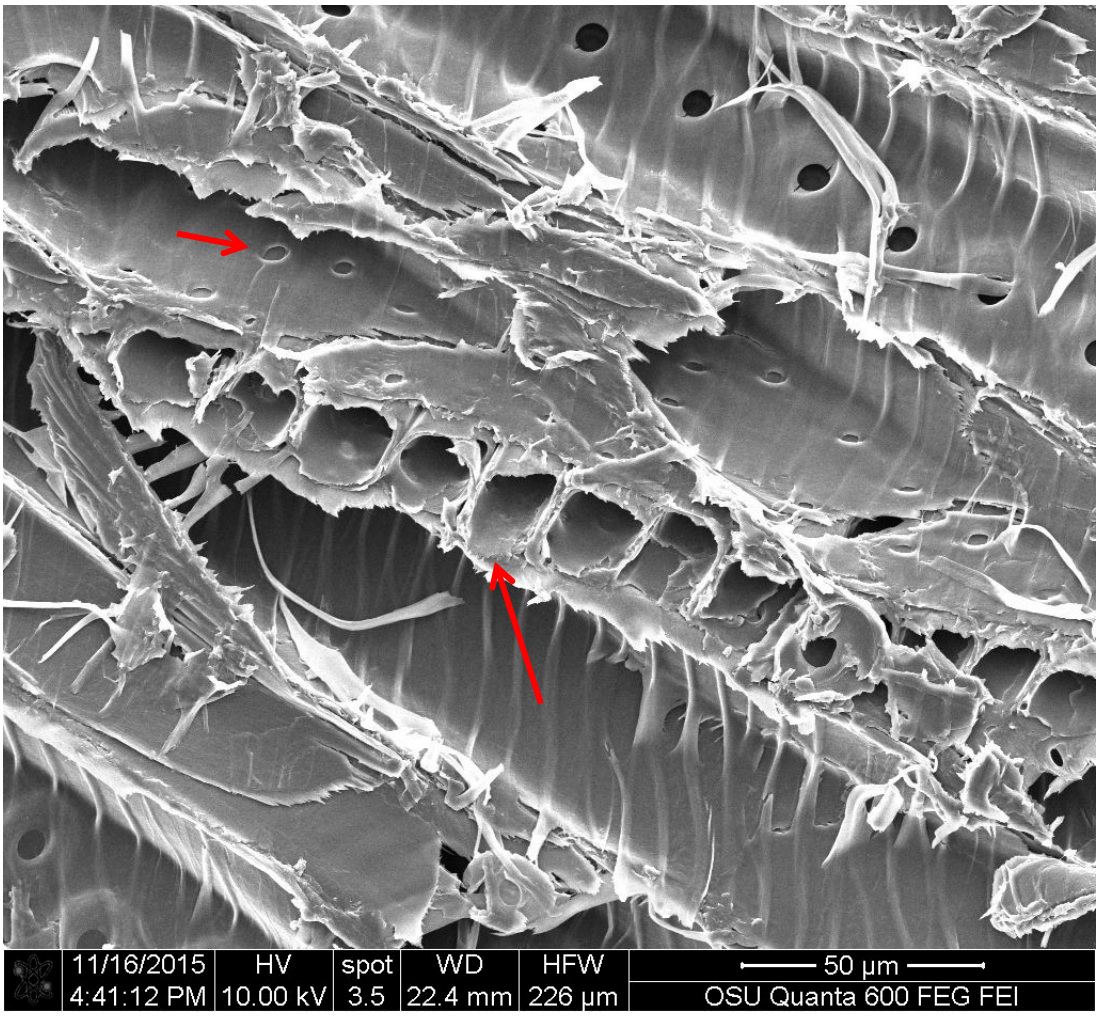

Figure 69. SEM showing ends of rays with ray pitting in Douglas-fir; used to identify and measure features within the nano-XCT dataset in Figure 68, although from the same piece of wood, this is not the same specimen as in Figure 68.

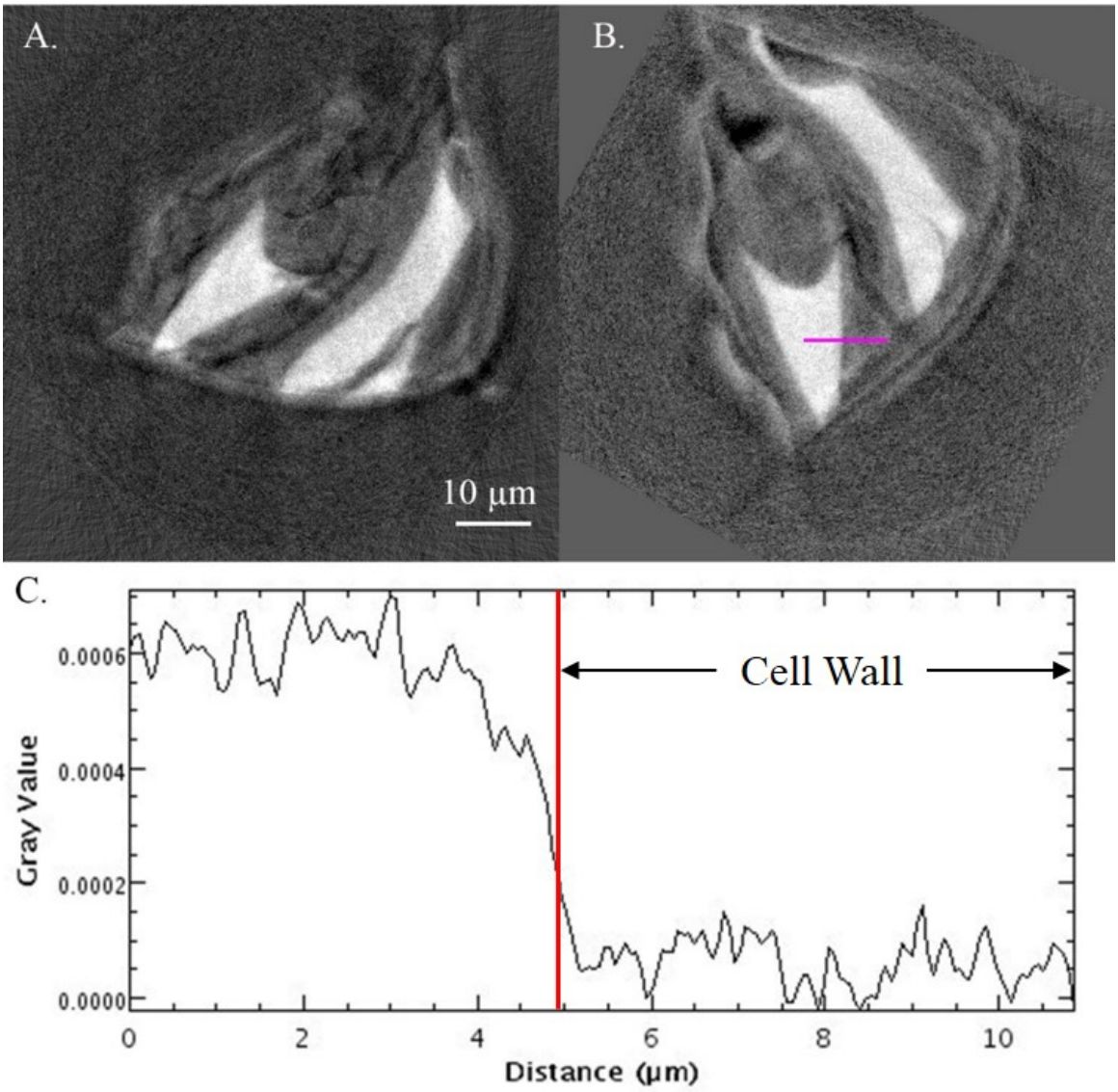

Figure 70. Adhesive penetration analysis of nano-XCT sample EE-IPL-DF-3-I; A.) original nano-XCT slice; B.) slice after rotating CW 298º relative to slice in A; pink line indicates box scan (averaging values over 5 pixel height); C.) grayscale box analysis across pink line in B; red lines represent location of cell wall edges.

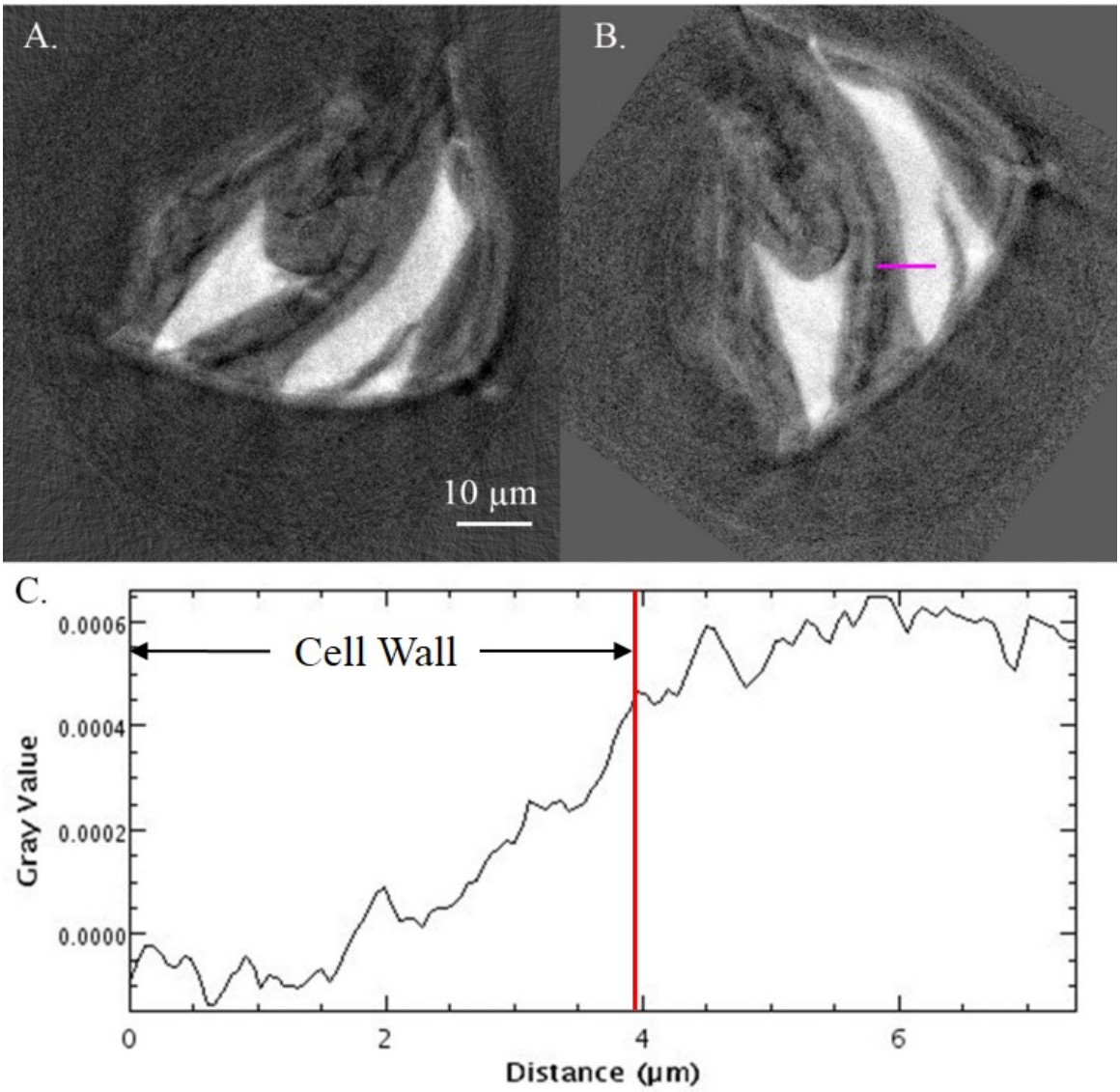

Figure 71. Adhesive penetration analysis of nano-XCT sample EE-IPL-DF-3-I; A.) original nano-XCT slice; B.) slice after rotating CW 306º relative to slice in A; pink line indicates box scan (averaging values over 5 pixel height); C.) grayscale box analysis across pink line in B; red lines represent location of cell wall edges.

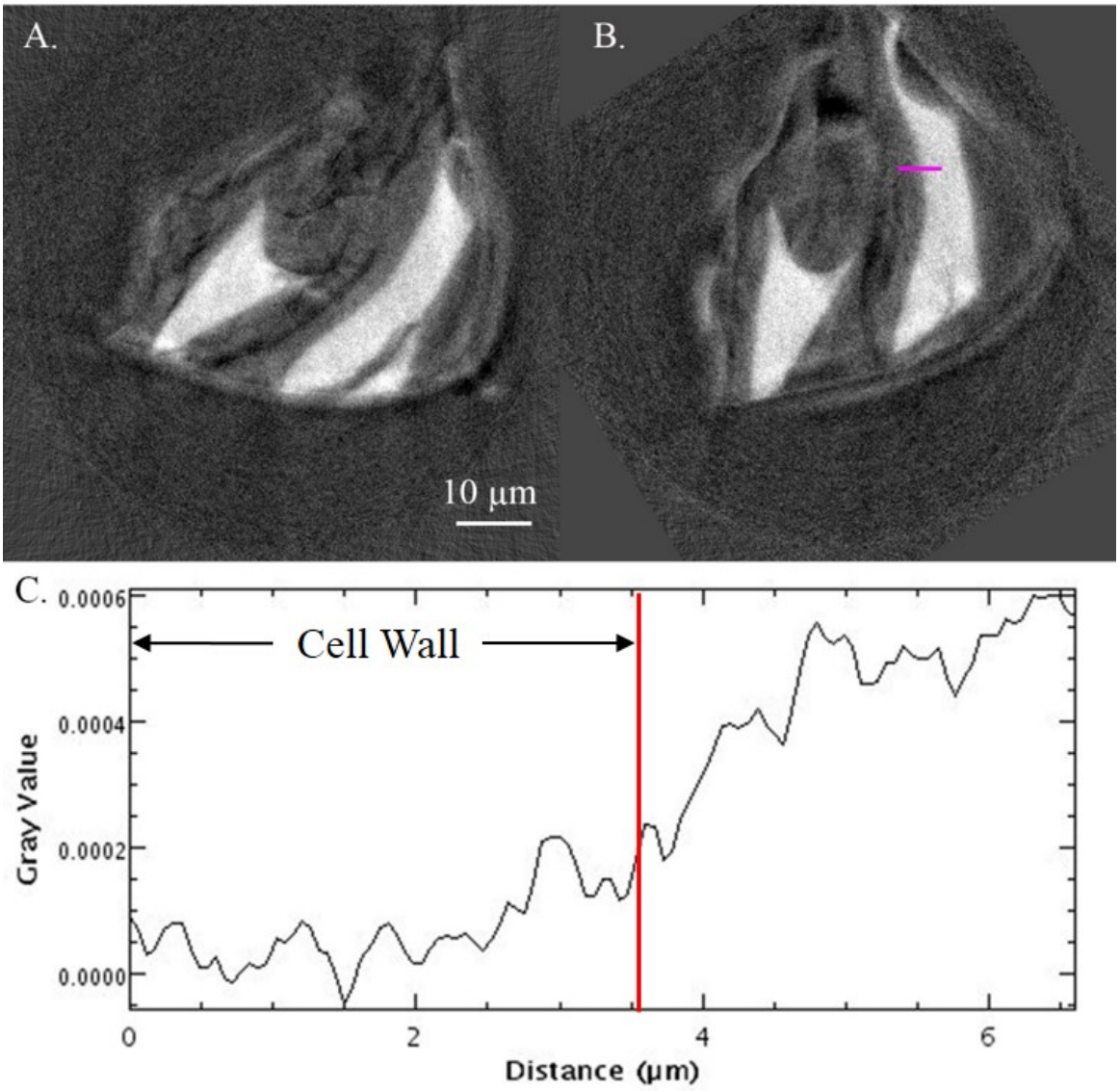

Figure 72. Adhesive penetration analysis of nano-XCT sample EE-IPL-DF-3-I; A.) original nano-XCT slice; B.) slice after rotating CW 328º relative to slice in A; pink line indicates box scan (averaging values over 5 pixel height); C.) grayscale box analysis across pink line in B; red lines represent location of cell wall edges.

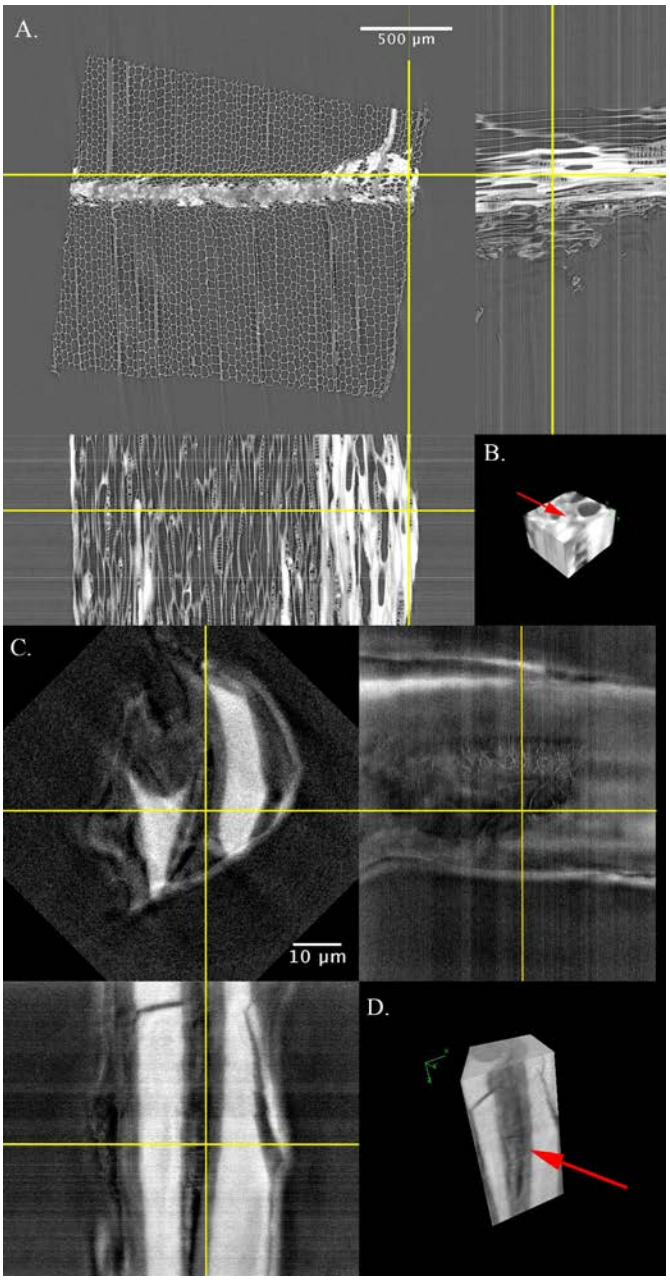

Figure 73. Locating nano-XCT specimen EE-IPL-DF-3-J within the micro-XCT dataset; this sample is located 40 microns above the nano-XCT sample in Figure 68; A.) original micro-XCT dataset with cross-hairs and orthogonal views showing location of nano-XCT sample; B.) 3D view of location within micro-XCT dataset with arrow emphasizing the crushed ray in nano-XCT sample (Figure 69); C.) nano-XCT sample rotated CW 315^{o} with orthogonal views showing voids in crushed ray and complex microstructure of the cell wall; D.) 3D view of nano-XCT sample with arrow emphasizing the end of crushed rays on side between two cell lumens filled with adhesive (Figure 69).

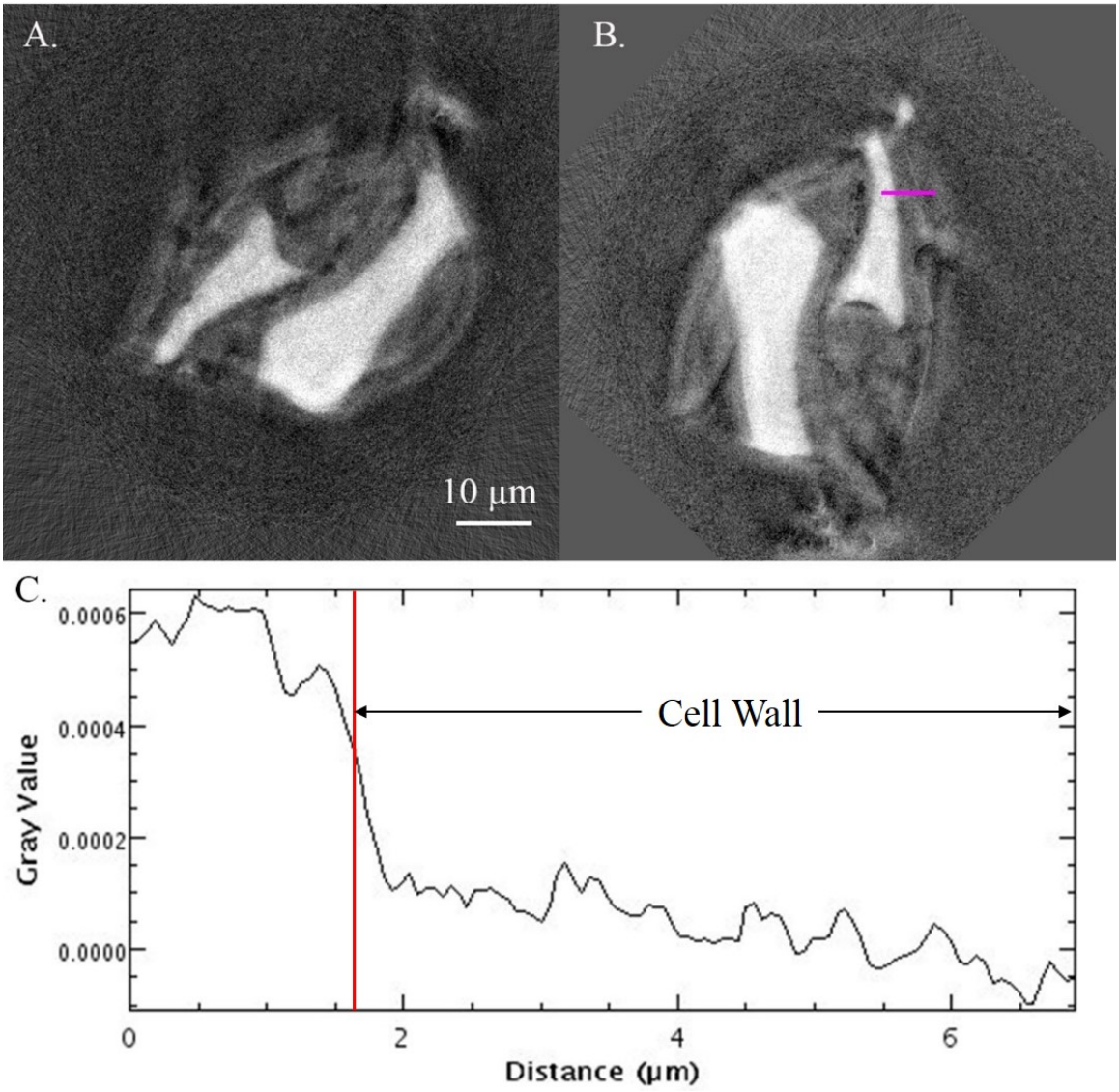

Figure 74. Adhesive penetration analysis of nano-XCT sample EE-IPL-DF-3-I; A.) original nano-XCT slice; B.) slice after rotating CW 135^{o} relative to slice in A; pink line indicates box scan (averaging values over 5 pixel height); C.) grayscale box analysis across pink line in B; red lines represent location of cell wall edges.

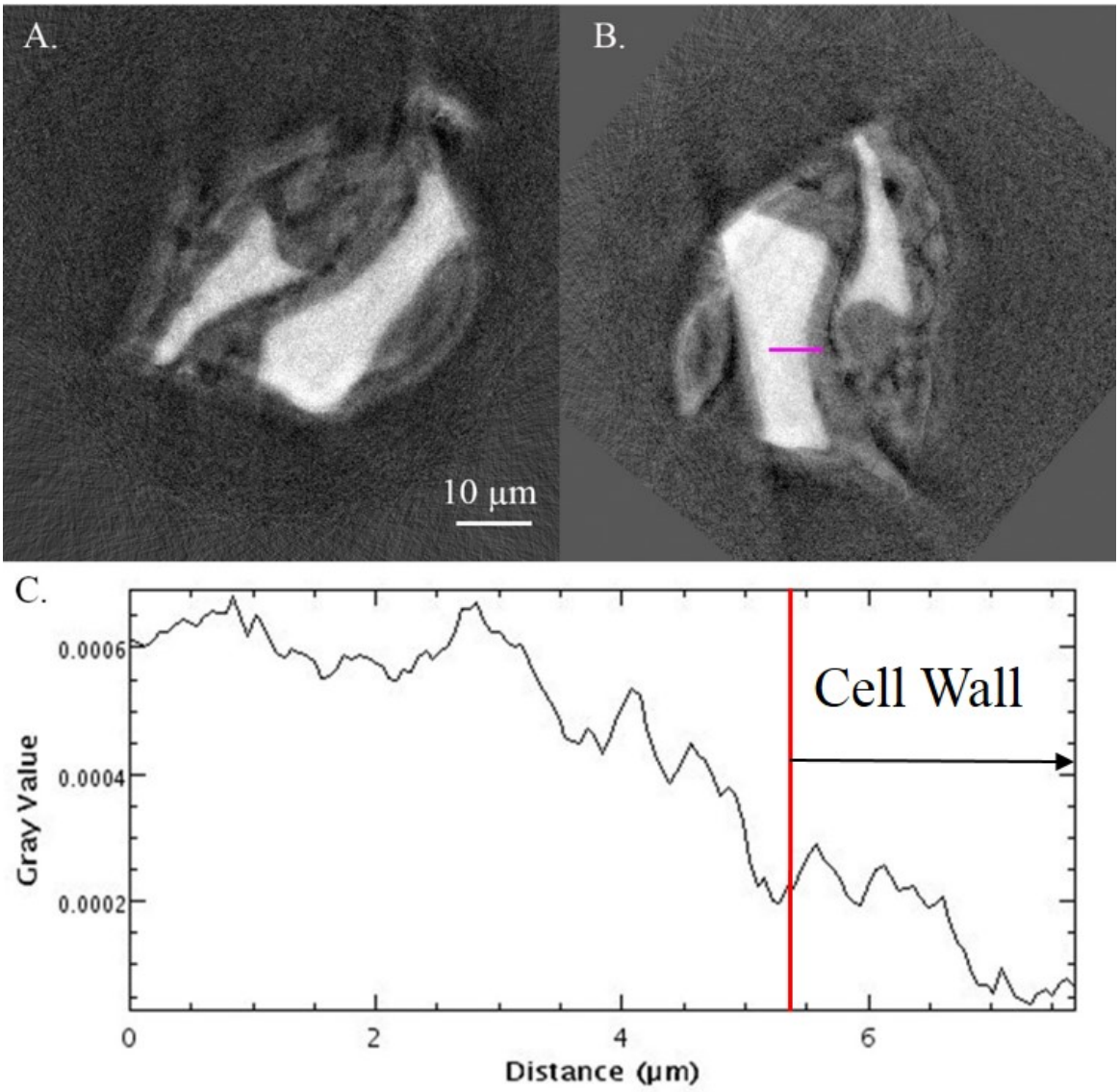

Figure 75. Adhesive penetration analysis of nano-XCT sample EE-IPL-DF-3-I; A.) original nano-XCT slice; B.) slice after rotating CW 130º relative to slice in A; pink line indicates box scan (averaging values over 5 pixel height); C.) grayscale box analysis across pink line in B; red lines represent location of cell wall edges.

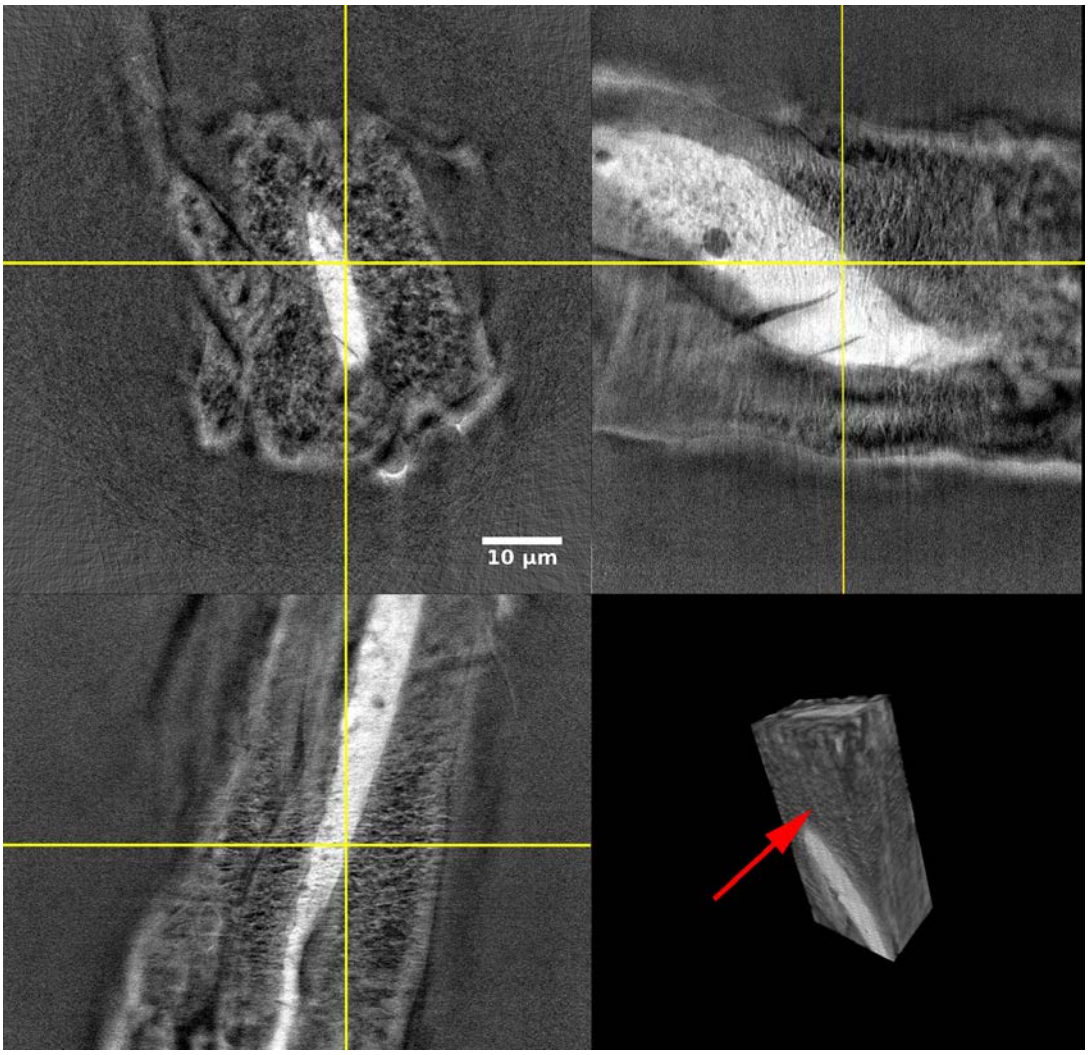

Figure 76. PAA treated nano-XCT sample from EE-IPL micro-XCT sample; orthogonal views and 3D view with arrow emphasizing porous cell wall structure; the variable x-ray attenuation values within the cell wall made adhesive penetration measurements more difficult, which was the opposite effect as anticipated.

4.4 Complementary Analysis

4.4.1 Energy Dispersive Spectroscopy

SEM was used to locate areas within the sample that have lumens filled with adhesive (Figure 77). EDS mapping was used to locate areas within the FOV that contain iodine. EDS line mapping was also used to represent differences in iodine net intensities from lumens filled with adhesive and into an adjacent cell wall.

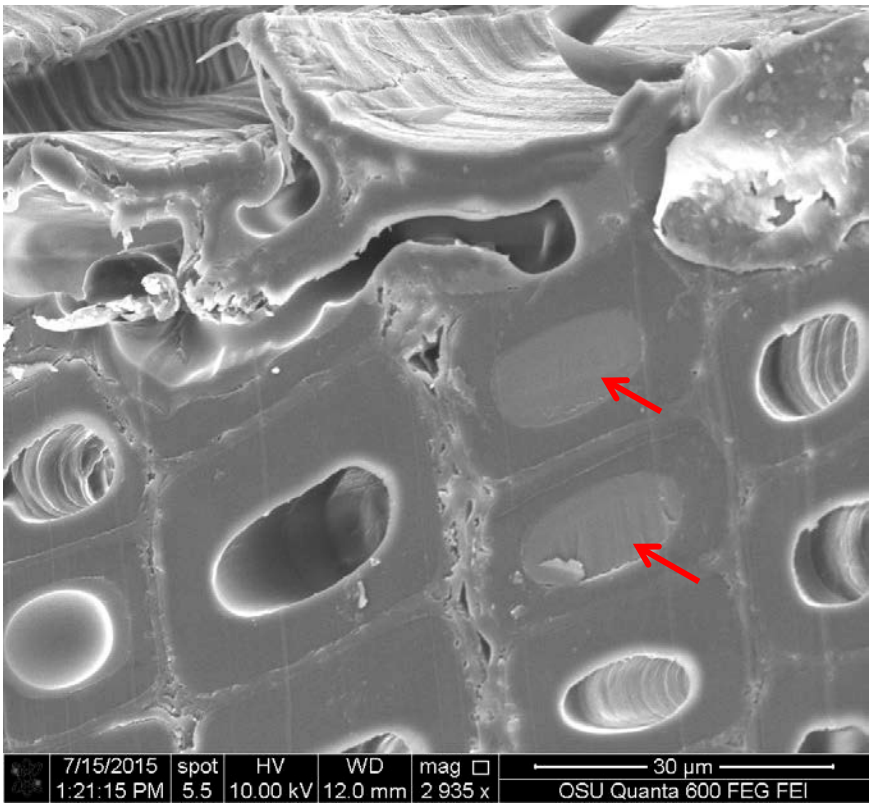

Figure 77. Example of SEM of IMDI sample with several lumens (arrows) filled with adhesive.

The EDS elemental maps showed areas that contained iodine, and therefore adhesive, confirming that the iodine was present in areas that contained adhesive. The elemental maps cannot be used to determine the concentration of adhesive in the cell wall. The net intensity measurement provides evidence of relative concentration of

iodine, and an approximate representation of concentration gradient in the cell wall. The EDS line scan data is shown in Figure 78 - Figure 81. This information can only be used as a qualitative measure and not as a quantitative measure of adhesive penetration. EDS does confirm the presence of iodine in the IMDI samples, making the lack of X-ray attenuation contrast more peculiar. If there was an issue during the tagging, and no iodine was present in the IMDI adhesive, the adhesive-filled lumens would not show the presence of iodine. In the case of IMDI, the concentration of iodine was not great enough to provide sufficient contrast by X-ray adsorption.

Figure 78 shows evidence of iodine in the cell wall, with penetration of approximately 500 nm to 800 nm. Figure 79 shows evidence of iodine in the cell wall, with penetration of approximately 2 μm (at right), but none in the adjacent cell wall at left. At the cell wall edge shown at left in Figure 79D, there is a void between the cured adhesive in the lumen and the cell wall. There also appears to be a gradient of iodine in the cured adhesive on the left, and some type of structure within the gradient region. Perhaps a fragment of the cell wall was torn away and overlapped the cured adhesive, which is an artifact from microtoming. This gradient within the pure IPL adhesive in the lumen was also present in the nano-XCT scans (Figure 65). EDS showed evidence of cell wall penetration for IPH (Figure 80) and IPL (Figure 81). Iodine was detected at approximately 500 nm penetration. Although, not all line scans revealed iodine in the cell wall adjacent to the adhesive-filled lumen (Figure 80D center). Again, these are speculations by the author and cannot be used as a comparison measurement to other penetration techniques.

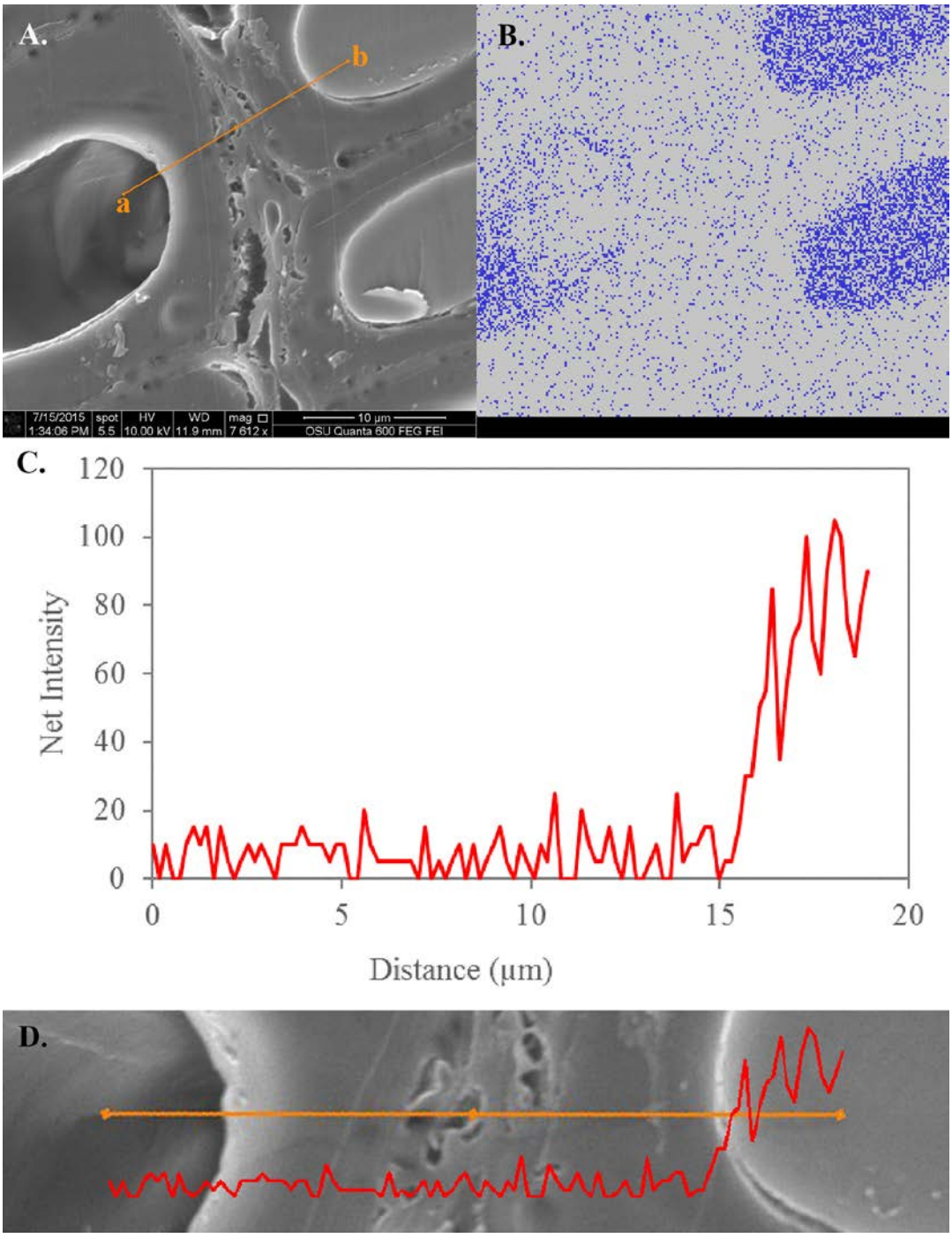

Figure 78. SEM and EDS of IMDI sample; A.) SEM with line scan starting at a and ending at b; B.) iodine elemental map of FOV in A; C.) net intensity of iodine from line scan in A; D.) net intensity overlay.

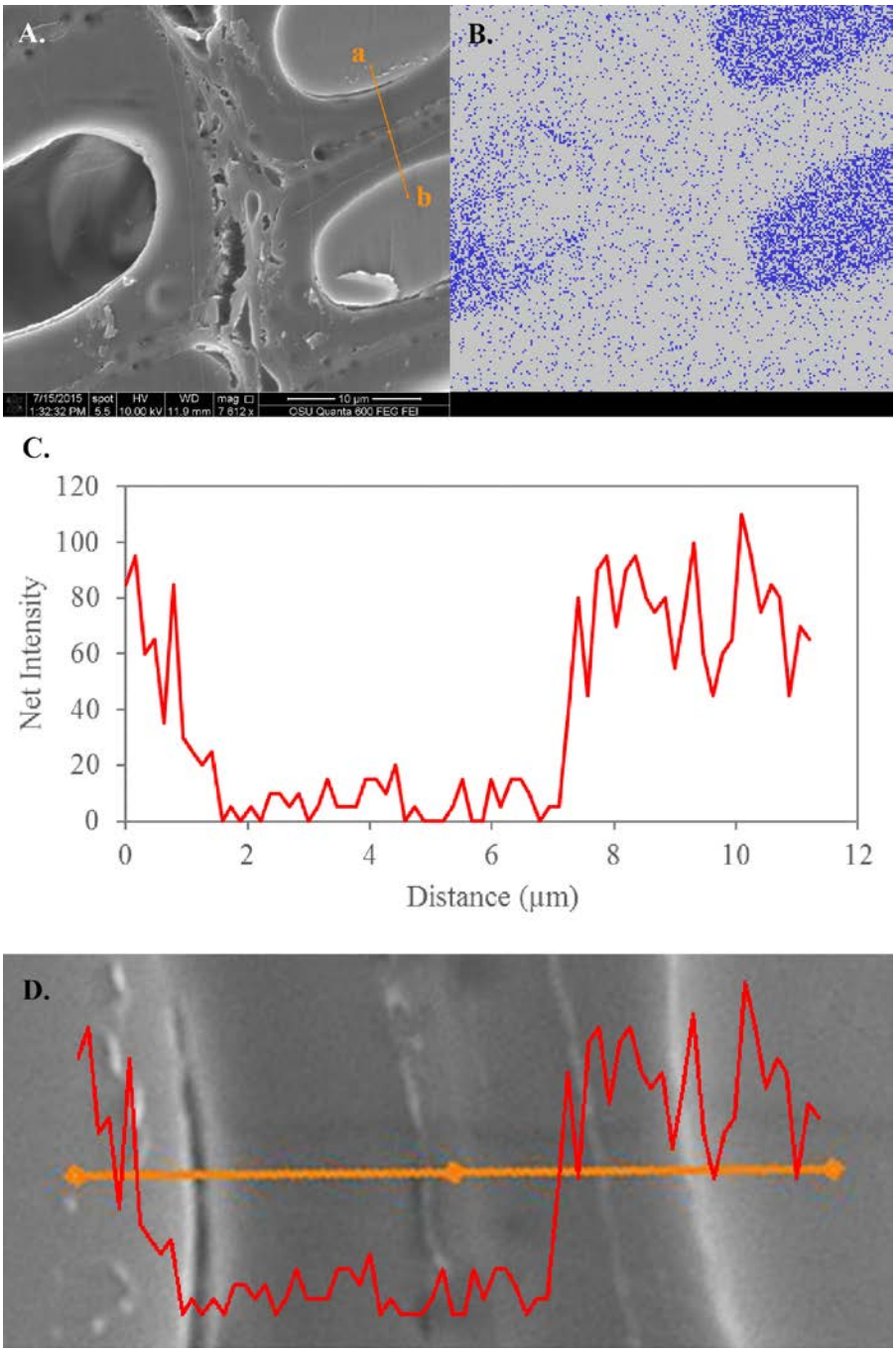

Figure 79. SEM and EDS of IMDI sample; A.) SEM with line scan starting at a and ending at b; B.) iodine elemental map of FOV in A; C.) net intensity of iodine from line scan in A; D.) net intensity overlay.

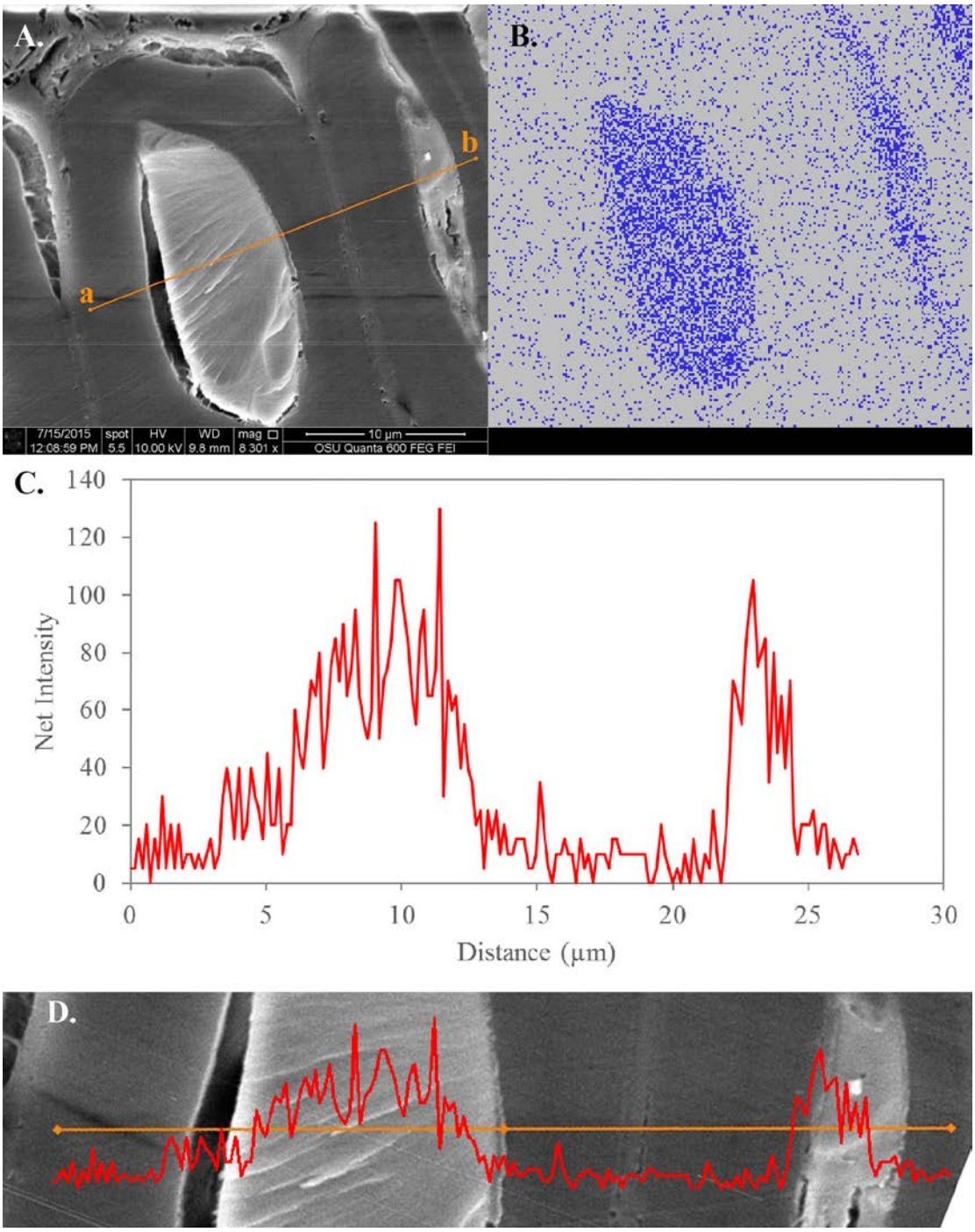

Figure 80. SEM and EDS of IPH sample; A.) SEM with line scan starting at a and ending at b; B.) iodine elemental map of FOV in A; C.) net intensity of iodine from line scan in A; D.) net intensity overlay.

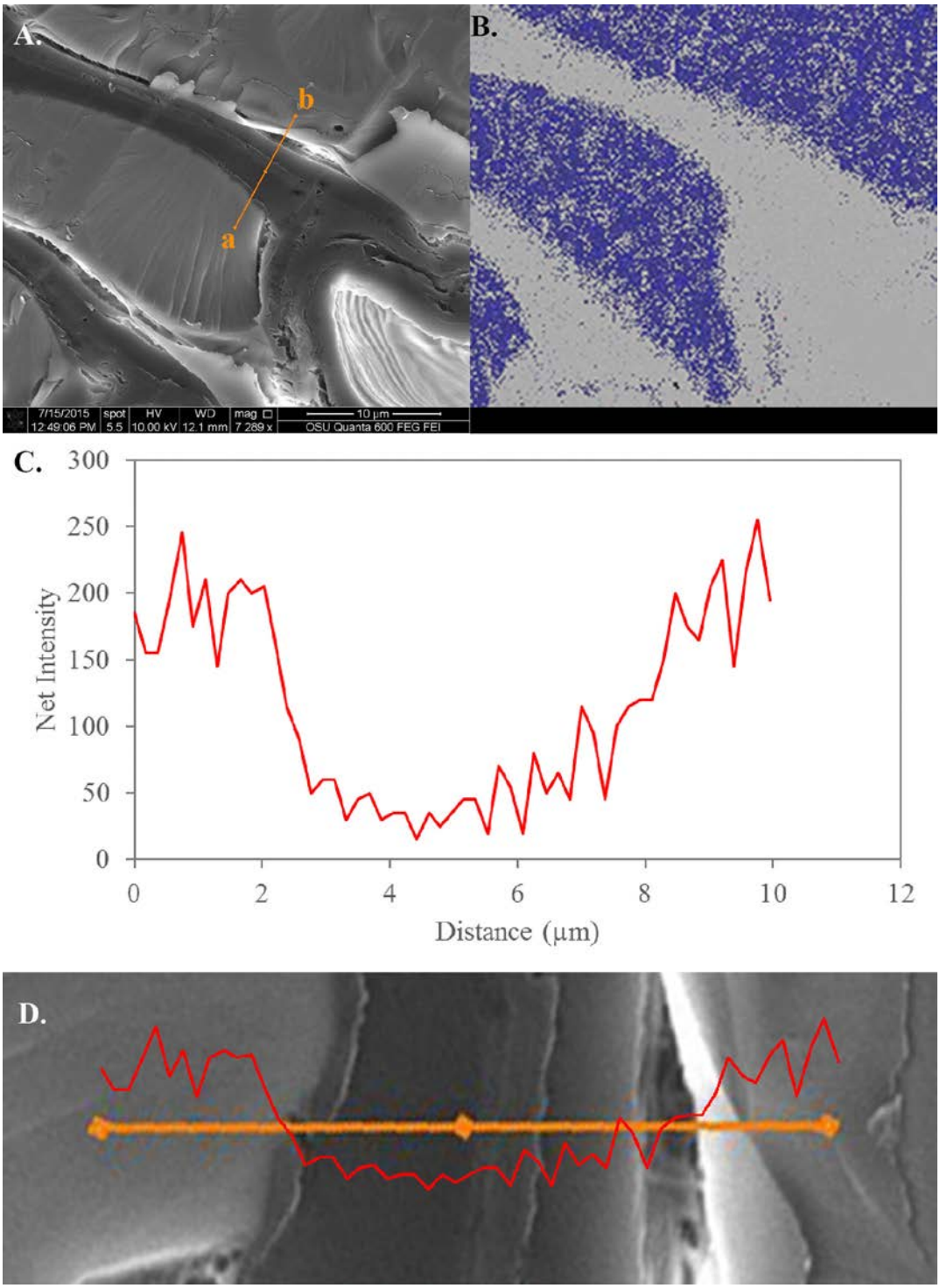

Figure 81. SEM and EDS of IPL sample; A.) SEM with line scan starting at a and ending at b; B.) iodine elemental map of FOV in A; C.) net intensity of iodine from line scan in A; D.) net intensity overlay.

4.4.2 X-ray Fluorescence Microscopy

The X-ray Fluorescence Microscopy (XFM) data gave quantitative information about the concentration of iodine in a sample. The XFM map represents the concentration of an element of interest as a grayscale value assigned to a pixel in a digital image, with color added to enhance visualization. Figure 82 - Figure 87 show the iodine elemental maps for IMDI and IPH, with box scan analyses. A box with a height of five pixels was used for the analysis, to reduce noise by averaging the grayscale value of the five pixels. The samples were rotated to create a perpendicular surface with respect to the direction of the box scan analysis. The difference between the relatively mobile IMDI in comparison to the high molecular weight IPH can be visualized in image A of each figure. Additional information is found in Appendix B. The CML in the region of the bondline had a slightly higher concentration of iodine than the rest of the cell wall substance. However, in relation to the concentration of iodine in the pure adhesive within the cell lumen, the iodine detected in the CML is low in concentration. The maximum concentration of iodine detected by XFM in the IMDI and IPH was 91 and 289 $\mu g/cm^3$, respectively. The lower concentration of iodine in the IMDI perhaps explains why the x-ray absorption contrast was poor. The iodine tagging procedure for the IMDI was intended to create the same concentration as the IPL and IPH adhesives. Apparently an error occurred. The resolution of the XFM elemental analysis was 0.2-0.3 μm^2/pixel, which is lower than the nano-XCT analysis, which was 0.06 μm^2/pixel. Nevertheless, XFM could still resolve the presence of adhesive penetration into the cell wall for the IMDI and IPH samples.

Based on the presence of iodine in the cell walls near the bondline of the IPH samples, it appears there is adhesive penetration into the cell substance (Figure 82 -

Figure 85). The IMDI samples have iodine present farther away from the bondline, due to the highly mobile nature of IMDI (Figure 86 - Figure 87) compared to IPH. When compared to the nano-XCT data from the IPL samples, there is a sharper phase change from an adhesive-filled lumen to an adjacent cell wall in the IPH samples, although these techniques had different spatial resolutions and different detection limits. Both adhesives appear to migrate more readily through the CML. XFM detected IPH completely through the cell walls adjacent to adhesive-filled lumens and a penetration depth of about 1 µm into the cell wall. XFM detected deep penetration of IMDI through the CML, more than 10 cells away from the bonded interface (Figure 86). However, little IMDI was detected in the cell walls (< 1 µm). An interesting phenomena occurred in some of the penetration analysis showing a decrease in iodine towards the center of an adhesive-filled lumen. This is seen in the nano-XCT dataset in Figure 66 and also in the XFM datasets in Figure 84 and Figure 96 in Appendix B. This could be due to a difference in polymerization of the adhesive near the cell wall substance, although it was not seen in all of the samples.

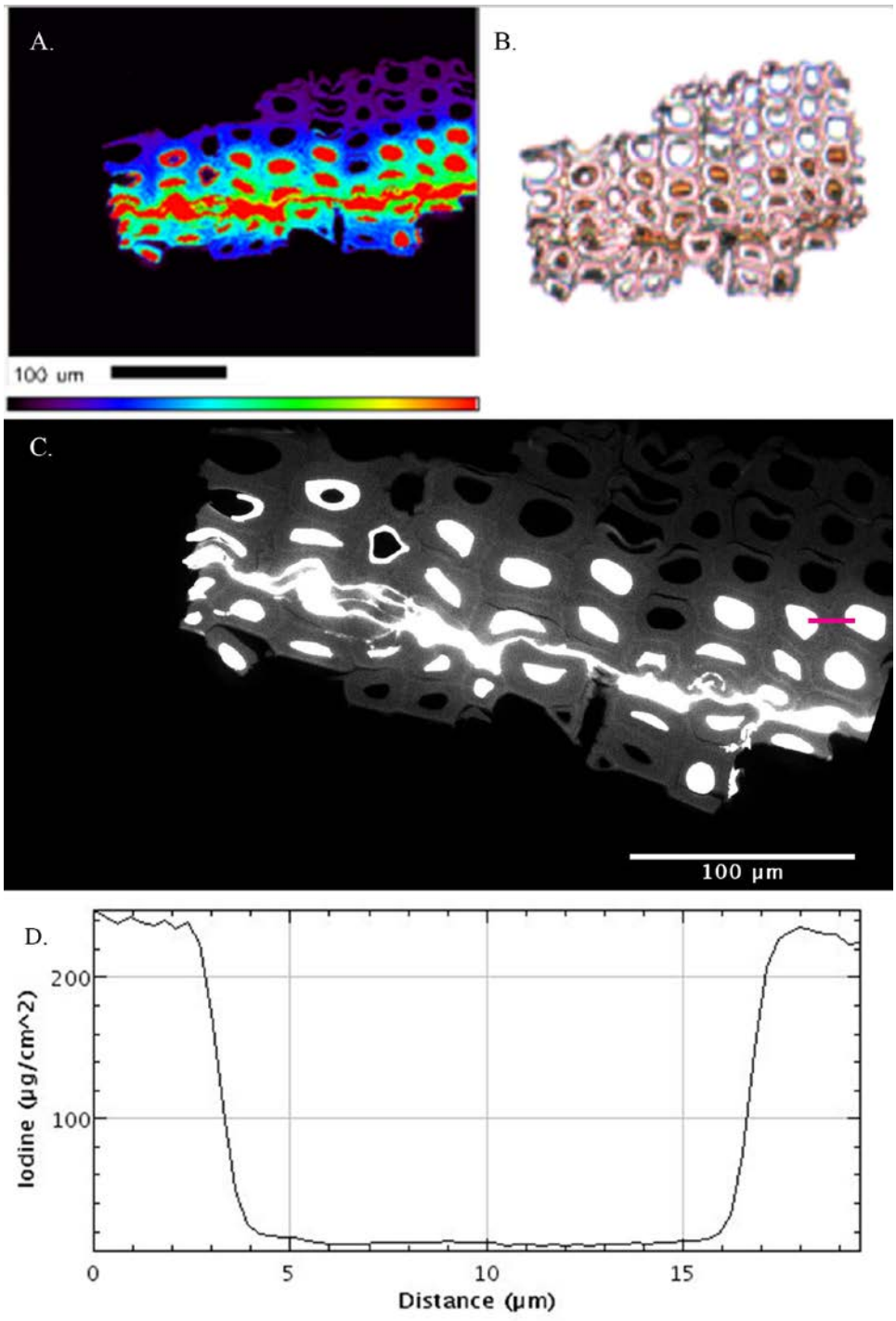

Figure 82. XFM of IPH; A.) Color mapped section of iodine with bondline near bottom; B.) Original 2 µm thick slice with bondline located near the bottom of the slice; C.) grayscale slice after rotating CW 18^{o} relative to image A; pink line indicates box scan; D.) distribution of iodine across line.

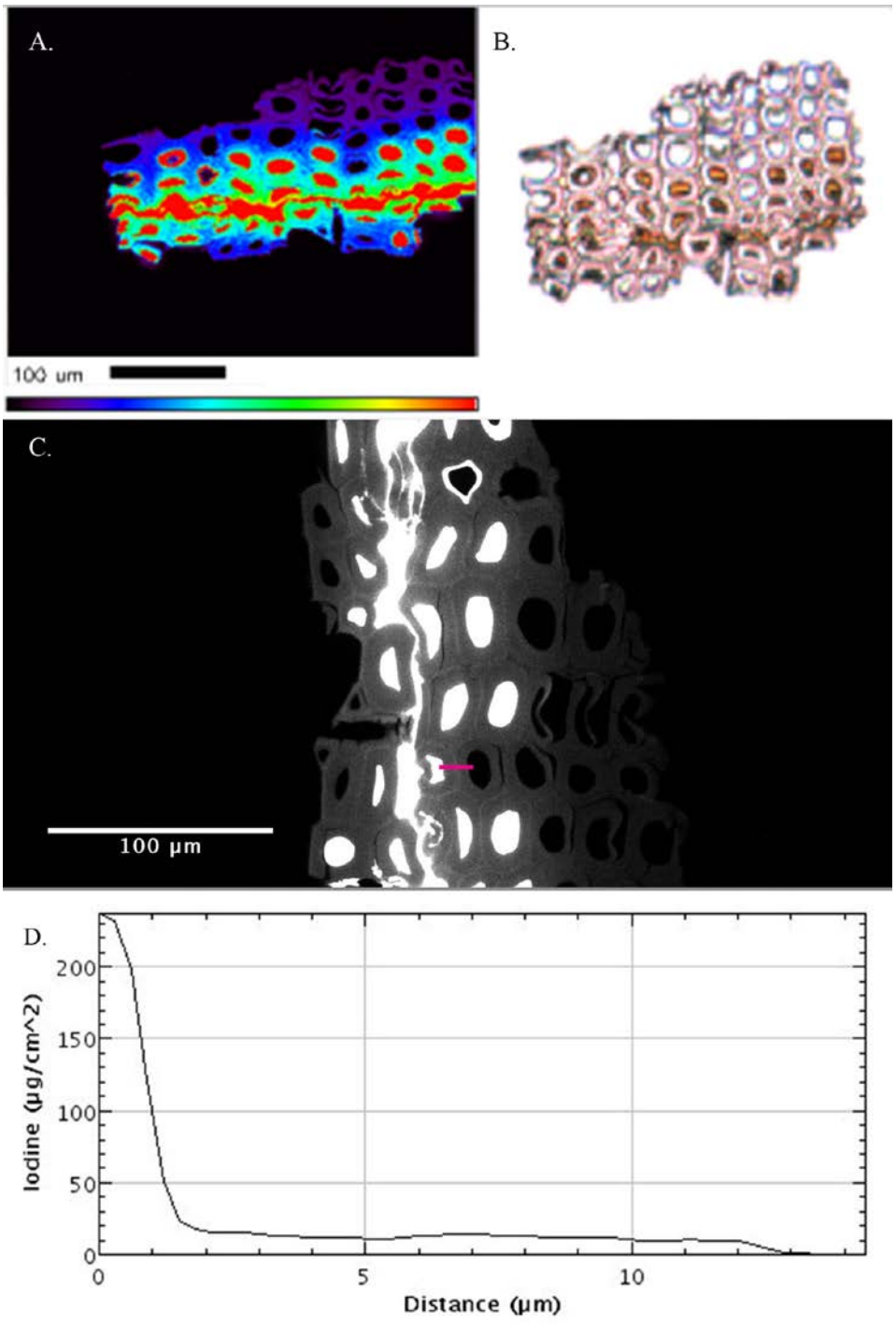

Figure 83. XFM of IPH; A.) Color mapped section of iodine with bondline near bottom; B.) Original 2 µm thick slice with bondline located near the bottom of the slice; C.) grayscale slice after rotating CW 90° relative to image A; pink line indicates line scan; D.) distribution of iodine across line.

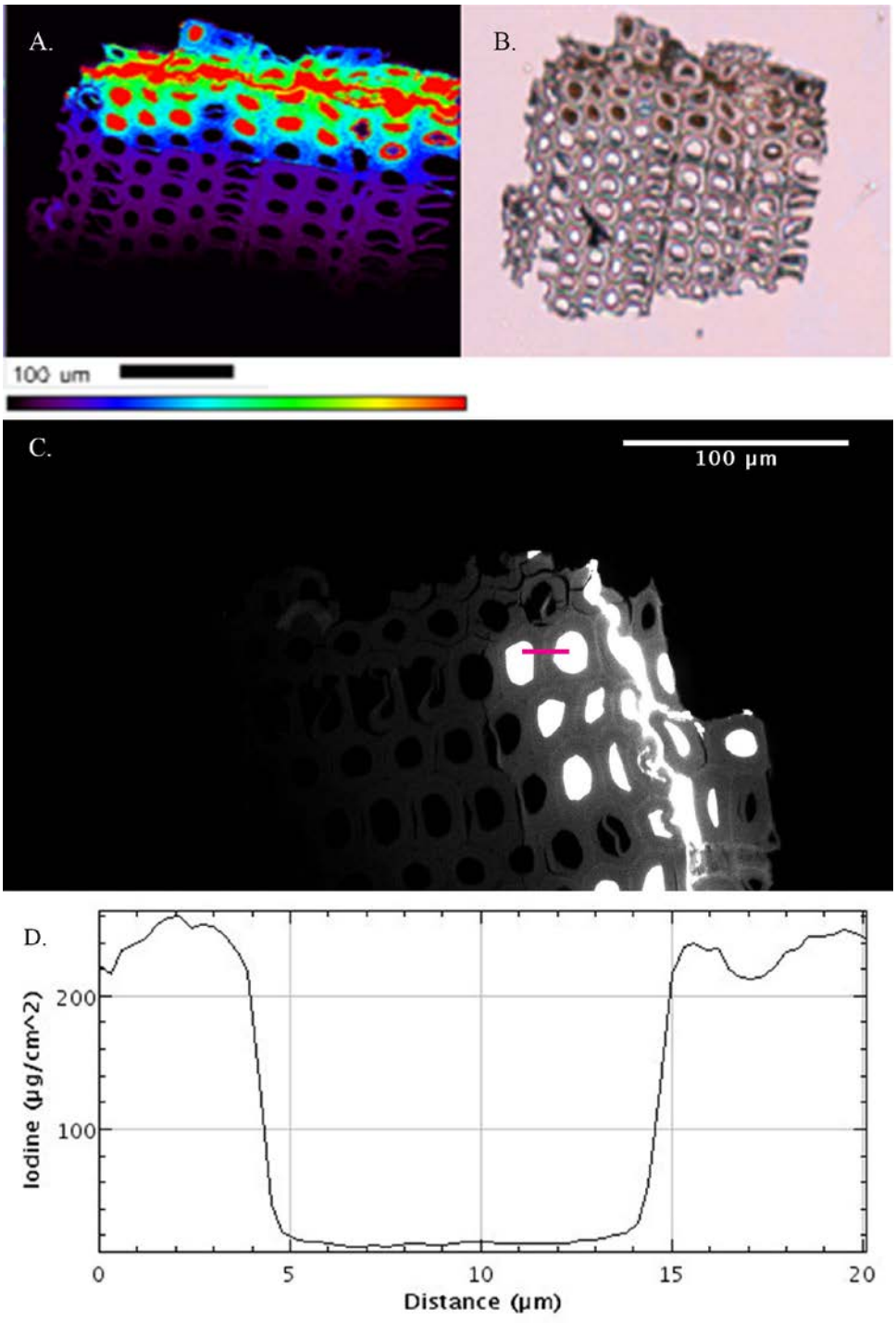

Figure 84. XFM of IPH; A.) Color mapped section of iodine with bondline at top; B.) Original 2 µm thick slice with bondline located near the bottom of the slice; C.) grayscale slice after rotating CW 68 ^{o} relative to image A; pink line indicates line scan; D.) distribution of iodine across line.

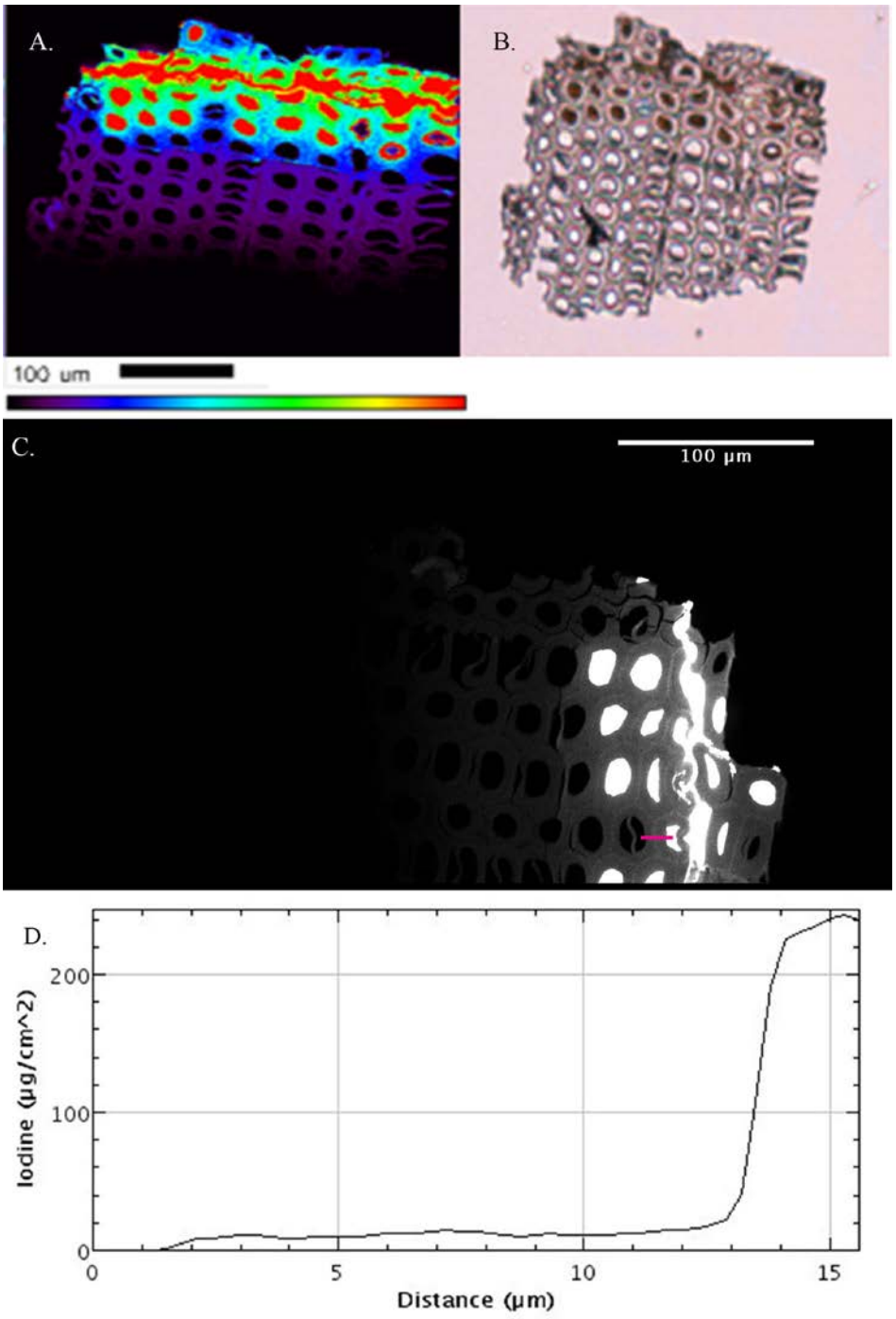

Figure 85. XFM of IPH; A.) Color mapped section of iodine with bondline at top; B.) Original 2 µm thick slice with bondline located near the bottom of the slice; C.) grayscale slice after rotating CW 86 º relative to image A; pink line indicates line scan; D.) distribution of iodine across line.

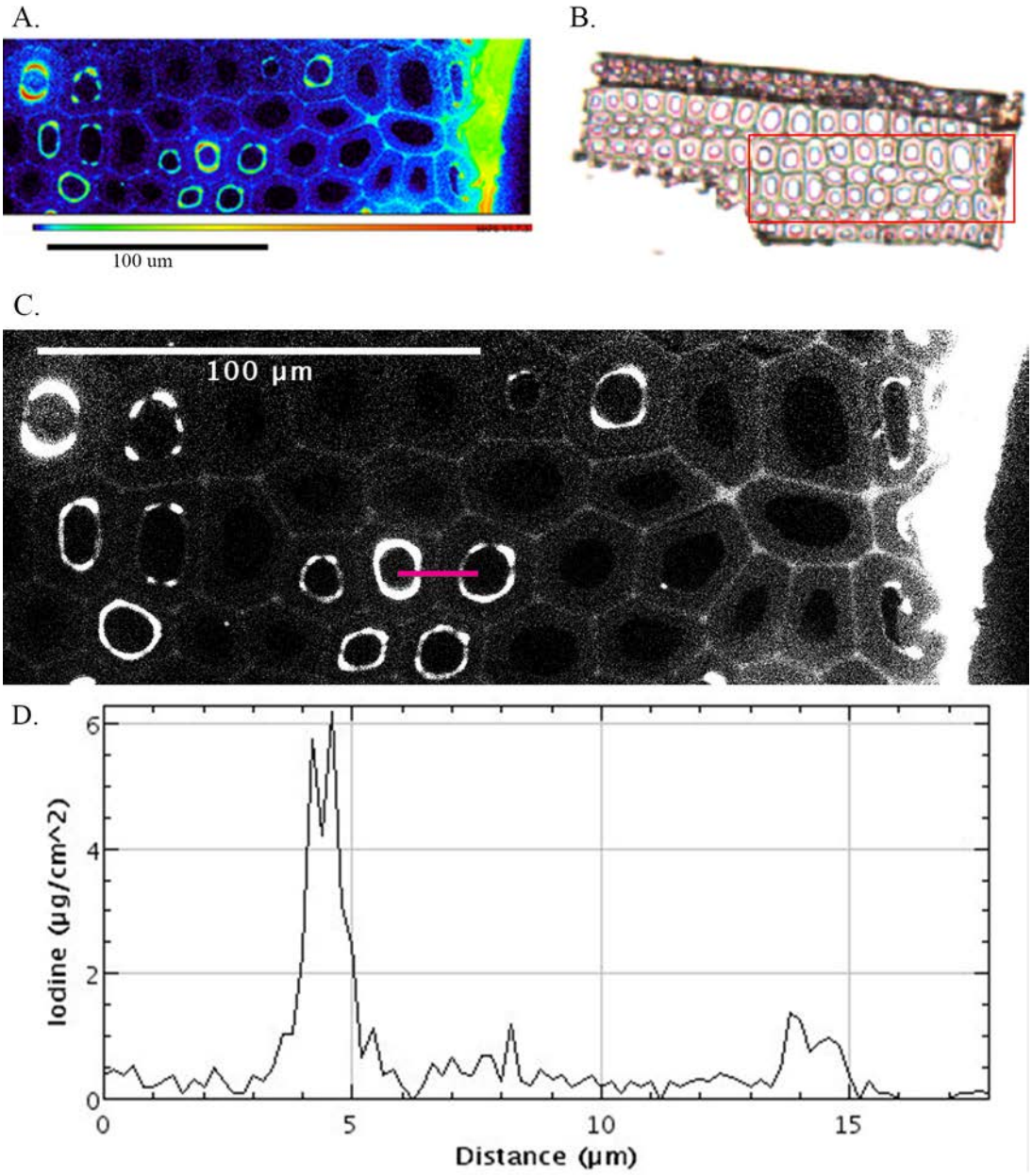

Figure 86. XFM of IMDI; A.) Color mapped section of iodine with bondline located on right; B.) Original 2 µm thick slice with bondline located near the bottom of the slice; C.) grayscale slice; pink line indicates line scan; D.) distribution of iodine across line.

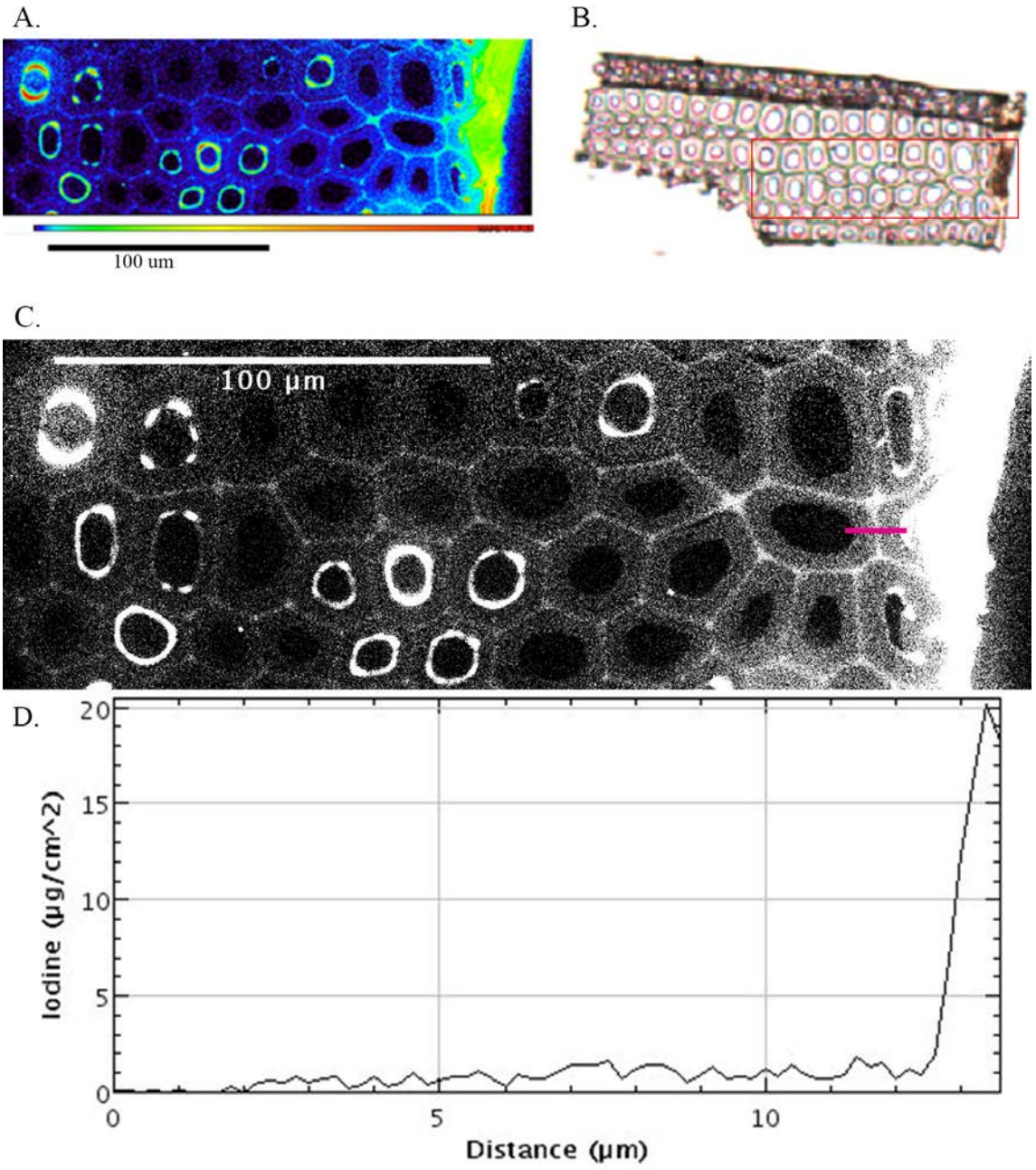

Figure 87. XFM of IMDI; A.) Color mapped section of iodine with bondline on right; B.) Original 2 µm thick slice with bondline located near the bottom of the slice; C.) grayscale slice; pink line indicates line scan; D.) distribution of iodine across line.

CHAPTER 5: SUMMARY

5.1 Conclusions

This project investigated the influence of adhesive penetration on the ability of adhesive bonds in Douglas-fir wood to resist the effects of moisture. Accelerated weathering procedures, mechanical testing, micro- and nano-XCT, and complementary elemental analysis techniques were used. Mechanical tests examined shear strain and ultimate strength. The extent of penetration analysis examined adhesive flow into the cell lumens and cell wall. Four adhesive formulations were examined in an attempt to create different penetration patterns into wood. Although the adhesive formulations were unique, they still provided a basis for relative comparison of main effects. High variability of the test results and small number of replications prevented definitive conclusions in several cases. While the APS is a renowned facility, the tomography tests were particularly challenging due to the limited access to the facilities, which prevented retesting of poor specimens within the time limitations of the study. In particular, the nano-XCT experiment was the first of its kind performed on wood adhesive bonds, and one of the first experiments performed on this facility at the APS. A final conclusion about the objective of this study was inconclusive. Nevertheless, this research revealed some interesting observations and opportunity for future work to build upon.

Information gathered from the lap-shear tests, tomography data, EDS, and XFM gave insight on how adhesive penetration affects the mechanical performance of the bondline, specifically related to weathering. Results from the lap-shear tests and DIC shear strain calculation showed high variation within sample groups. Differences were

seen between dry and macroweathered samples. The visual DIC surface shear strain maps showed a higher amount of shear strain, in general, for the IPH and IMDI samples, than the IPL and IPLFE samples when subjected to the same level of stress. However, this varied based on the bonded wood surface. The EL samples were more variable than the LL and EE samples. Discrepancies in sample quality and manufacturing factored into the variation in the results. EW/LW transition regions both within the DIC AOI and around the AOI caused variability.

Accelerated weathering tests are inherently difficult to quantitatively assess. In this research some macroweathering specimens did not survive the weathering procedure and could not be evaluated in the lap-shear apparatus. The five samples that delaminated during the weathering were first kept out of the statistical analysis, then added to an additional analysis. Even though these samples could not be mechanically tested, these samples were critically deteriorated by the weathering procedure. When the delaminated samples were added to the analysis, the EL-IMDI samples had a significant difference in the weathered vs. non-weathered samples for the effective shear modulus. In both sets of analyses, the EL-IPH samples had a significant difference in weathering for the effective shear modulus results. The energy to failure results did not show any significant differences for weathering, in any of the sample groups. Despite the delamination of five of the samples during the weathering cycles, the author suspects that the weathering regime needed to be more intense to see clear differences in the mechanical test results. The IPLFE and IPL samples did not have any significant differences after weathering, indicating that they perform similarly before and after weathering.

The failure modes for each sample were recorded and categorized based on the failure location related to the notches in the lap-shear specimens. In addition, the failed surfaces were evaluated for the percent wood failure. The LL-IPH samples did not have any of the non-weathered samples fail between the notches. These samples also had high maximum load values. None of the non-weathered LL-IPH specimens failed between the notches. It can be concluded that the LL-IPH specimens had very high apparent shear strength in the dry condition. If the IPH does not penetrate into the wood, but rather creates a thick bondline, this would explain a greater amount of brittle adhesive failure. The IMDI penetrates so well, that it leaves a thin film of adhesive at the failed interphase.

The microweathered XCT samples showed that the parallel-laminated samples had little to no internal cracking after weathering. The cross-laminated IPL samples had large internal cracks and delamination that occurred after the sample was exposed to weathering. Direct statements cannot be made on the relationship between the microweathered and macroweathered specimens, since all of the macroweathered specimens were parallel-laminated. However, the IPL cross-laminated microweathered samples did result in a greater amount of delamination and internal cracking. It could be that when cross-laminating a sample, the thick IPH stabilizes the differences in shrinkage and swelling of the longitudinal and radial cell structure.

The micro-XCT results gave 3D adhesive penetration measurements that can be related back to the mechanical test performance of each specimen replication. The IPH samples had a lower EP measurement and COV than the IPL samples. The WP measurement and corresponding COV was similar for the IPH and IPL samples. There was variation here due to EW and LW differences between specimens, as well as

anatomical features like rays and resin canals. The EE-IPL samples had more crushing at the bondline, which could be due to the IPL penetrating and softening the EW cell wall before pressing. More sample replications are needed to test this hypothesis. The IPL specimens did not have a significant difference in weathering during the macro lap-shear tests, indicating a better response to weathering than the IPH samples, which did have significant differences after weathering exposure.

The IMDI micro-XCT samples did not provide sufficient contrast during scanning. This was likely caused by an error during adhesive formation that resulted in a lower concentration of iodine in the formulated IMDI than desired. EDS and XFM information confirmed the presence of iodine in areas of the samples containing adhesive. XFM revealed significantly lower concentration of iodine in the IMDI than the IPH adhesive. Confirmation that the adhesives were covalently bonded with iodine was done with gel permeation and ion chromatography analyses by a previous experiment. In addition to low concentration of iodine, a high beam energy may have overwhelmed the scan and reduced the image contrast.

The nano-XCT results are the first of this kind reported in the literature. Lessons were learned during scanning while at the APS on beamline 32 ID. The small sample size permitted only 1-2 Douglas-fir cells within the FOV (50 μm^3), which made the stability difficult to control during XCT scanning. Movements of a fraction of a micron were detectable and resulted in unclear tomograms. To get quality penetration results from the nano-XCT data, clear phases of wood cell and adhesive must be identified. Three of the thirty datasets obtained were able to be used for an adhesive penetration analysis, and unfortunately only included the IPL. The three successful datasets did provide good

information to detect adhesive penetration at a resolution of 60 nm^3/voxel. The box scan analysis of the reconstructed images showed adhesive penetration based on a gradient of grayscale values from an adhesive-filled lumen to an adjacent cell wall. A gradient of adhesive concentration was detectable in the cell wall up to a depth of approximately 500 nm. If nano-XCT data was available for multiple adhesive formulations, a statistical comparison could give information on the difference in adhesive penetration. Two of the nano-XCT samples were successfully identified within the micro-XCT dataset. This was only accomplished with detailed note taking during the sectioning procedure.

While there were not any quality nano-XCT datasets for the IPH and IMDI samples, XFM data was collected on these samples that showed signs of penetration into the cell substance. Calibration of the XFM data provided quantitative information on the concentration of iodine per pixel. However, the XFM data was lower spatial resolution than the nano-XCT data, so comparisons between the IPL and IPH samples are difficult. It can be concluded that both IPL and IPH had some degree of adhesive penetration into the cell substance. It seems the IPL samples have a more gradual slope of grayscale values from the adhesive-filled lumen, into the cell wall, than the IPH, but no direct comparison can be made.

Conclusions about adhesive penetration into the cell wall, and the effects of weathering, are dependent on the type of bonded wood, as well as the specimen size. The macroweathered specimens were positively influenced by the lower MW portion of the IPL by a more even transfer of strain around the bondline. There was no significant difference found in the weathered vs. dry IPL samples, indicating that the adhesive performed similarly dry vs weathered. In the microweathered cross-laminated specimens,

it appeared that the bulk of the IPH provided more stabilization and less internal cracking. To see clear variations in the effect of molecular weight, penetration, and mechanical bond performance, a more extreme difference in molecular weights (> 10,000 g/mol) might show more definite differences. Overall, there was more effective adhesive penetration in the lower molecular weight adhesive and less shear strain calculated from the DIC macroweathered analysis. This indicated that adhesive penetration could have a positive influence on moisture durability, although the variability is too high to make a definite conclusion, and there were not enough replicates to compare the amount of adhesive penetration into the cell wall.

5.2 Limitations and Future Work Recommendations

This project had certain limitations that should be considered for future work around the topic of adhesive penetration and durability. XCT is an advanced method that can result in high quality images for the use of measuring adhesive penetration. Future work on this data may include Digital Volume Correlation (DVC) to model the shrinking and swelling of the bonded wood sample. XCT opens many opportunities for exploration but comes with certain limitations. Maximizing the number of useable datasets is critical in order to make conclusions, especially when collecting data from a facility such as Argonne National Laboratory, which has a competitive user program and therefore limited available scan time. Sample preparation and scanning is time intensive, therefore ensuring the sample and scanning parameters are sufficient is important. If the image quality is not pristine, the data is essentially useless for quantitative measurements. Future work on examining the effects of adhesive penetration into the cell substance should focus heavily on effective tagging of the adhesive to ensure sufficient x-ray

attenuation contrast between the two substances. For the nano-XCT scanning, a stabilization procedure should be experimented to eliminate poor image quality and scanning defects, and increase useable datasets for penetration comparisons.

Within the data, the x-ray attenuation within the adhesive decreased as it neared the cell wall. This was an unexpected phenomenon. The authors speculate that the adhesive polymerizes differently next to the cell wall substance than it does in the middle of the lumen, but are unsure whether it is attributed to the iodine tagging or the nature of the PF adhesive. This trend was seen throughout different methods including the nano-XCT, EDS, and XFM data, although not in all datasets. This would be an interesting aspect of the data to research in future projects.

Wood is a naturally variable material and therefore reducing variability to make fundamental conclusions can be difficult. This data had high variability, which cannot be ignored when analyzing the results. Elimination of possible sources of variation helps to improve the clarity of the conclusions. Optimum weathering cycles matched with sample type and size should be carefully considered when attempting to detect differences in the effects of weathering. Accelerated weathering regimes are balanced between conditions that are not extreme enough, to ones that are too harsh and will result in unusable specimens.

In addition, DIC has inherent limitations and assumptions that can add to the variability. The DIC technique assumes that the measurements on the surface of the sample are consistent throughout the width of the sample. This may or may not be the case but this uncertainty can add to the variation in the results. In this study, the shear strain from DIC is a measurement that is only between the notched area whereas the load

is being measured over the whole sample. When comparing these to produce a shear stress vs. shear stain curve, the assumption is that the load is not altered by sample and/or test setup features outside of the DIC AOI. This is also uncertain. Further, when using DIC to analyze a bonded wood sample, the thick PF bondline can be too dark and not converge. The system measures displacement by the convergence of the speckle pattern. Without adequate convergence of an area that does not have the contrast needed, the algorithm cannot calculate the shear strain.

BIBLIOGRAPHY

Alldritt, K. (2013). *Designing a strand orientation pattern for improved shear properties of oriented strand board* (Thesis). Oregon State University, Corvallis, OR.

Ammann, S., Schlegel, S., Beyer, M., Aehlig, K., Lehmann, M., Jung, H., & Niemz, P. (2016). Quality assessment of glued ash wood for construction engineering. *European Journal of Wood and Wood Products*, *74*(1), 67–74.

APA PS 1-09. (2010). *Voluntary Product Standard: PS 1-09 Structural Plywood*. 20-49

ASTM D2559. (2012). *ASTM D2559-12ae1 Standard Specification for Adhesives for Bonded Structural Wood Products for Use Under Exterior Exposure Conditions*. West Conshohocken, PA: ASTM International.

ASTM D5266. (2013). *ASTM D5266 Standard Practice for Estimating the Percentage of Wood Failure in Adhesive Bonded Joints*. West Conshohocken, PA: ASTM International.

Bastani, A., Adamopoulos, S., Koddenberg, T., & Militz, H. (2016). Study of adhesive bondlines in modified wood with fluorescence microscopy and x-ray micro-computed tomography. *International Journal of Adhesion & Adhesives*, *68*, 351–358.

Bin, B., Rukai, Z., Songtao, W., Wenjing, Y., Gelb, J., Gu, A., Xiangxiang, Z., & Ling, S. (2013). Multi-scale method of nano(micro)-CT study on microscopic pore structure of tight sandstone of Yanchang Formation, Ordos Basin. *Petroleum Exploration and Development*, *40*(3), 354–358.

BS EN 321. (2002). *BE EN 321:2002. Wood-based panels. Determination of moisture resistance under cyclic test conditions.* (p. 12). British Standards Institute.

Derome, D., Griffa, M., Koebel, M., & Carmeliet, J. (2011). Hysteretic swelling of wood at cellular scale probed by phase-contrast X-ray tomography. *Journal of Structural Biology*, *173*, 180–190.

Dowd, B. A., Campbell, G. H., Marr, R. B., Nagarkar, V. V., Tipnis, S. V., Axe, L., & Siddons, D. P. (1999). Developments in synchrotron x-ray computed microtomography at the National Synchrotron Light Source, 224–236.

Evans, P. D., Morrison, O., Senden, T. J., Vollmer, S., Roberts, R. J., Limaye, A., Arns, C. H., Averdunk, H., Lowe, A., & Knackstedt, M. A. (2010). Visualization and numerical analysis of adhesive distribution in particleboard using X-ray micro-computed tomography. *International Journal of Adhesion & Adhesives*, *30*, 754–762.

Frazier, C. (2002). The interphase in bio-based composites: what is it, what should it be? (pp. 206–212). Presented at the 6th Pacific Rim Bio-Based Composites Symposium, Portland, Oregon.

Frazier, C., & Ni, J. (1998). On the occurrence of network interpenetration in the wood-isocyanate adhesive interphase. *International Journal of Adhesion & Adhesives*, *18*, 81–87.

Frihart, C. (2005). Adhesive bonding and performance testing of bonded wood products. *Journal of ASTM International*, *2*(7), 1–12.

Frihart, C. (2006). *Characterization of the cellulosic cell wall*. Ames, Iowa, USA: Blackwell Publishing Professional.

Frihart, C. (2009). Adhesive groups and how they relate to the durability of bonded wood. *Journal of Adhesion Science and Technology*, *23*, 601–617.

Frihart, C. R., & Hunt, C. G. (2010). *Wood Handbook*. Forest Products Laboratory, Madison, WI: General Technical Report FPL-GTR-190.

Gindl, W. (2001). SEM and UV-microscopic investigation of glue lines in Parallam PSL. *Holzforschung*, *59*, 211–214.

Gindl, W., Dessipri, E., & Wimmer, R. (2002). Using UV-microscopy to study diffusion of melamine-urea-formaldehyde resin in cell walls of spruce wood. *Holzforschung*, *56*, 103–107.

Gindl, W., & Gupta, H. S. (2002). Cell-wall hardness and young's modulus of melamine-modified spruce wood by nano-indentation. *Composites Part A: Applied Science and Manufacturing*, *33*, 1141–1145.

Gindl, W., & Müller, U. (2006). Shear strain distribution in PRF and PUR bonded 3-ply wood sheets by means of electronic laser speckle interferometry. *Wood Science and Technology, 40*, 351–357.

Gindl, W., Schoberl, T., & Jeronimidis, G. (2004). The interphase in phenol-formaldehyde and polymeric methylene di-phenyl-di-isocyanate glue lines in wood. *International Journal of Adhesion & Adhesives*, *24*, 279–286.

Gürsoy, D., De Carlo, F., Xiao, X., & Jacobsen, C. (2014). TomoPy: a framework for the analysis of synchrotron tomographic data. *Journal of Synchrotron Radiation, 21*, 118–1193.

Haibel, A. (2008). *Advanced tomographic methods in materials research and engineering*. Oxford, New York: Oxford University Press.

Hass, P., Wittel, F. K., Mendoza, M., Herrmann, H. J., & Niemz, P. (2012). Adhesive penetration in beech wood: experiments. *Wood Science and Technology*, *46*, 243–256.

Hoheisel, M., Bernhardt, P., Lawaczeck, R., & Pietsch, H. (2006). Comparison of polychromatic and monochromatic x-rays for imaging. *Medical Imaging 2006: Physics of Medical Imaging*, *6142*(614209), 1605–7422.

Jakes, J., Hunt, C., Yelle, D., Lorenz, L., Hirth, K., Gleber, S.-C., Vogt, S., Grigsby, W., & Frihart, C. (2015). Synchrotron-based x-ray fluorescence microscopy in conjunction with nanoindentation to study molecular-scale interactions of phenol-formaldehyde in wood cell walls. *American Chemical Society Applied Materials and Interfaces*, *7*, 6584–6589.

Kamke, F., & Lee, J. N. (2007). Adhesive penetration into wood-a review. *Wood Science and Technology*, *39*(2), 205–220.

Kastner, J., Harrer, B., Requena, G., & Brunke, O. (2010). A comparative study of high resolution cone beam x-ray tomography and synchrotron tomography applied to Fe- and Al-alloys. *NDT&E International*, *43*, 599–605.

Khoury, B. M., Bigelow, E. M., Smith, L., Schlecht, S. H., Scheller, E. L., Andarawis-Puri, N., & Jepsen, K. J. (2015). The use of nano-computed tomography to enhance musculoskeletal research. *Connective Tissue Research*, *56*(2), 106–119.

Kojima, Y., Shimoda, T., & Suzuki, S. (2011). Evaluation of the weathering intensity of wood-based panels under outdoor exposure. *Journal of Wood Science*, *57*, 408–414.

Kretschmann, D. E. (2010). *Wood Handbook*. Forest Products Laboratory, Madison, WI: General Technical Report FPL-GTR-190.

Kumar, R., Hu, F., Hubbell, C. A., Ragauskas, A. J., & Wyman, C. E. (2013). Comparison of laboratory delignification methods, their selectivity, and impacts on physiochemical characteristics of cellulosic biomass. *Bioresource Technology*, *130*, 372–381.

Laborie, M.-P. (2002). *Investigation of the wood/phenol-formaldehyde adhesive interphase morphology* (Dissertation). Virginia Polytechnic Institute and State University, Blacksburg, VA.

Laleicke, P. F. (2015). *Non-destructive detection and monitoring of durability issues in wood panels under accelerated weathering* (Dissertation). Oregon State University, Corvallis, OR.

Li, W., Van den Bulcke, J., De Windt, I., Dhaene, J., & Van Acker, J. (2015). Moisture behavior and structural changes of plywood during outdoor exposure. *European Journal of Wood and Wood Products*.

Lu, W., Hu, Y., Yao, J., & Li, Y. (2013). Optimization and simulation research of tensile properties of wood lap joint. *Bioresource Technology*, *8*(1), 1409–1419.

Mannes, D., Marone, F., Lehmann, E., Stampanoni, M., & Niemz, P. (2010). Application areas of synchrotron radiation tomographic microscopy for wood research. *Wood Science and Technology*, *44*, 67–84.

Mayo, S. C., Chen, F., & Evans, R. (2010). Micron-scale 3D imaging of wood and plant microstructure using high-resolution x-ray phase-contrast microtomography. *Journal of Structural Biology*, *171*, 182–188.

Mendoza, M., Hass, P., Wittel, F. K., Niemz, P., & Herrmann, H. J. (2012). Adhesive penetration of hardwood: a generic penetration model. *Wood Science and Technology*, *46*, 529–549.

Metscher, B. D. (2013). Biological applications of X-ray microtomography: imaging microanatomy, molecular expression and organismal diversity. *Microscopy and Analysis*, *27*(2), 13–16.

Mirzaei, B. (2016). *Durability assessment of wood composites using fracture mechanics* (Dissertation). Oregon State University, Corvallis, OR.

Modzel, G., Kamke, F. A., & De Carlo, F. (2011). Comparative analysis of a wood: adhesive bondline. *Wood Science and Technology*, *45*, 147–158.

Müller, U., Sretenovic, A., Vincenti, A., & Gindl, W. (2005). Direct measurement of strain distribution along a wood bond line. Part 1: Shear strain concentration in a lap joint specimen by means of electronic speckle pattern interferometry. *Holzforschung*, *59*, 300–306.

Myridis, N. E. (2008). *Advanced tomographic methods in materials research and engineering*. (J. Banhart, Ed.) (4th ed., Vol. 51). Oxford University Press.

Paris, J. (2014, February 21). *Wood-adhesive bondline analyses with micro x-ray computed tomography* (Dissertation). Oregon State University, Corvallis, OR.

Paris, J., & Kamke, F. (2015). Quantitative wood-adhesive penetration with x-ray computed tomography. *International Journal of Adhesion & Adhesives*, *61*, 71–80.

Paris, J., Kamke, F., Mbachu, R., & Kraushaar Gibson, S. (2014). Phenol formaldehyde adhesives formulated for advanced x-ray imaging in wood-composite bondlines. *Journal of Material Science*, *49*, 580–591.

Patera, A., Derome, D., Griffa, M., & Carmeliet, J. (2013). Hysteresis in swelling and in sorption of wood tissue. *Journal of Structural Biology*, *182*, 226–234.

River, B. H., Vick, C. B., & Gillespie, R. H. (1991). *Wood as an adherend* (Vol. 7). New York: Marcel Dekker.

RStudio, T. (2015). RStudio: Integrated Development for R (Version R 3.2.3). Boston, MA: RStudio, Inc.

Saunders, C., & De Andrade, V. (2015, December 2). TXM at 32-ID home. *Confluence*. Page. Retrieved from https://confluence.aps.anl.gov/display/TXM/TXM+at+32-ID+Home

Schindelin, J., Arganda-Carreras, I., Frise, E., Kaynig, V., Longair, M., Pietzsch, T., Preibisch, S., Rueden, C., Saalfeld, S., Schmid, B., Tinevez, J.-Y., White, D. J., Hartenstein, V., Eliceiri, K., Tomancak, P., & Cardona, A. (2012). Fiji: an open-source platform for biological-image analysis. *Nature Methods*, *9*(7), 676–682. http://doi.org/10.1038/nmeth.2019

Schneider, P., Stauber, M., Voide, R., Stampanoni, M., Donahue, L. R., & Müller, R. (2007). Ultrastructural properties in cortical bone vary greatly in two inbred strains of mice as assessed by synchrotron light based micro- and nano-CT. *Journal of Bone and Mineral Research*, *22*(10), 1557–1569.

Schwarzkopf, M. (2014, August 27). *Characterization of load transfer in wood-based composites* (Dissertation). Oregon State University, Corvallis, OR.

Schwarzkopf, M., Muszynski, L., & Nairn, J. (2013). Stereomicroscopic optical method for the assessment of load transfer across the adhesive bond interphase (pp. 100–109). Presented at the International Conference on Wood Adhesives, Toronto, Ontario.

Serrano, E., & Enquist, B. (2005). Contact-free measurement and non-linear finite element analyses of strain distribution along wood adhesive bonds. *Holzforschung*, *59*, 641–646.

Shearing, P. R., Bradley, R. S., Gelb, J., Lee, S. N., Atkinson, A., Withers, P. J., & Brandon, N. P. (2011). Using synchrotron x-ray nano-CT to characterize SOFC electrode microstructures in three-dimensions at operating temperature. *Electrochemical and Solid-State Letters*, *14*(10), B117–B120.

Sonnenschein, M. F., Wendt, B. L., & Sonnenschein, G. F. (2005). Interfacial factors affecting polymeric diphenylmethane diisocyanate/wood bond strength. *Journal of Applied Polymer Science*, *98*, 449–455.

Standfest, G., Kranzer, S., Petutschnigg, A., & Dunky, M. (2010). Determination of the microstructure of an adhesive-bonded medium density fiberboard (MDF) using 3-D sub-micrometer computer tomography. *Journal of Adhesion Science and Technology*, *24*, 1501–1514.

Stephens, S., & Kutscha, N. (1987). Effect of resin molecular weight on bonding flakeboard. *Wood and Fiber Science*, *19*(4), 353–363.

Steppe, K., Cnudde, V., Girard, C., Lemeur, R., Cnudde, J.-P., & Jacobs, P. (2004). Use of x-ray computed microtomography for non-invasive determination of wood anatomical characteristics. *Journal of Structural Biology*, *148*, 11–21.

Stöckel, F., Konnerth, J., Moser, J., Kantner, W., & Gindl-Altmutter, W. (2012). Micromechanical properties of the interphase in pMDI and UF bond lines. *Wood Science and Technology*, *46*, 611–620.

Subramanian, V., Luo, H., Wang, F., Cooper, W., Lu, H., & Komanduri, R. (2011). *Mechanisms of granular materials: experimentation and simulations for determining the compressive and shear behaviors of sand at granular and meso scales*.

Sutton, M. A., Orteu, J.-J., & Schreier, H. W. (2009). *Image correlation for shape, motion and deformation measurements: basic concepts, theory and applications*. New York, NY, USA: Springer.

Svensson, S., Turk, G., & Hozjan, T. (2011). Predicting moisture state of timber members in a continuously varying climate. *Engineering Structures*, *33*, 3064–3070.

Trtik, P., Dual, J., Keunecke, D., Mannes, D., Niemz, P., Stähli, P., Kaestner, A., Groso, A., & Stampanoni, M. (2007). 3D imaging of microstructure of spruce wood. *Journal of Structural Biology*, *159*, 46–55.

Vick, C. B., Richter, K., River, B. H., & Fried, A. R. (1995). Hydroxymehtylated resorcinol coupling agent for enhanced durability of bisphenol-a epoxy bonds to sitka spruce. *Wood and Fiber Science*, *27*(1), 2–12.

Wang, S. (2015). TXM MKI Kickoff Meeting. *Confluence*. presentation. Retrieved from https://confluence.aps.anl.gov/display/TXM/TXM+at+32-ID+Home

Way, D. (2015). *Proof of concept for a three-dimensional molded core wood-strand sandwich panel* (Thesis). Oregon State University, Corvallis, OR.

Wildenschild, D., Hopmans, J. W., Vaz, C. M. P., Rivers, M. L., Rikard, D., & Christensen, B. S. . (2002). Using x-ray computed tomography in hydrology: systems, resolutions, and limitations. *Journal of Hydrology*, *267*, 285–297.

Xu, P., Donaldson, L. A., Gergely, Z. R., & Staehelin, L. A. (2007). Dual-axis electron tomography: a new approach for investigating the spatial organization of wood cellulose microfibrils. *Wood Science and Technology*, *41*, 101–116.

Zauner, M. (2015). *Damage Evolution in wood and layered wood composites monitored in situ by acoustic emission, digital image correlation and synchrotron based tomographic microscopy*. ETH Zurich.

Zauner, M., Keunecke, D., Mokso, R., Stampanoni, M., & Niemz, P. (2012). Synchrotron-based tomographic microscopy (SbTM) of wood: development of a testing device and observation of plastic deformation of uniaxially compressed Norway spruce samples. *Holzforschung*, *66*(8), 973–979.

Zink, A. G., Davidson, R. W., & Hanna, R. B. (1995). Strain measurement in wood using a digital image correlation technique. *Wood and Fiber Science*, *27*(4), 346–359.

APPENDICES

Appendix A. Additional Micro-X-ray Computed Tomography Segmentation

Figure 88 - Figure 95 show the additional micro-XCT segmentation graphics from Section 4.2.2. The graphics are shown in the same order as listed in Table 36 and were used in the EP and WP calculations.

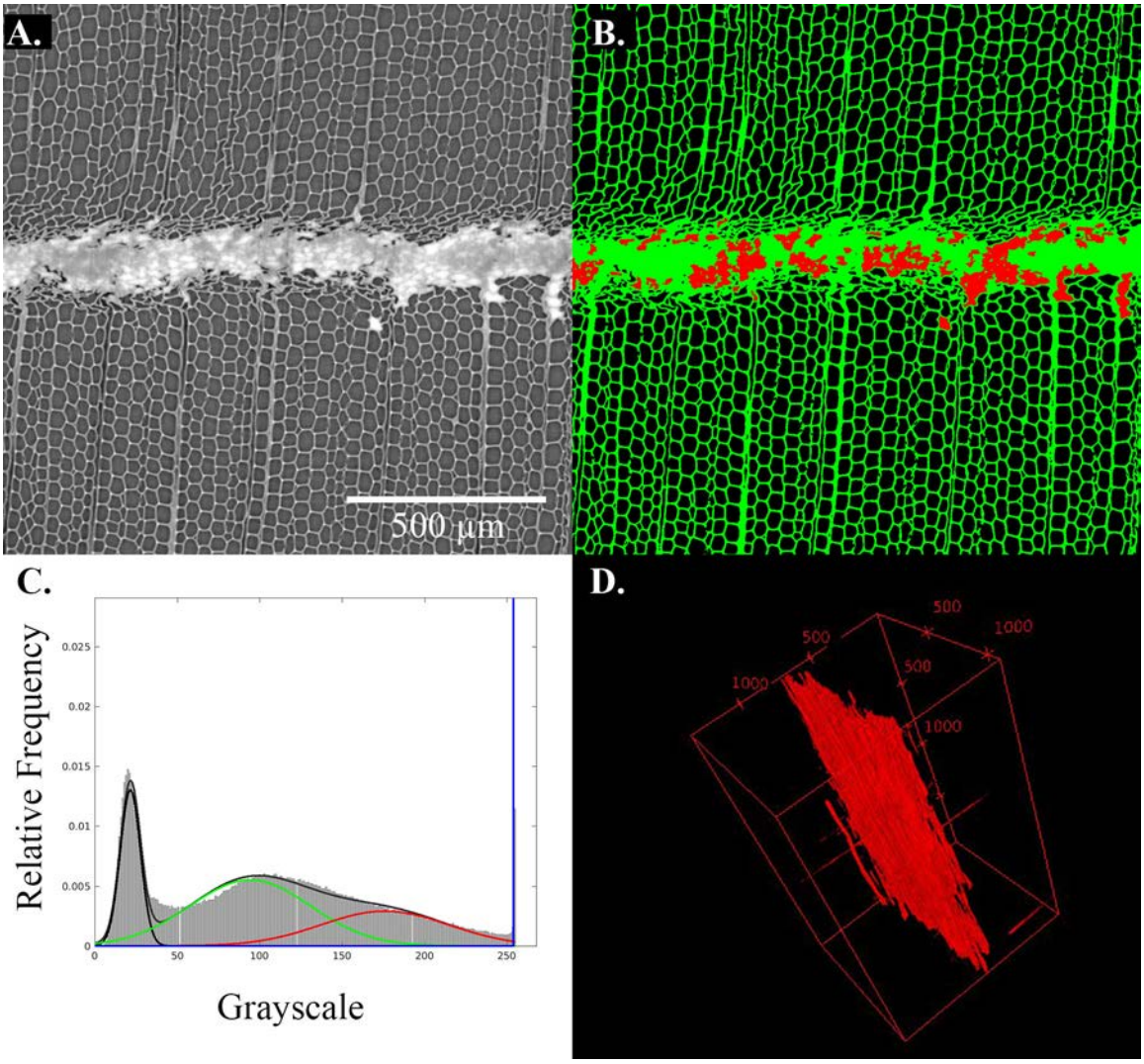

Figure 88. Micro-XCT segmentation of EE-IPH-2; A.) original micro-XCT slice; B.) micro-XCT slice after color mapping; C.) distribution of grayscale values (8-bit); black peak is void space, green peak is wood substance, red peak is adhesive penetration into cell substance, blue peak is pure adhesive; D.) combined pure adhesive and penetration phases in 3D with the full dataset outlined by the red box.

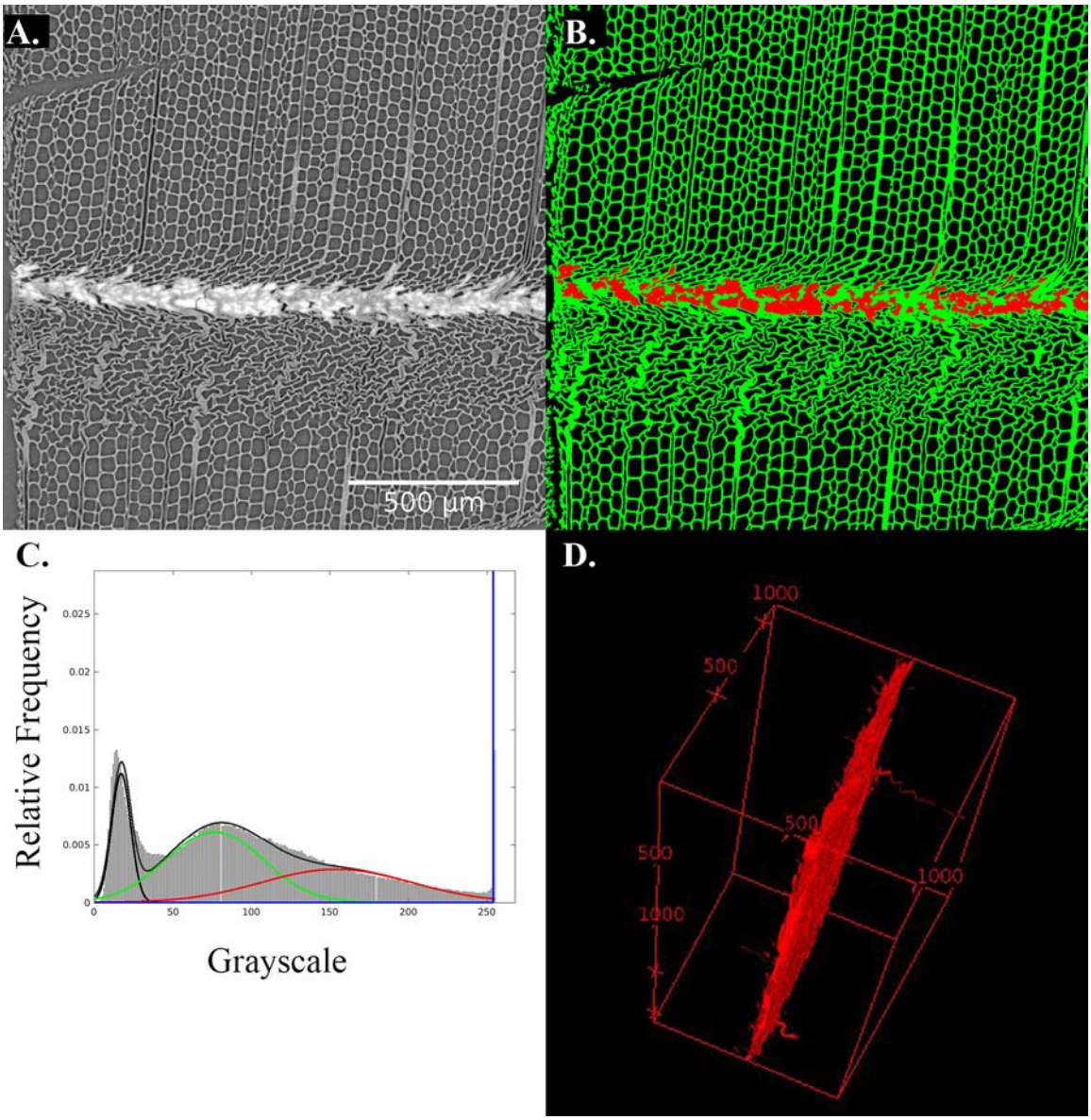

Figure 89. Micro-XCT segmentation of EE-IPH-3; A.) original micro-XCT slice; B.) micro-XCT slice after color mapping; C.) distribution of grayscale values (8-bit); black peak is void space, green peak is wood substance, red peak is adhesive penetration into cell substance, blue peak is pure adhesive; D.) combined pure adhesive and penetration phases in 3D with the full dataset outlined by the red box.

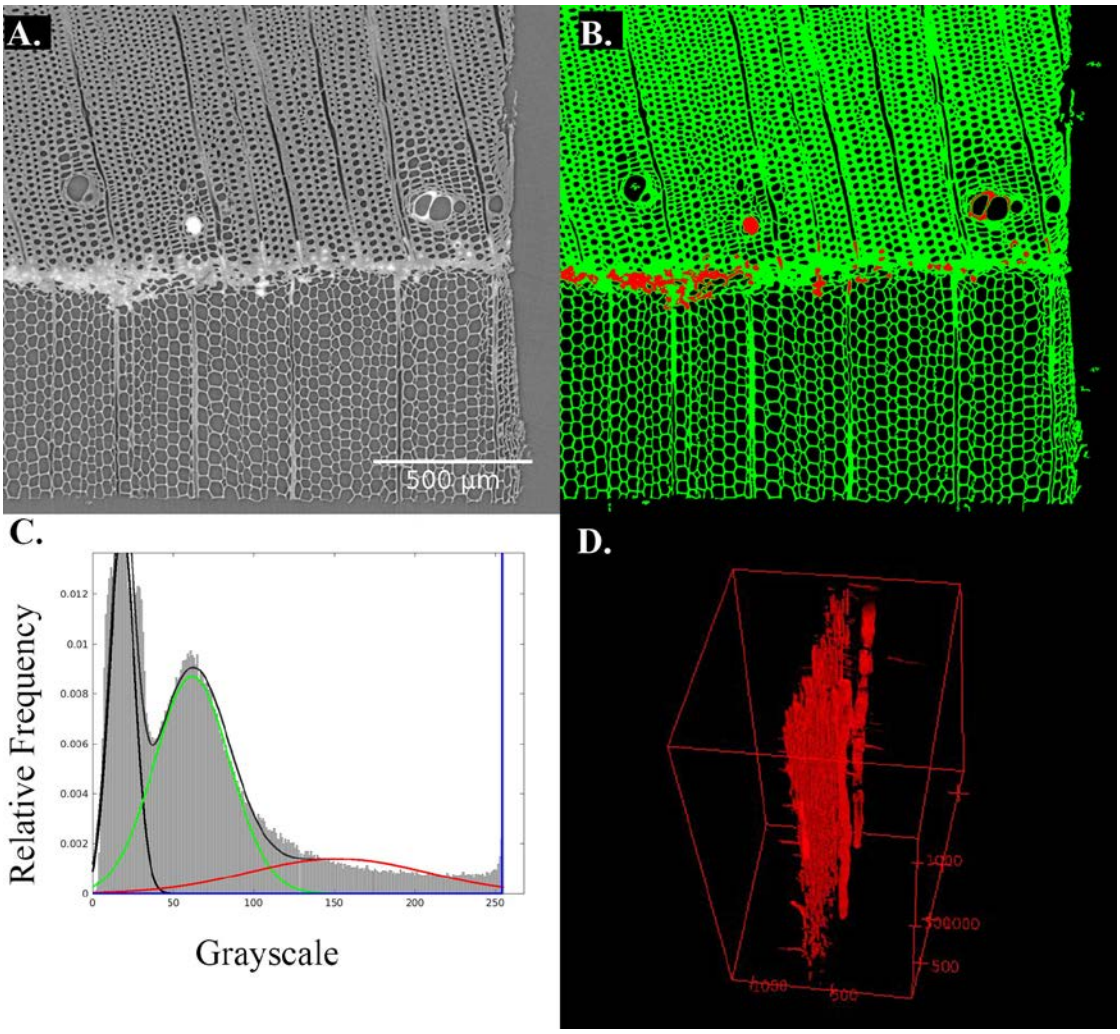

Figure 90. Micro-XCT segmentation of EL-IPH-4; A.) original micro-XCT slice; B.) micro-XCT slice after color mapping; C.) distribution of grayscale values (8-bit); black peak is void space, green peak is wood substance, red peak is adhesive penetration into cell substance, blue peak is pure adhesive; D.) combined pure adhesive and penetration phases in 3D with the full dataset outlined by the red box.

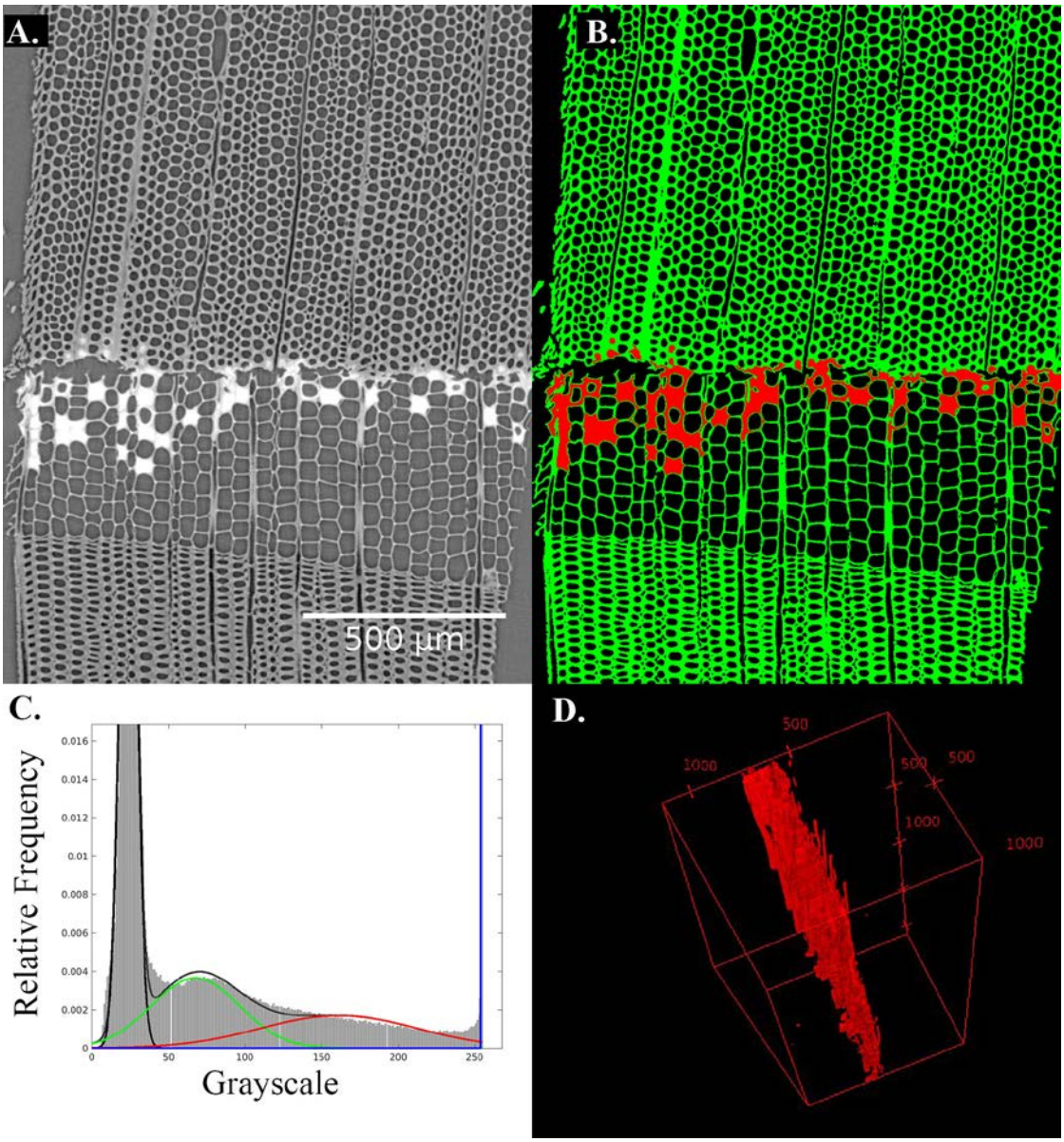

Figure 91. Micro-XCT segmentation of EL-IPH-6; A.) original micro-XCT slice; B.) micro-XCT slice after color mapping; C.) distribution of grayscale values (8-bit); black peak is void space, green peak is wood substance, red peak is adhesive penetration into cell substance, blue peak is pure adhesive; D.) combined pure adhesive and penetration phases in 3D with the full dataset outlined by the red box.

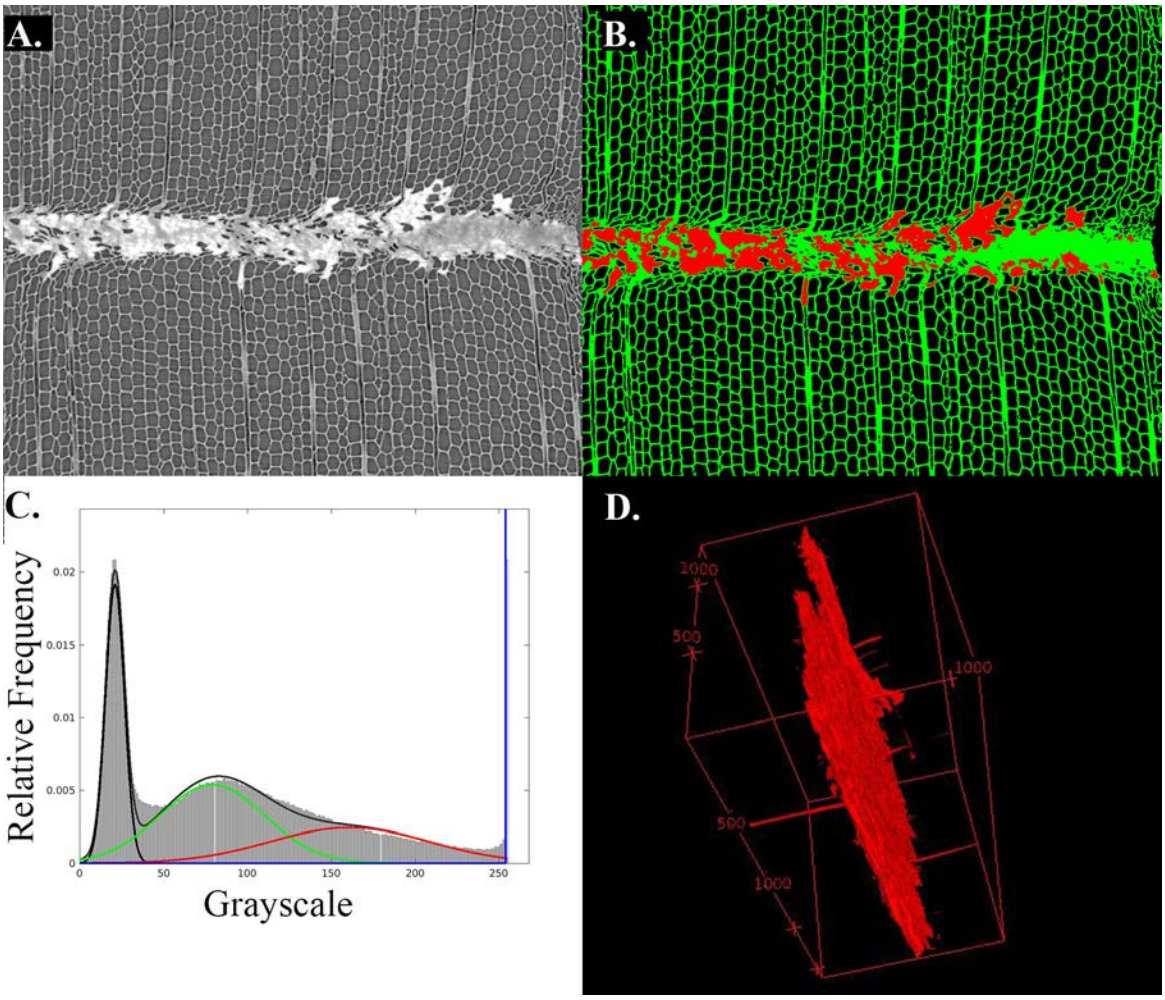

Figure 92. Micro-XCT segmentation of EE-IPL-1; A.) original micro-XCT slice; B.) micro-XCT slice after color mapping; C.) distribution of grayscale values (8-bit); black peak is void space, green peak is wood substance, red peak is adhesive penetration into cell substance, blue peak is pure adhesive; D.) combined pure adhesive and penetration phases in 3D with the full dataset outlined by the red box.

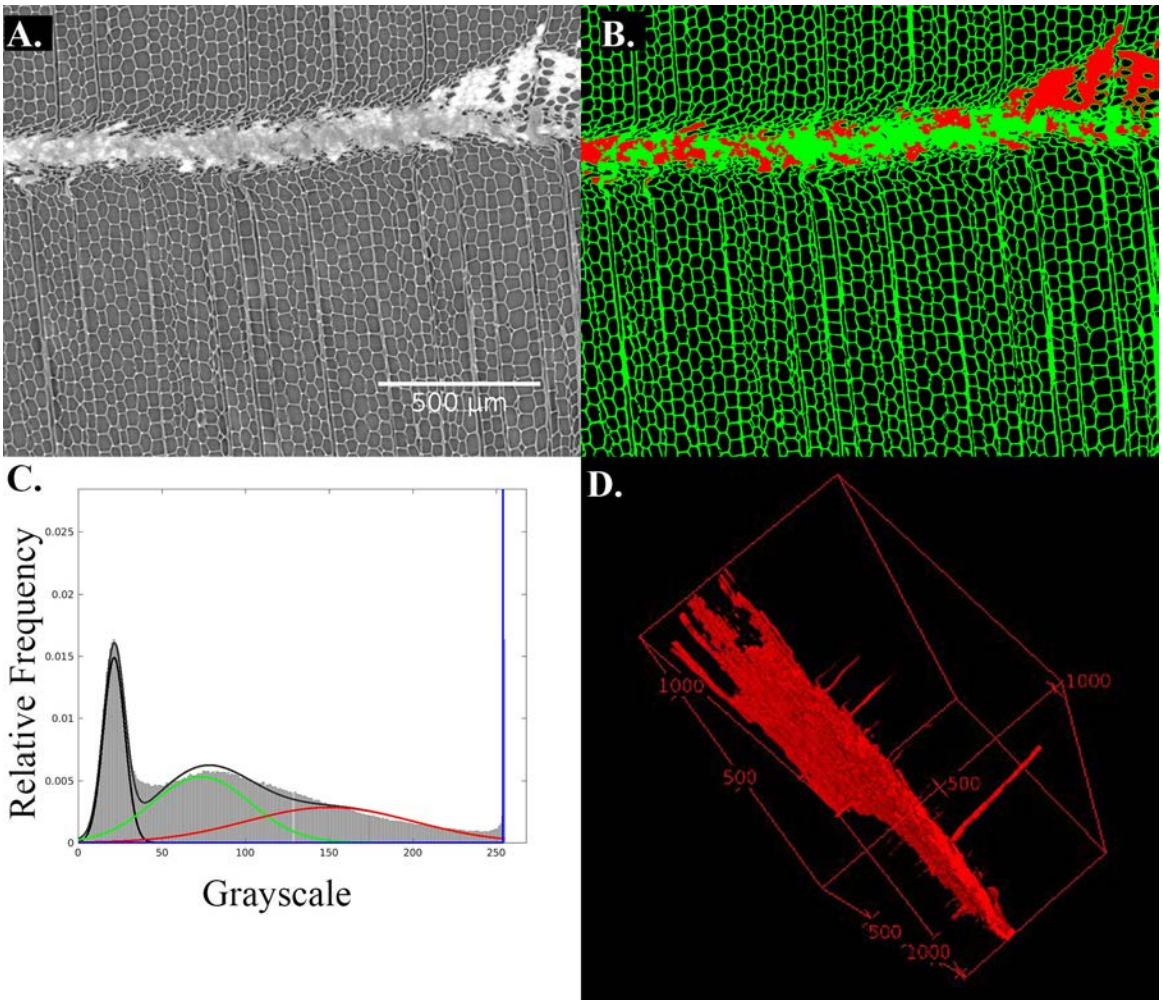

Figure 93. Micro-XCT segmentation of EE-IPL-3; A.) original micro-XCT slice; B.) micro-XCT slice after color mapping; C.) distribution of grayscale values (8-bit); black peak is void space, green peak is wood substance, red peak is adhesive penetration into cell substance, blue peak is pure adhesive; D.) combined pure adhesive and penetration phases in 3D with the full dataset outlined by the red box.

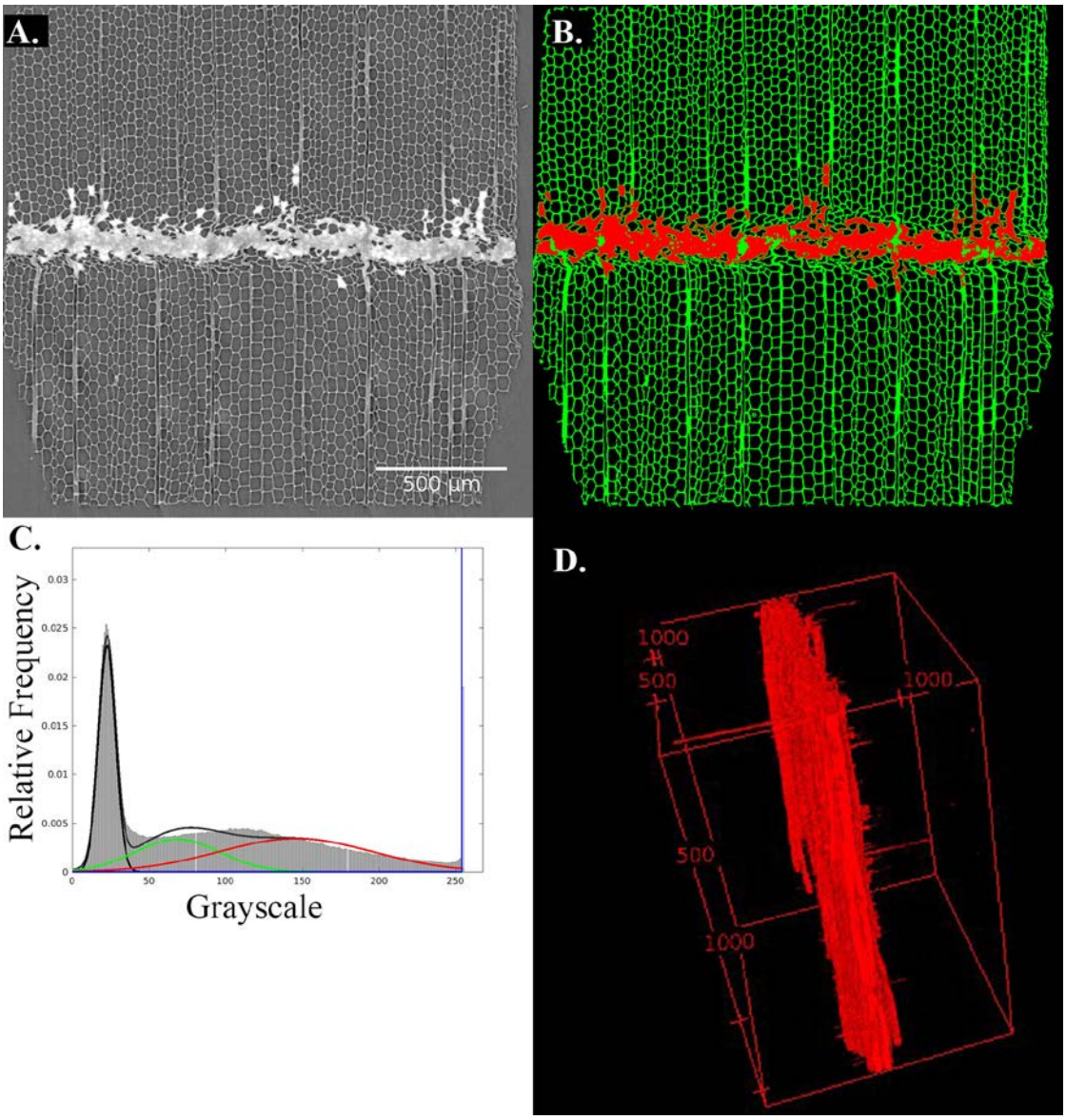

Figure 94. Micro-XCT segmentation of EE-IPL-4; A.) original micro-XCT slice; B.) micro-XCT slice after color mapping; C.) distribution of grayscale values (8-bit); black peak is void space, green peak is wood substance, red peak is adhesive penetration into cell substance, blue peak is pure adhesive; D.) combined pure adhesive and penetration phases in 3D with the full dataset outlined by the red box.

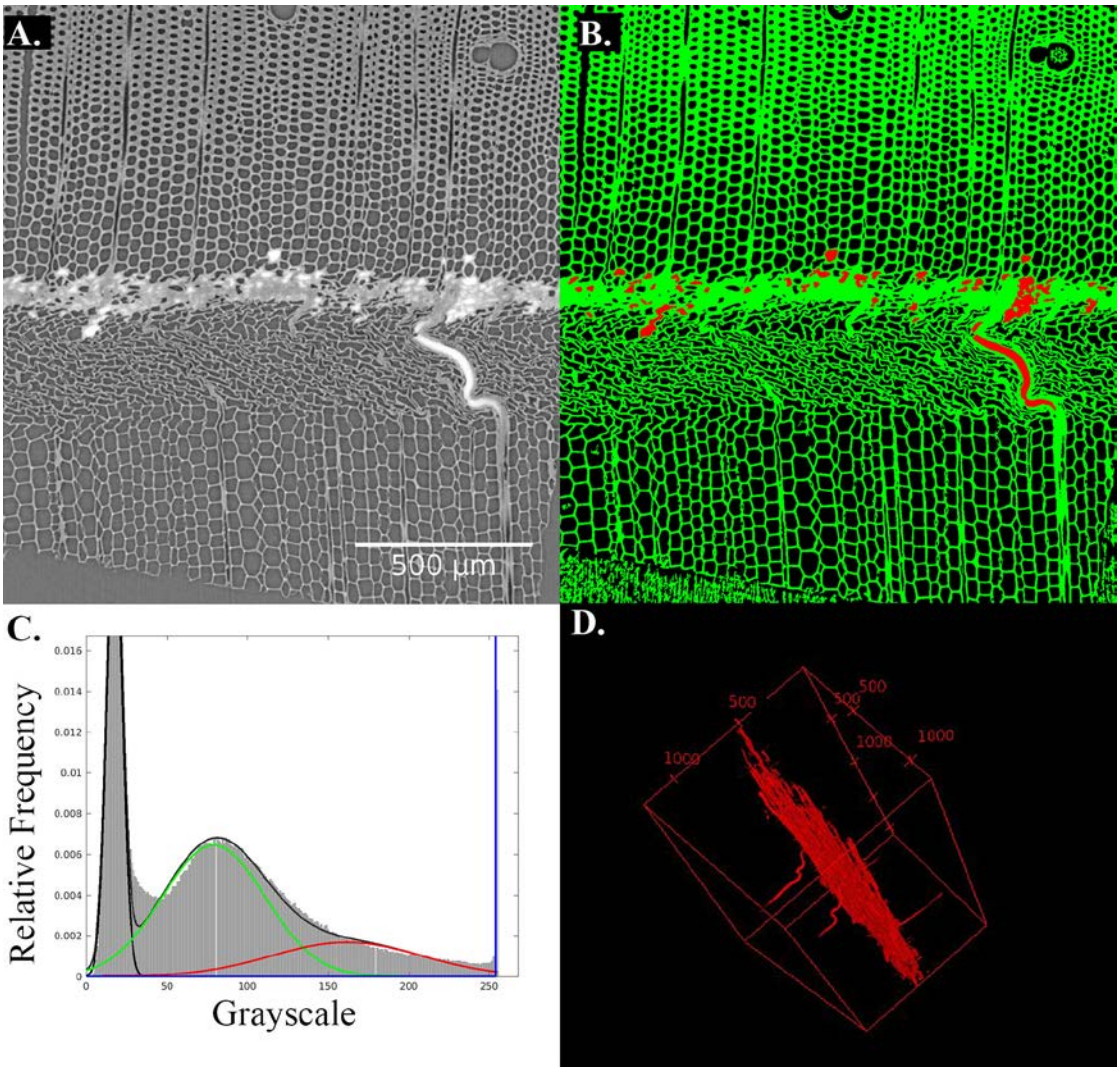

Figure 95. Micro-XCT segmentation of EL-IPL-1; A.) original micro-XCT slice; B.) micro-XCT slice after color mapping; C.) distribution of grayscale values (8-bit); black peak is void space, green peak is wood substance, red peak is adhesive penetration into cell substance, blue peak is pure adhesive; D.) combined pure adhesive and penetration phases in 3D with the full dataset outlined by the red box.

Appendix B. Additional X-ray Fluorescence Microscopy Results

Figure 96 - Figure 101 show additional XFM analyses of IPH and IMDI samples in the same manner as Section 4.4.2.

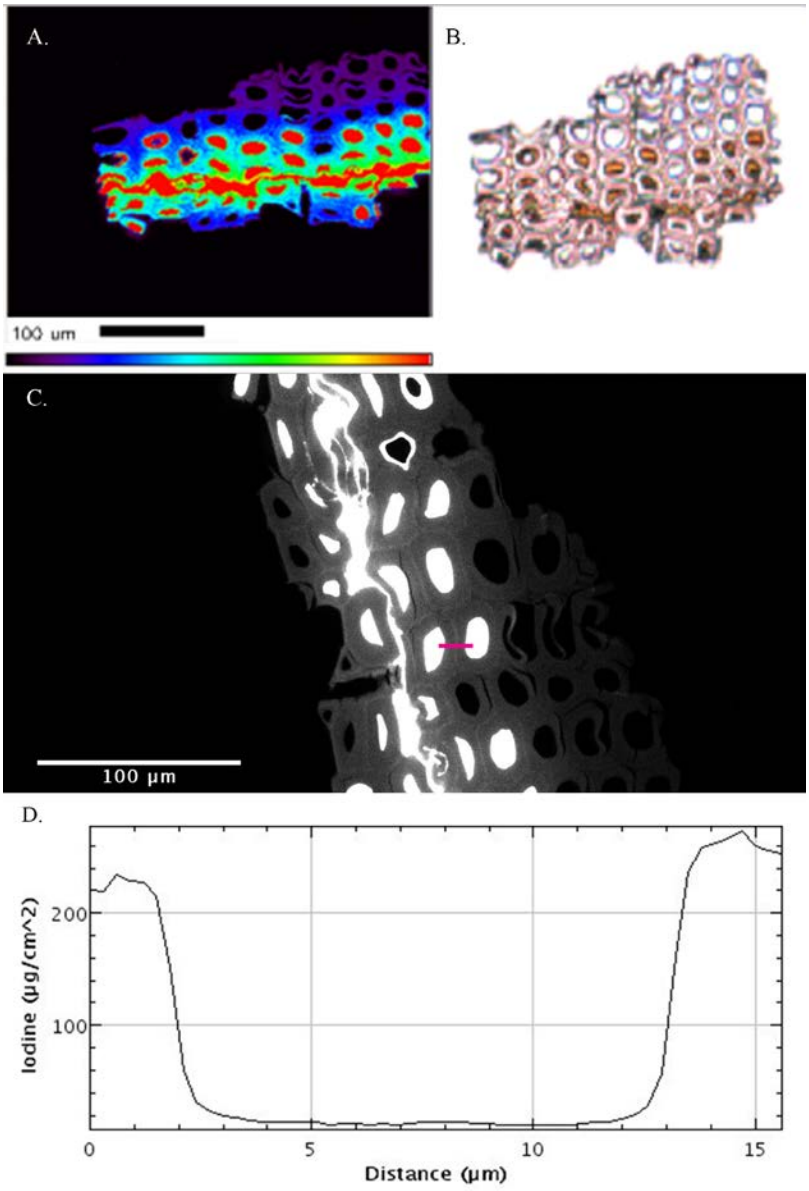

Figure 96. XFM of IPH (A.) Color mapped section of iodine; (B.) Original 2 µm thick slice with bondline located near the bottom of the slice; (C.) grayscale slice after rotating CW 78^{o} relative to image A; pink line indicates line scan; (D.) distribution of iodine across line.

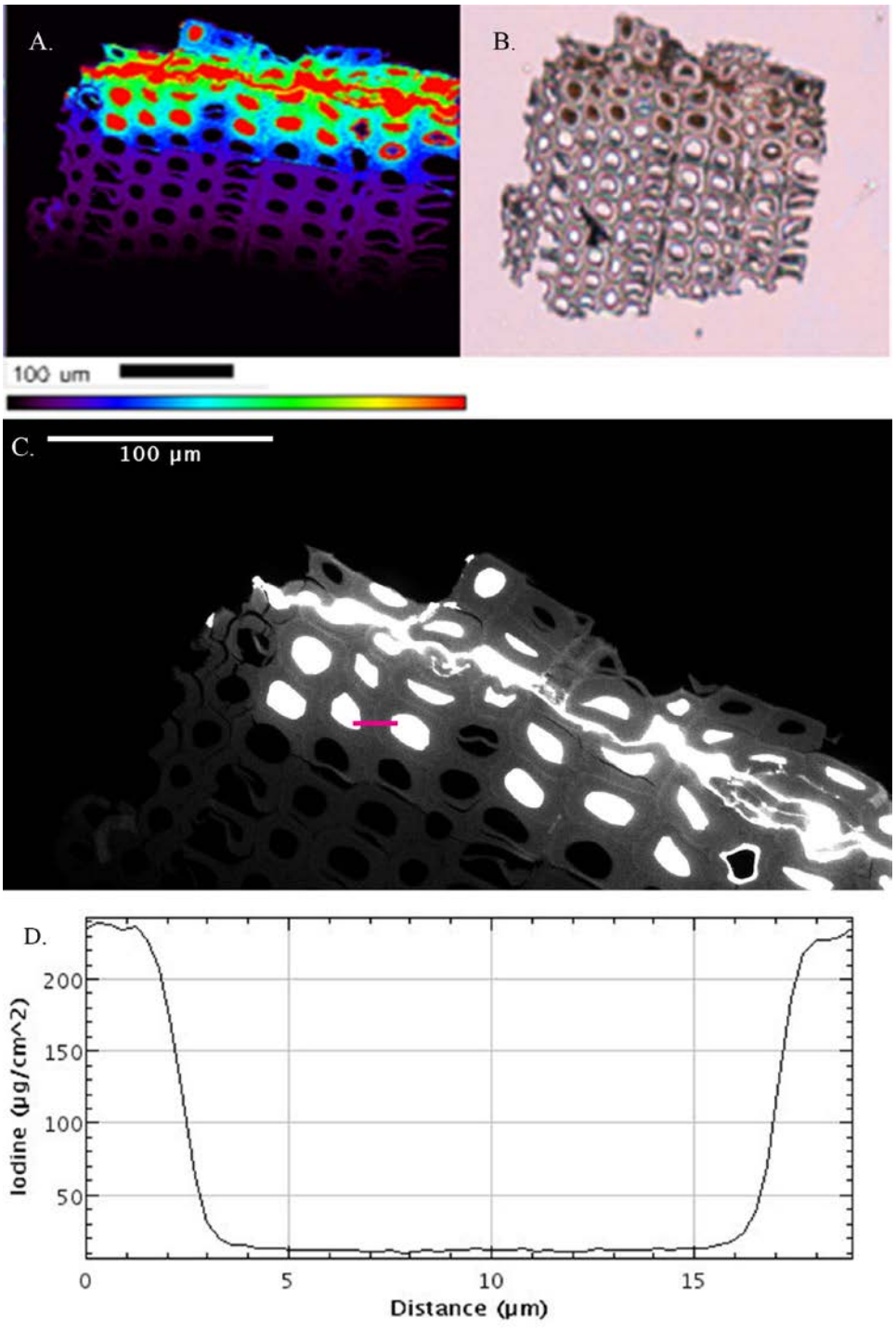

Figure 97. XFM of IPH (A.) Color mapped section of iodine; (B.) Original 2 µm thick slice with bondline located near the bottom of the slice; (C.) grayscale slice after rotating CW 18^{o} relative to image A; pink line indicates line scan; (D.) distribution of iodine across line.

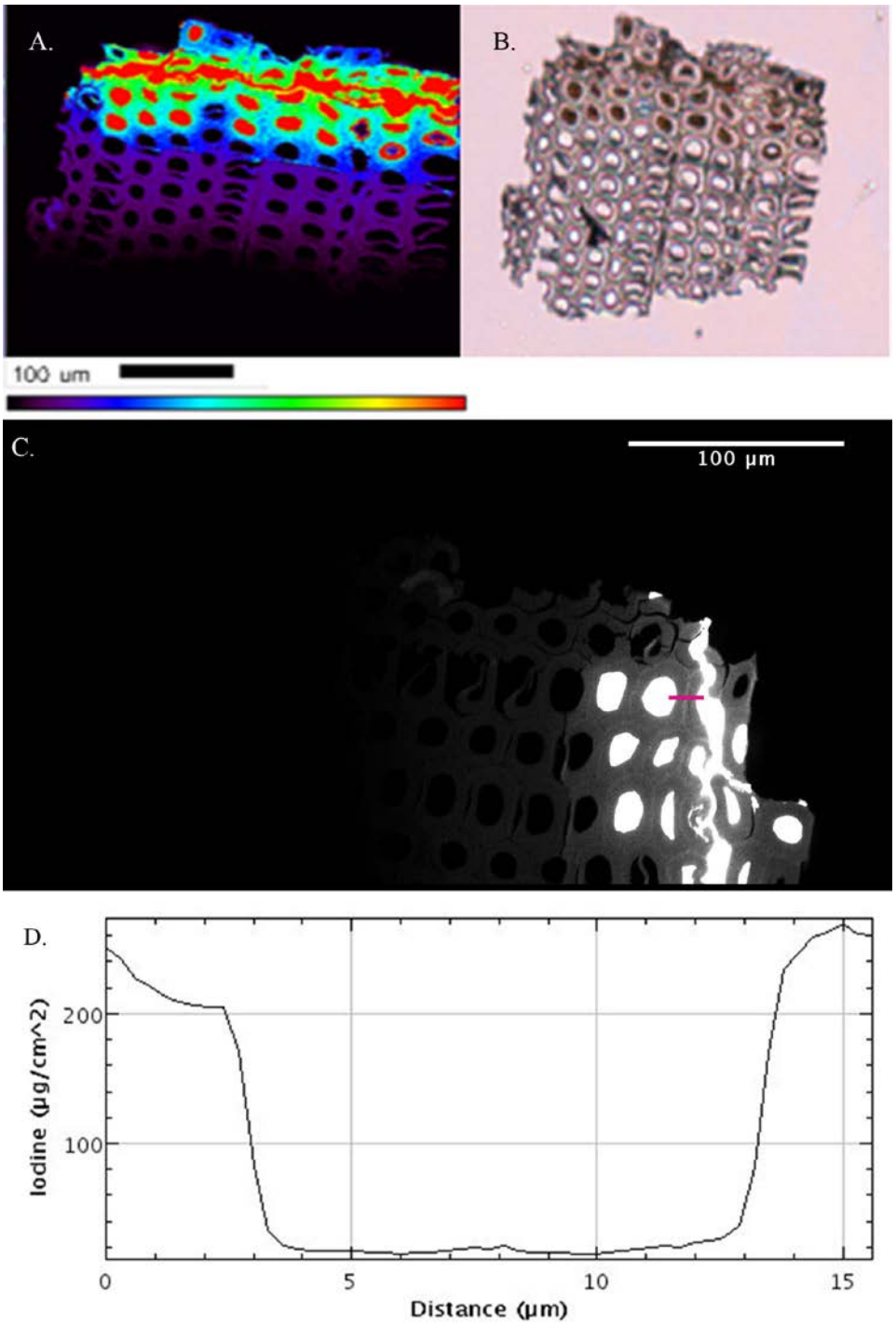

Figure 98. XFM of IPH (A.) Color mapped section of iodine; (B.) Original 2 µm thick slice with bondline located near the bottom of the slice; (C.) grayscale slice after rotating CW 86^{o} relative to image A; pink line indicates line scan; (D.) distribution of iodine across line.

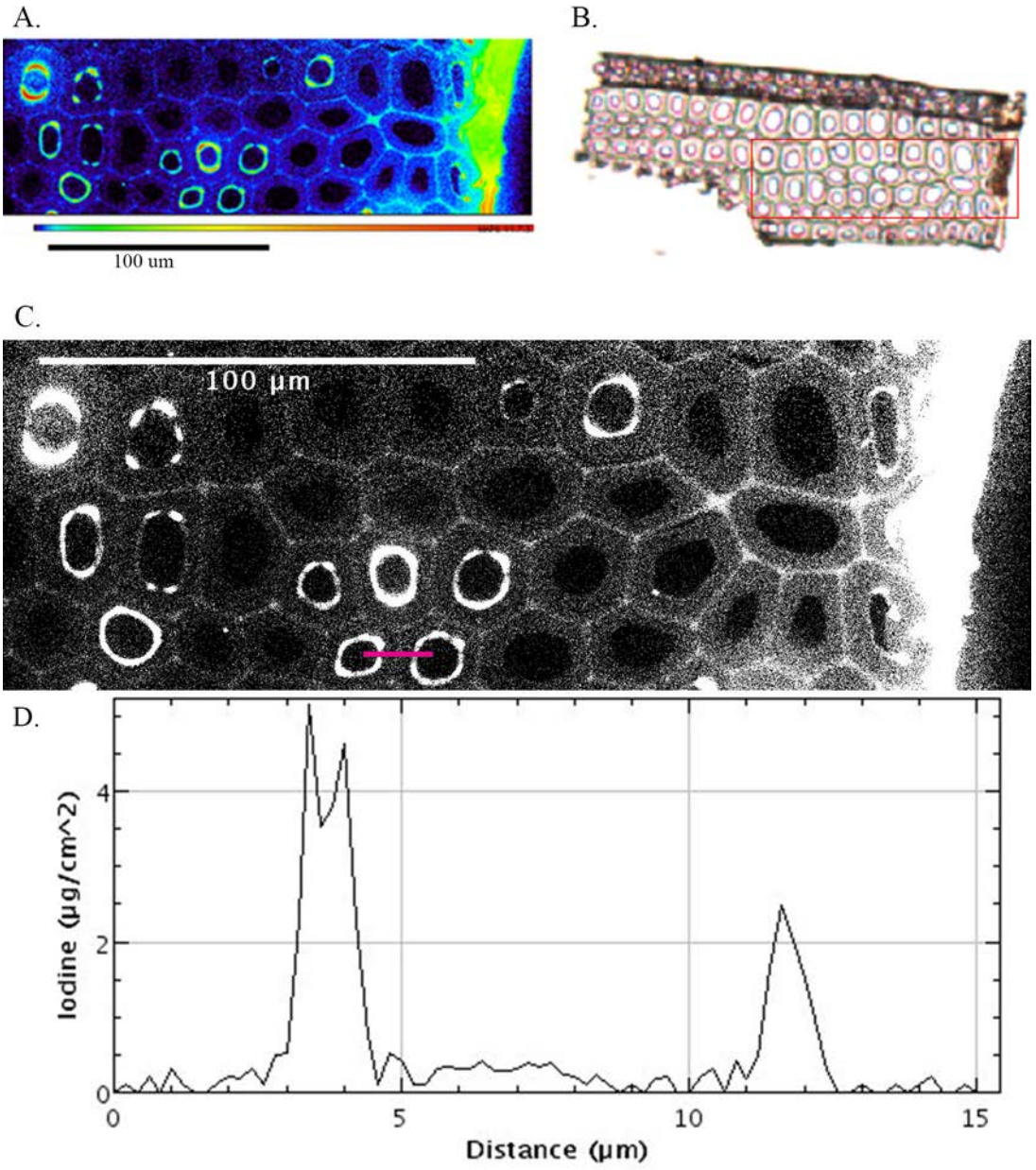

Figure 99. XFM of IMDI (A.) Color mapped section of iodine; (B.) Original 2 µm thick slice with bondline located near the bottom of the slice; (C.) grayscale slice; pink line indicates line scan; (D.) distribution of iodine across line.

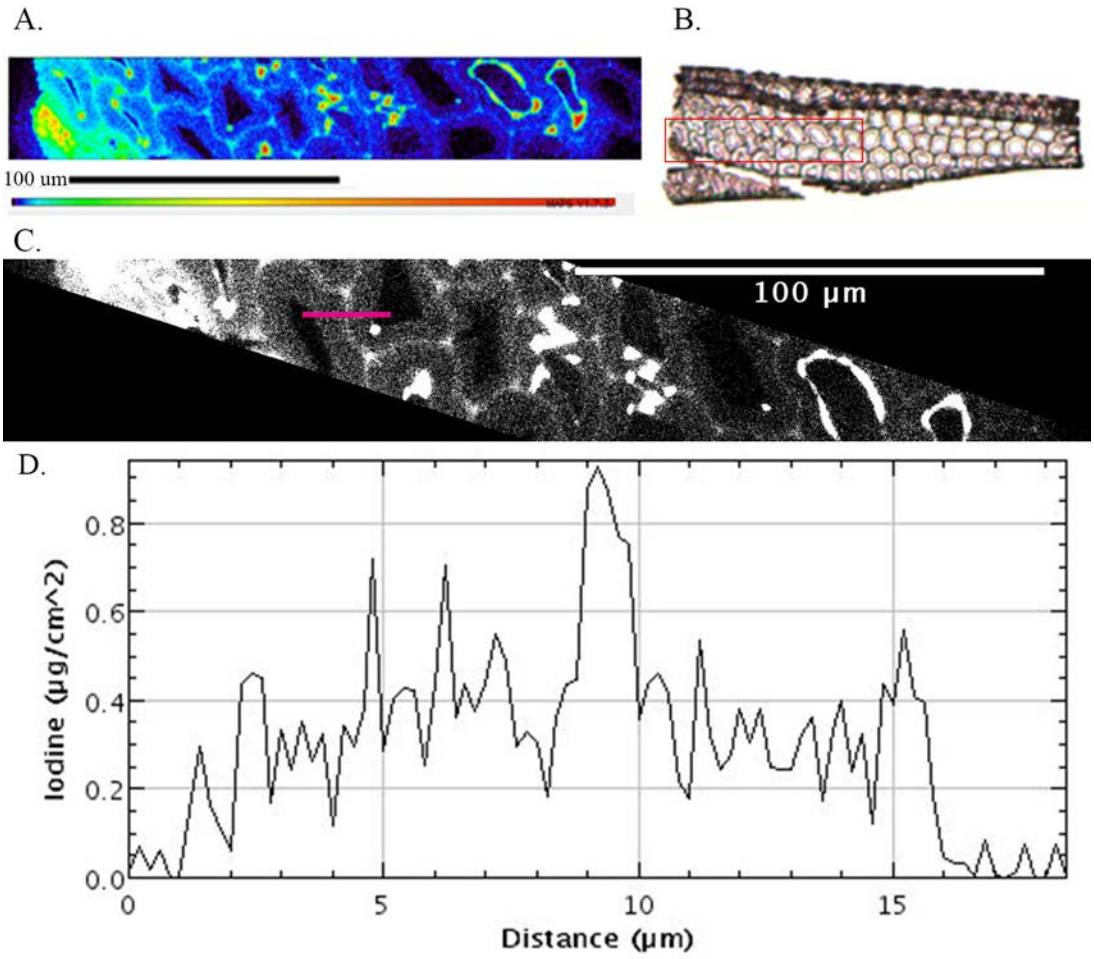

Figure 100. XFM of IMDI (A.) Color mapped section of iodine; (B.) Original 2 µm thick slice with bondline located near the bottom of the slice; (C.) grayscale slice after rotating CW 18^{o} relative to image A; pink line indicates line scan; (D.) distribution of iodine across line.

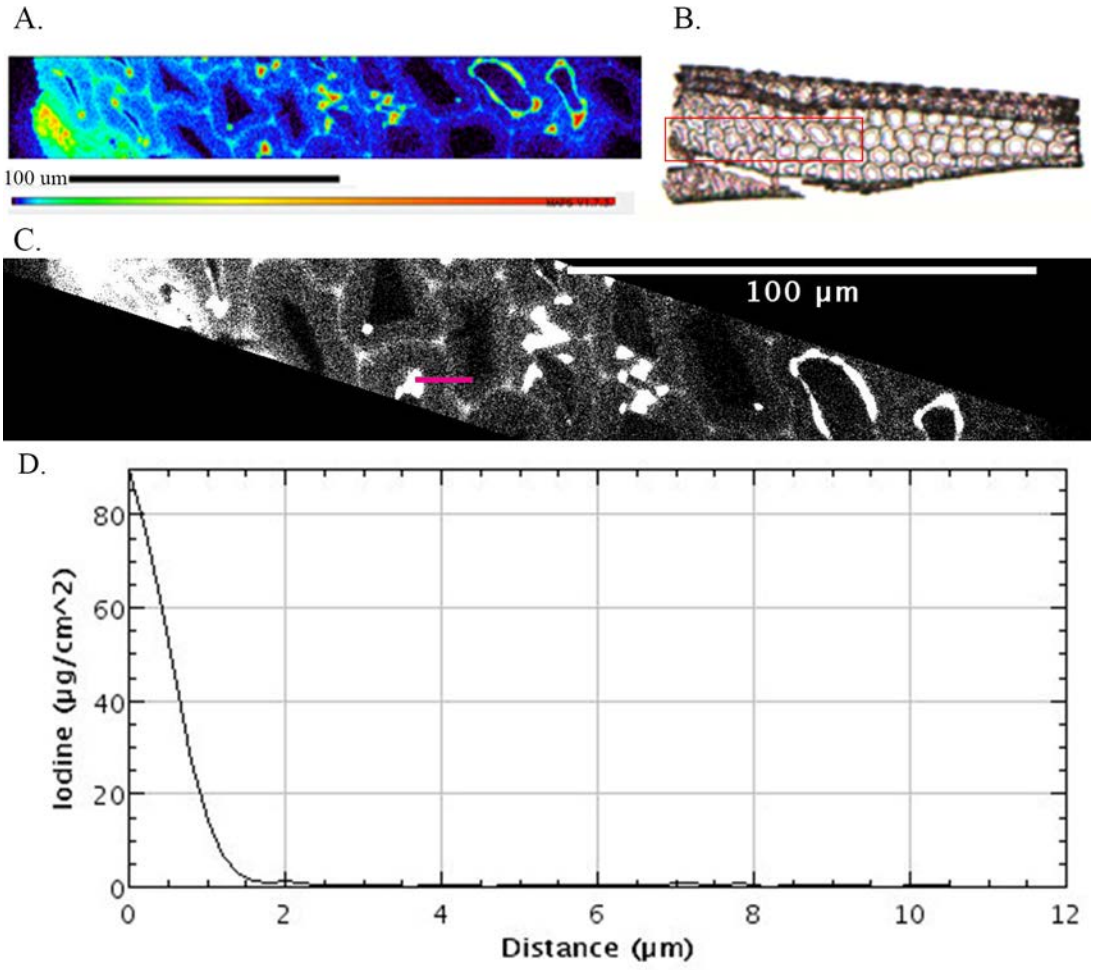

Figure 101. XFM of IMDI (A.) Color mapped section of iodine; (B.) Original 2 µm thick slice with bondline located near the bottom of the slice; (C.) grayscale slice after rotating CW 18^{o} relative to image A; pink line indicates line scan; (D.) distribution of iodine across line scan.

Appendix C. Scripts

The script used for the micro-XCT segmentation procedure was run in Matlab, and developed by Daniel Ching, graduate student at Oregon State University. It is available online at: https://github.com/carterbox/wpart/releases/tag/v2.2.0. Chad Hammerquist, graduate student at Oregon State University, developed the script used to import and convert the shear strain DIC data into absolute values and average the shear strain measurements for each image taken. This script was run in RStudio. Warren Sept, a high school intern who worked for Lech Muszyński, developed the macro used for the wood-adhesive failure thresholding, which was run in ImageJ.